DISSERTATION

submitted to the

Combined Faculty of Mathematics, Engineering and Natural Sciences

of Heidelberg University, Germany

for the degree of

Doctor of Natural Sciences

Put forward by

MOLLY ROSE ANN WELLS

born in Taunton, England

Oral examination: July 17th, 2025

THE ROLE OF FILAMENTARY FLOWS IN HIGH MASS STAR FORMATION

MOLLY ROSE ANN WELLS

REFEREES:

PROF. DR. HENRIK BEUTHER

PROF. DR. LAURA KREIDBERG

ABSTRACT

Accretion flows onto dense structures in star-forming regions plays a crucial role in the formation and growth of stars. These flows, which occur on multiple spatial scales – from large-scale filaments down to small cores – are responsible for channelling material onto protostellar objects. Understanding the properties of these flows is vital for developing a comprehensive picture of star formation, yet the detailed mechanisms governing their dynamics remain unclear. In this thesis, I investigate the properties of accretion flows in high-mass star-forming clusters, with a focus on understanding the interplay between gas dynamics, environmental conditions, and the evolutionary stage of the systems. Using interferometric data from the ALMA evolutionary study of high mass protocluster formation in the Galaxy, single dish data from the IRAM 30m observatory and synthetic observations from magnetohydrodynamic (MHD) simulations, I explore how material is transported along filamentary structures and accumulated onto dense cores. The results reveal that accretion flow rates are closely tied to the mass of the cores, following a $M^{2/3}$ relationship that supports the tidal-lobe accretion model. I find that flow rates have an increasing trend with respect to their evolutionary stages, suggesting a connection between accretion dynamics and the age of the star-forming system. Additionally, feedback from newly-formed stars is shown to significantly affect the flow structure. In feedback-dominated regions, feeder filaments sustain material flows onto the central clump, emphasising the importance of environmental conditions in shaping the accretion process. Through a multi-scale analysis of accretion flows, I find that the flow rates decrease slightly as we move from large to small spatial scales. This thesis contributes to our understanding of the complex dynamics driving star formation. By integrating observational data with theoretical models, it bridges the gap between the large-scale collapse of molecular clouds and the detailed accretion mechanisms moving material onto forming protostars, offering new insights into how this material is accumulated in star-forming regions.

ZUSAMMENFASSUNG

Akkretionsflüsse auf dichte Wolkenkerne in Sternentstehungsgebieten spielen eine entscheidende Rolle bei der Entstehung und Entwicklung von Sternen. Diese Flüsse, die auf verschiedenen räumlichen Skalen auftreten - von großflächigen Filamenten bis hin zu kleinen Kernen - sind für die Kanalisierung von Material auf protostellare Objekte verantwortlich. Die Eigenschaften dieser Flüsse zu verstehen ist für die Ausarbeitung eines umfassenden Bildes der Sternentstehung von entscheidender Bedeutung, jedoch sind die detaillierten Mechanismen, die diese Dynamiken steuern, nach wie vor unklar. In dieser Dissertation untersuche ich die Eigenschaften von Akkretionsflüssen in massereichen Sternentstehungshaufen mit Schwerpunkt auf dem Zusammenspiel zwischen Gasdynamik, Umgebungsbedingungen und den Entwicklungsstadien der Systeme. Anhand interferometrischer Daten der ALMA Evolutionssstudie über Enstehung sehr massiver protocluster in der Galaxie, Daten des IRAM 30m Teleskops und synthetischer Beobachtungen aus magnetohydrodynamischen (MHD) Simulationen untersuche ich, wie Material entlang filamentärer Strukturen transportiert und in dichten Kernen angesammelt wird. Die Ergebnisse zeigen, dass die Akkretionsflussraten eng mit der Masse der Kerne verbunden sind und einem $M^{2/3}$ Gesetz folgen, welches das Modell der *tidal-lobe* Akkretion unterstützt. Die Flussraten in ihren Entwicklungsstadien weisen einen zunehmenden Trend mit den Entwicklungsstadien auf, was auf einen Zusammenhang zwischen der Akkretionsdynamik und dem Alter der untersuchten Systeme hindeutet. Außerdem zeigt sich, dass Feedback von neu gebildeten Sternen die Strömungsstruktur erheblich beeinflusst. In Regionen, in denen Feedback dominiert, halten die einspeisenden Filamente die Materialflüsse auf den zentralen Klumpen aufrecht, was die Bedeutung der Umgebungsbedingungen für die Gestaltung der Akkretionsprozesse unterstreicht. Durch eine Multiskalenanalyse der Akkretionsflüsse stelle ich fest, dass die Strömungsraten leicht abnehmen, wenn wir uns von großen zu kleinen räumlichen Skalen bewegen. Diese Arbeit trägt zu unserem Verständnis der komplexen Dynamik bei, die der Sternentstehung zugrunde liegt. Durch die Kombination von Beobachtungsdaten mit theoretischen Modellen schließt sie die Lücke zwischen dem großräumigen Kollaps von Molekülwolken und den detaillierten Akkretionsmechanismen, die Material auf die sich bildenden Protosterne transportieren, und bietet neue Einblicke in die Art und Weise, wie dieses Material in Sternentstehungsgebieten akkumuliert wird.

Show 'em what you're made of ladies

Contents

1 INTRODUCTION 1

1.1 The interstellar medium 1
1.2 Star formation sequence 3
    1.2.1 Giant molecular clouds 3
    1.2.2 Clumps and clusters 4
    1.2.3 Filaments 5
    1.2.4 Evolutionary sequence 6
1.3 Observations 10
    1.3.1 Single-dish telescopes 10
    1.3.2 Interferometry 12
    1.3.3 Molecular line emission 14
1.4 Flow rate equation 15
1.5 Theoretical simulations 17
1.6 Scientific motivation 19

2 ALMAGAL: FLOWS ALONG FILAMENTARY STRUCTURES 21

2.1 Introduction 22
2.2 Sample selection 25
    2.2.1 ALMAGAL survey details 25
    2.2.2 Sample 26
    2.2.3 Evolutionary stage 27
    2.2.4 Core identification 28
    2.2.5 Analysis 29
2.3 Flow rates 30
    2.3.1 Quantifying flow rates 31
    2.3.2 Column density 32
    2.3.3 Temperature estimates 32
    2.3.4 Width 33
    2.3.5 Velocity difference 34
    2.3.6 Error analysis 34
2.4 Results 37

2.4.1 Statistical testing 38
2.4.2 Evolutionary stage 38
2.4.3 Offset from the core 39
2.4.4 Core mass 41
2.5 Discussion 42
2.5.1 Comparison between low- and high-mass regions 42
2.5.2 Comparison to simulations 43
2.6 Conclusions 44

3 COMPARING THEORY AND OBSERVATION 45
3.1 Introduction 46
3.2 Simulation data 48
3.3 Filament identification 50
3.4 Methods 51
3.4.1 Velocity difference 52
3.4.2 Error analysis 53
3.5 Results 53
3.5.1 Along 55
3.5.2 Polar 56
3.5.3 Galactic inclination 57
3.6 Discussion 59
3.6.1 Comparison with 3D simulation values 60
3.6.2 Filament inclination 63
3.6.3 Comparison with observations 65
3.7 Conclusions 66

4 HIERARCHICAL FLOWS FROM CLOUDS TO CORES. 69
4.1 Introduction 70
4.2 Data 74
4.2.1 IRAM 30m 74
4.2.2 ALMAGAL 74
4.3 Methods 75
4.3.1 Structure identification 75
4.3.2 Column density 76
4.3.3 Width determination 77
4.3.4 Velocity difference 77
4.3.5 Sources of error 78
4.4 Results 79
4.4.1 Large scale 79
4.4.2 Small scales 82
4.4.3 Scale comparison 82
4.4.4 Evolutionary stage 84
4.5 Discussion 86

4.5.1 Different scales 86
4.5.2 Theoretical predictions 87
4.6 Conclusions 88

5 ADVANCING OUR UNDERSTANDING OF HIGH-MASS STAR FORMATION 89
5.0.1 Summary of results 90
5.0.2 Thesis conclusions 91
5.1 Outlook: The importance of studying high-mass star formation . . . 93
5.1.1 Towards a unified picture of accretion across multiple scales . 93
5.1.2 Time evolution of accretion flows 94
5.1.3 Environmental influences on accretion flows 94
5.1.4 The future of high-mass star formation research 95

Appendix A Additional material to Chapter 2 97
A.1 Sample parameter histograms 98
A.2 Core mass figures 98
A.3 Source and core parameters 99

Appendix B Additional material to Chapter 4 101
B.1 Scale figures 102
B.2 IRAM 30m 0th moment maps 105
B.3 IRAM 30m 1st moment maps 106

List of Figures 107

List of Tables 109

Publication list 111

Bibliography 113

Acknowledgments 119

1

INTRODUCTION

> "The universe is a pretty big place. It's bigger than anything anyone has ever dreamed of before. So if it's just us... seems like an awful waste of space."
> *Carl Sagan*

I've always loved this movie (and of course book), and this quote in particular – but I don't actually think it's a waste of space. The sheer vastness of the universe, full of wonders and unanswered questions, makes the idea that we're alone feel improbable. While this question drifts beyond the scope of this thesis, the immense expanse of stars, gas, and dust is at the heart of scientific exploration. Without it, the work presented here wouldn't exist. This thesis focuses on star formation in the Milky Way — a tiny piece of the universe, yet one that plays a crucial role in our understanding. The Milky Way is often used as a blueprint for studying galaxies beyond our own, helping us uncover the structure and evolution of the universe. In that sense, even this small corner of space connects to something much bigger, so maybe the singing dolls were wrong[1], maybe it's not such a small world after all.

1.1 The interstellar medium

The Interstellar Medium (ISM) is the matter that exists in the space between stars, consisting of gas in ionic, atomic, and molecular forms, as well as dust and cosmic rays. Figure 1.1 shows observations of the cold gas and dust in the southern hemisphere of the Galactic plane. The ISM plays a crucial role in the life cycle of galaxies, serving as the reservoir for star formation and acting as the medium through which stellar feedback and material are recycled. The components of the ISM are described below (information in this section is mostly taken from the reviews by Klessen & Glover (2016) and Ferrière (2001), with input from Caselli et al.

---

[1] From the 'its a small world' ride at Disney World in Florida, USA.

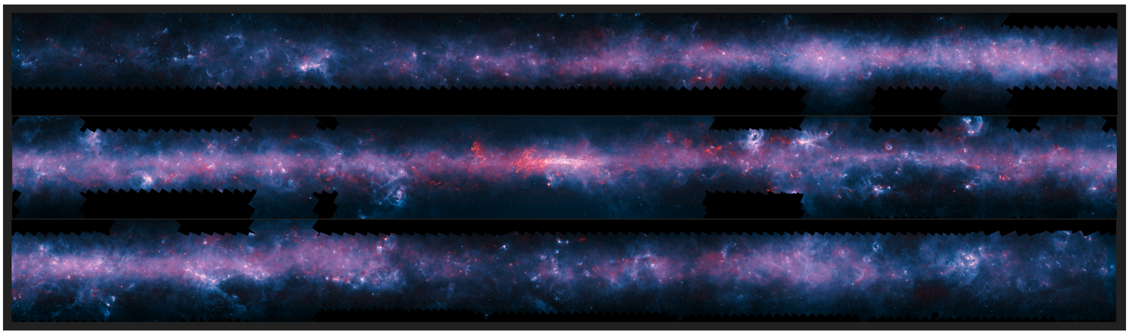

Figure 1.1: The full area of the Galactic plane visible from the southern hemisphere, mapped by the Atacama Pathfinder Experiment (APEX) single dish telescope in Chile as part of the APEX Telescope Large Area Survey of the Galaxy (ATLASGAL). The APEX data, shows up in red and the background blue image was imaged at shorter infrared wavelengths by the NASA Spitzer Space Telescope as part of the GLIMPSE survey. The fainter extended red structures come from complementary observations made by ESA's Planck satellite. Credit: ESO/APEX/ATLASGAL consortium/NASA/GLIMPSE consortium/ESA/Planck.

(1998), Wolfire et al. (2003) and Jenkins (2013)):

- Ionised gas: found around young, massive stars that emit ultraviolet, hydrogen-ionising radiation. These regions are typically at temperatures $> 10^5$ K with densities $< 1\,\mathrm{cm}^{-3}$ (e.g., Nava et al. 2019).
- Neutral atomic gas: composed mainly of neutral hydrogen atoms, these regions have densities on the order of $10\,\mathrm{cm}^{-3}$ and temperatures around 100 K. These are detectable via the 21 cm hydrogen line emission.
- Molecular gas: existing in the coldest and densest parts of the ISM, molecular gas is primarily hydrogen (H_2) and is the primary site for star formation. Giant Molecular Clouds (GMCs) are prominent examples of such regions, with average densities around 10^4 cm^{-3} and temperatures $\sim 20\,\mathrm{K}$ (e.g., Rathborne et al. 2006).
- Dust: consisting of tiny solid particles, dust grains absorb and scatter ultraviolet and visible light, re-emitting it in the infrared. Dust plays a vital role in cooling the ISM and facilitating the formation of molecular hydrogen.
- Cosmic rays: high-energy particles, predominantly protons, that permeate through the ISM and into molecular clouds, influencing its ionisation state and contributing to heating processes (e.g., Padovani et al. 2009).

The ISM is the birthplace of stars. Regions within molecular clouds can become gravitationally unstable, leading to the collapse of gas and dust to form new stars. The efficiency and rate of star formation are influenced by various factors, including the density, temperature, and turbulence within these clouds. Feedback mechanisms from newly formed stars, such as stellar winds, radiation pressure, and supernova explosions, can further impact the surrounding ISM by triggering or suppressing subsequent star formation (e.g., Mac Low & Klessen 2004). These factors also influence heating and cooling in the ISM. Heating mechanisms are stellar radiation, cosmic rays, collisions, and shocks while cooling occurs via atomic and molecular line emission (e.g., Draine 2011).

1.2 Star formation sequence

1.2.1 Giant molecular clouds

Giant molecular clouds are vast assemblies of molecular gas that serve as the primary birthplaces of stars within galaxies. Their masses range from 10^4 to 10^6 solar masses, and they span tens to hundreds of parsecs in size. The cold temperatures within GMCs, typically around 10 to 20 K, allow hydrogen to exist in its molecular form (H_2), facilitating the conditions necessary for star formation (e.g., Dobbs & Pringle 2013; García et al. 2014).

Observations indicate that GMCs exhibit a hierarchical structure, with dense clumps, clusters and filaments embedded within them. These substructures are the sites where star formation predominantly occurs. The collapse of GMCs and their substructures is a critical aspect of star formation (e.g., Froebrich & Rowles 2010). Two primary scenarios have been proposed to describe this process:

- Global Hierarchical Collapse (GHC): in this scenario, the entire GMC undergoes a hierarchical and chaotic collapse, where larger scales collapse first, leading to the formation of filaments and clumps, which subsequently fragment into cores that form stars. This model suggests that star formation occurs throughout the cloud and over extended periods, with feedback mechanisms from newly formed stars eventually dispersing the remaining gas, thereby regulating the star formation efficiency. This perspective is supported by observations of filamentary structures and accretion flows within GMCs (e.g., Vázquez-Semadeni et al. 2019).

- Localised collapse: alternatively, some studies propose that only specific regions within a GMC, typically the densest clumps, undergo collapse to form stars, while the rest of the cloud remains stable or is dispersed by feedback processes. This model emphasises the role of local conditions, such as density enhancements and turbulence dissipation, in triggering star formation. Observational evidence for this scenario includes the presence of star-forming cores within otherwise quiescent clouds (e.g., Vázquez-Semadeni et al. 2009; Pon et al. 2011).

The debate between these scenarios centres on the extent and scale at which gravitational collapse occurs within GMCs. Recent observations and simulations suggest that, in reality, both models are correct to some extent, with global collapse leading to the formation of filamentary networks, within which localised collapses give rise to individual stars or stellar clusters (e.g., Vázquez-Semadeni et al. 2009; Carroll-Nellenback et al. 2014). Understanding the relative contributions of these processes is crucial for developing a comprehensive theory of star formation.

By definition, high-mass stars have masses greater than eight solar masses ($8\,\mathrm{M}_\odot$). This is the lower mass limit that allows the star to explode as a supernova, leaving a remnant neutron star or stellar mass black hole. The formation of these high-mass stars has similarities and differences to the formation of their low-mass counterparts. Review publications (e.g., Beuther et al. 2025) provide a comparative analysis on this topic. A break down between low and high-mass parameters can be found in the following section (Sect. 1.2.2). While significant progress has been made in understanding these processes, ongoing research continues to refine our knowledge of the complex interplay between the various factors that govern the life cycle of GMCs and their role in shaping the stellar content of galaxies.

1.2.2 Clumps and clusters

As a GMC collapses, it fragments into smaller substructures known as clumps. These clumps are typically about 0.1-1 pc in size and serve as the precursors to star clusters, though not all clumps will necessarily form stars (e.g., Klessen et al. 1998). The density within these clumps is higher than the surrounding medium, making them susceptible to further gravitational collapse. The internal dynamics of clumps, influenced by turbulence and accretion processes, play a crucial role in their evolution and the subsequent formation of stars within them. Within these dense clumps, further fragmentation occurs, leading to the formation of cores that collapse to form individual stars or small stellar systems (e.g., Klessen et al. 2000; Heitsch et al. 2008).

In star-forming clumps, both high and low-mass stars often form concurrently. Despite differences in their final masses, they share notable similarities in initial conditions and early stages of star formation (all comparison information from Beuther et al. (2025)):

- Turbulent gas properties: both regimes exhibit turbulent motions within their natal clouds, influencing the fragmentation and collapse processes.
- Density structures: the hierarchical density structures observed in star-forming regions are common to both high and low-mass star formation, suggesting a shared underlying mechanism in the early stages.

While the foundational processes are alike, several quantitative differences distinguish high from low-mass star formation:

- Accretion rates: high-mass stars experience higher accretion rates compared to their low-mass counterparts, necessitating efficient mechanisms to transport angular momentum and sustain rapid mass accumulation.

- Outflow and infall rates: the rates of material outflow and infall are elevated in high-mass star-forming regions, reflecting the intense dynamics associated with massive star formation.

- Mean densities: high-mass star-forming regions typically exhibit higher mean column and volume densities, providing the necessary conditions to support the formation of massive stars.

- Multiplicity: there is a significant increase in stellar multiplicity from low to high-mass stars, with massive stars more likely to be found in multiple systems.

High-mass star formation also presents qualitative differences, primarily due to feedback effects:

- Radiative and ionising feedback: massive stars emit substantial ultraviolet radiation, leading to the ionisation of surrounding gas. This feedback can influence subsequent star formation by heating the local environment and dispersing molecular material.

- Accretion in ionised environments: despite the presence of ionising radiation, accretion can continue through disk structures. With ionised accretion flows playing a role in the growth of massive stars.

The discussion and comparison of the low and high-mass regimes is important to determine what information is still missing, and piece together why their formation mechanisms are different in some areas and not others. This thesis focuses exclusively on high-mass stars, mainly investigating their accretion mechanisms.

1.2.3 Filaments

Filamentary structures are recognised as fundamental components of the interstellar medium, forming a key part of the galactic ecosystem in which stars are born. For more information and support see reviews such as André et al. (2014), Schisano et al. (2020) and Hacar et al. (2023). These elongated, dense structures, are observed across a wide range of environments and physical scales – from small-scale filaments in star-forming regions to massive, kiloparsec-scale structures that trace spiral arms and galactic-scale flows (e.g., Goldsmith et al. 2008; Myers 2009; Jackson et al. 2010; Schneider et al. 2010; Henshaw et al. 2014; Beuther et al. 2020; Alves et al. 2020; Syed et al. 2022).

Filaments are also crucial in forming massive stellar clusters, as shown by studies such as André et al. (2010) and Schneider et al. (2010). Moreover, hub–filament systems, where multiple filaments converge onto a dense core, are commonly observed in massive star-forming complexes such as the DR21 ridge (Schneider et al., 2010), SDC335 (Peretto et al., 2013), and G33.92+0.11 (Liu et al., 2015). These junctions represent zones of enhanced mass accumulation.

Theoretical and numerical work supports the observational picture, showing that filament formation is a natural outcome of turbulent motions in the ISM, particularly when combined with self-gravity and magnetic fields (Padoan et al., 2001; Federrath, 2016; Clarke et al., 2017). Simulations further suggest that filaments are dynamically active structures, undergoing continuous mass accretion from their surroundings while simultaneously fragmenting to form stars (Gómez & Vázquez-Semadeni, 2014; Seifried & Walch, 2015).

In this thesis, filaments are treated not just as morphological features, but as physically significant structures that critically shape the conditions for star formation – particularly in high-mass environments. Their ability to concentrate material, and funnel it into hubs and onto cores, makes them key regulators of both the efficiency and scale of star formation. Understanding the physical properties, dynamics, and environmental context of filaments is therefore essential for developing a comprehensive model of how stars, especially massive ones, form and evolve.

1.2.4 Evolutionary sequence

Throughout this thesis, the observational data have been classified into distinct evolutionary stages to provide additional context for interpreting the results. This evolutionary sequence was derived using sources from the ATLASGAL survey and incorporates four key classification subsets. Further information and other classifications not a part of this evolutionary sequence are discussed in Urquhart et al. (2022). This sequence progresses from quiescent, to protostellar, then to young stellar objects (YSOs), and finally to HII regions. Figure 1.2 presents a schematic representation of the star formation process across these stages. The quiescent stage refers to a gravitationally bound, massive pre-stellar clump with no embedded point source detectable at any wavelength. This evolves into the protostellar phase, where the clump collapses and fragments into dense cores, each potentially forming protostars. As mass accumulates, the protostar begins heating its surrounding envelope.

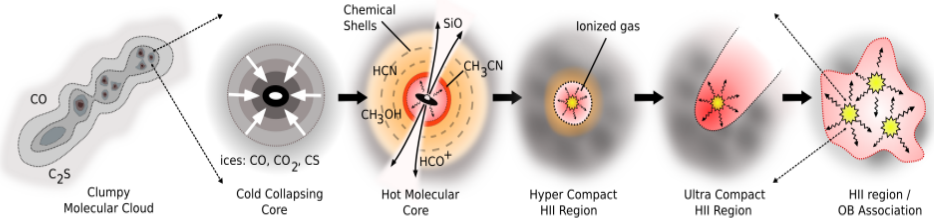

Figure 1.2: A schematic of the evolution from quiescent to HII region. Image credit: Cormac Purcell.

The transition from protostellar to YSO is gradual, marked by continued accretion rather than distinct physical changes (Urquhart et al., 2022; Wells et al., 2022). A more pronounced shift occurs with the formation of a H II region, signalling the end of the accretion phase and onset of dispersal. Once hydrogen burning begins, the protostar emits sufficiently ionising radiation to form a surrounding H II region. This initially appears as a hypercompact (HC) H II region and rapidly expands through the ultracompact (UC) and compact phases before ultimately breaking out of its natal clump and transitioning into the classical H II regions visible at optical wavelengths (Urquhart et al., 2014).

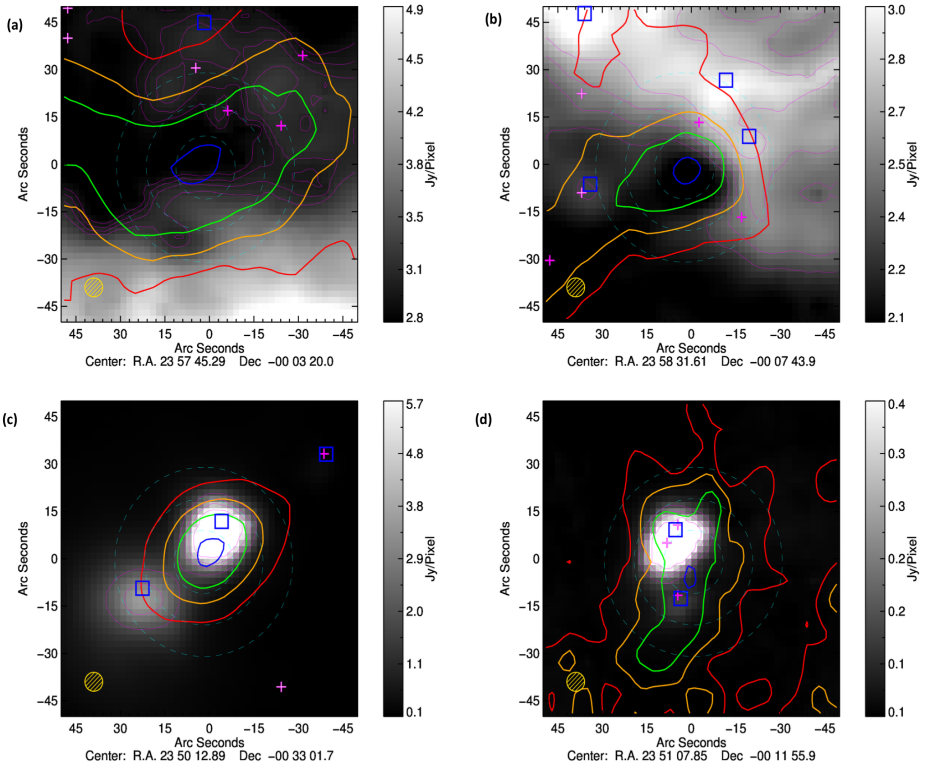

Figure 1.3: *Upper panels:* examples of 70 µm dark clumps (Quiescent) *Lower panels:* examples of 70 µm images of protostellar clumps. In all panels of there are blue, green, orange and red contour lines. These all represent percentages of the 70 µm dust emission associated with the clumps, red being 30 % orange being 50 %, green being 70 %, and blue is the sub-millimetre emission of the clump. In the images there are also two types of symbols, the pink + symbol shows MIPS point sources (Gutermuth & Heyer, 2015) and the blue squares show 70 µm point sources from the Hi-GAL catalogue (Elia et al., 2017).

The following paragraphs outline the specific criteria used to distinguish between quiescent, protostellar, YSO, and H II region sources. The process started with an initial classification specifying whether each source has an embedded source or not, before a second round to distinguish between protostellar, YSO and H II regions.

For a source to be classified as quiescent the image needs to be clean of extended emission that covers the peak of the clump, or 50 % of the clump as a whole. There must also be no 70 µm point source located within the 70 % contour line. In Fig. 1.3

the upper panels show sources that have been classified as quiescent. It can be seen that whilst there is some extended emission, the centre of the clump is not covered and the majority of the clump is free from any 70 µm emission, with no embedded objects anywhere in the image.

Any embedded source must be larger than nine pixels, as this ensures the source is larger than the beam, if an embedded source is smaller than the beam, it is likely to be spurious. It must also be circular in shape, and clearly distinguishable above any background emission; if this is the case, the source is classified as protostellar. The lower panels in Fig. 1.3 show protostellar sources that have a very distinct embedded point source at the centre of the clumps that is not obscured by any extended emission.

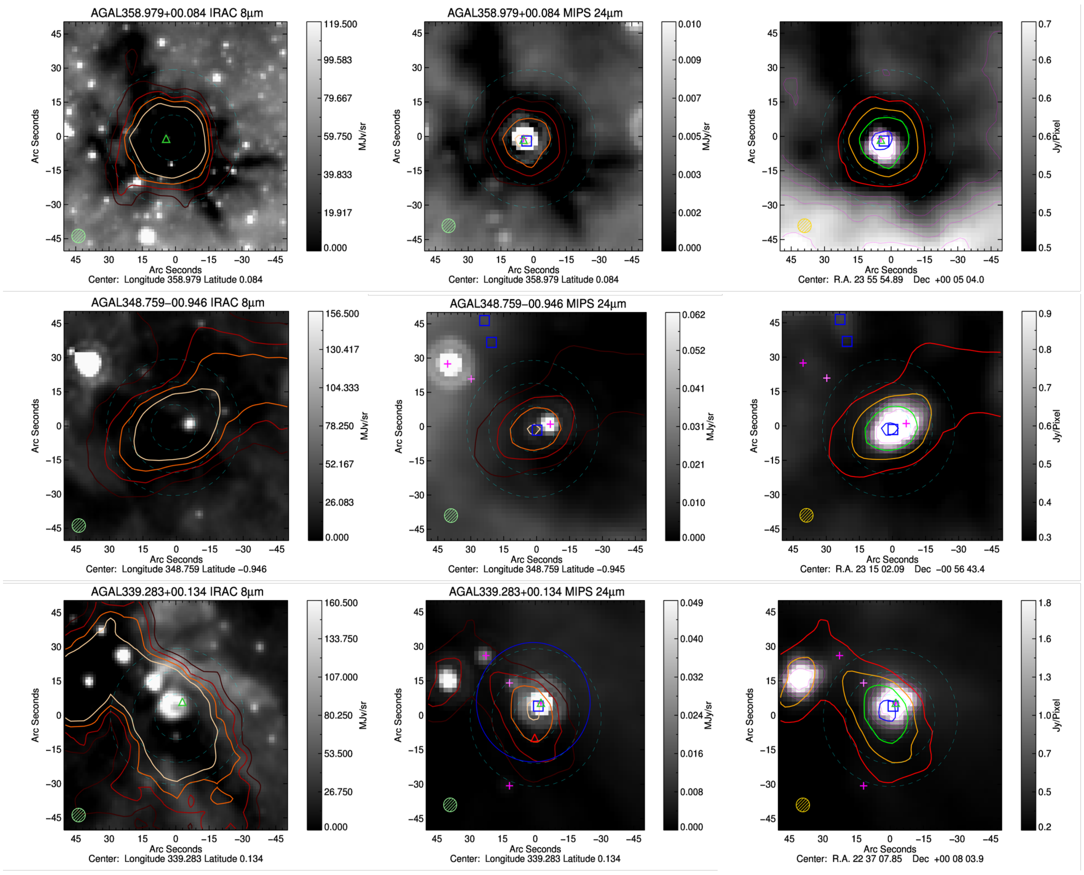

Figure 1.4: All of the images presented are 100 x 100″ in size and show the 30, 50, 70 and 90 % contour levels of the ATLASGAL 70 µm dust emission; these are colours red, orange, green and blue in the right image and dark red, red, orange and peach in the left and centre images. Panels on the right follow the same contour colour scheme as Fig. 1.3.

After an initial classification of either quiescent or protostellar the protostellar sources were investigated further to split them into protostellar, YSO or HII region, by looking at multiple wavelengths – namely, 8, 24 and 70 µm. Each one of these sources has different characteristics in each of these wavelengths, and there are also symbols that would indicate the presence of one these sources found by a different survey. For YSOs, there are orange filled circles, whilst for HII regions there are yellow crosses, these symbols appear in the 8 µm image only. Another indicator of Hii regions are blue circles in the 24 µm image.

Blue squares and magenta crosses mark the positions of 70 µm and 24 µm sources identified in the region; these are associated with embedded protostellar objects. For these sources to remain classified as protostellar, there must be a clearly distinguishable embedded source in the 70 µm image. There may also be an embedded object in the 24 µm image, but the embedded source must not be present in the 8 µm image for it to be classed as protostellar. The upper three panels of Fig. 1.4 shows the absence of a point source in the 8 µm (left panel) image but an embedded source in the 70 µm (right panel) image, and hence it is classified as protostellar.

For a source to be classified as either a YSO or a Hii region, there must be an embedded source in both the 70 and 24 µm images. The difference between these two classifications is the 8 µm image. For the source to be classified as a YSO, there must also be a corresponding point source in the 8 µm image. Figure 1.4 shows a point source in all three images (the three central panels) and hence this source is classified as a YSO.

Finally, for Hii regions the source will appear at all three wavelengths, similar to the YSOs, however the Hii regions will appear more diffuse in the 8 µm image in comparison to YSO sources which are much more compact. Hii regions will have a higher temperature; hence if there is any uncertainty, the temperature can be reviewed for additional information when making the classifications. Figure 1.4 (lower panels) shows this in the left panel and also shows a blue circle in the middle panel, which also suggests the presence of a Hii region.

This initial work, classifying a large portion of the ATLASGAL sources, laid the groundwork for the classification method and evolutionary sequence used throughout the thesis.

1.3 Observations

Around the world, numerous radio telescopes are currently operational, including interferometric arrays such as the Atacama Large Millimeter/submillimeter Array (ALMA), the Northern Extended Millimeter Array (NOEMA), and the Submillimeter Array (SMA), as well as single-dish telescopes like the IRAM 30m and APEX. These instruments have all significantly advanced the capabilities of the field and have majorly contributed to the results we have seen in the past 20 years. For example, programs such as ATLASGAL, CMZoom, CASCADE, EMERGE, ALMAGAL and ANTI-HEROES all use one, or in a few cases, multiple, of these instruments (e.g., Schuller et al. 2009; Battersby et al. 2020; Beuther et al. 2022; Hacar et al. 2024; Molinari et al. 2025; Gieser et al. in prep). The single dish telescopes excel in surveying large-scale structures, while interferometric arrays provide the resolution necessary for detailed imaging of compact objects. Together, these instruments provide a comprehensive view of different targets across a range of scales. The instruments used in this thesis are detailed in the following sections, along with a short discussion of commonly used spectral lines.

1.3.1 Single-dish telescopes

Figure 1.5: The IRAM 30m on top of on Pico Veleta during April 2024 observations.

The IRAM 30m telescope is a single-dish radio telescope located on Pico Veleta in the Sierra Nevada mountains of southern Spain, at an altitude of 2,850 meters. Completed in 1984, it is operated by the Institut de Radioastronomie Millimétrique (IRAM), and is a collaboration between France, Germany, and Spain. The IRAM 30m telescope is optimised for observations in the millimeter wavelength range (70–350 GHz). The primary reflector has a diameter of $D = 30$ m. The telescope's angular resolution θ is diffraction-limited, and in small-angle approximation given by:

$$\theta \approx 1.22 \frac{\lambda}{D}, \tag{1.3.1}$$

where λ is the observing wavelength. Larger dishes or shorter observational wavelengths improve the resolution. However, single-dish telescopes generally have lower resolving power compared to interferometric arrays, as their resolution is fundamentally limited by the physical size of the dish. Despite this limitation, single-dish telescopes are highly sensitive to large-scale ($>$1 pc) diffuse emissions, making them ideal for observing extended structures such as molecular clouds, and filamentary structures. The IRAM 30m telescope uses heterodyne receivers cooled to cryogenic temperatures to minimise thermal noise. The main receiver system, Eight MIxer Reciever (EMIR), operates simultaneously across multiple bands and polarisations. The incoming radio frequency (RF) signal is mixed with a local oscillator (LO) to produce an intermediate frequency (IF), according to:

$$\nu_{\mathrm{IF}} = |\nu_{\mathrm{RF}} - \nu_{\mathrm{LO}}|, \tag{1.3.2}$$

where ν_{IF} is the down-converted signal passed to the backend (IRAM has a few different ones but we will use the FTS backend in this explanation). The signal is digitised and processed by fast Fourier transform spectrometers (FFTS), which deliver high spectral resolution over broad bandwidths. The frequency resolution is defined as:

$$\Delta\nu = \frac{\nu}{R}, \tag{1.3.3}$$

where ν is the central frequency and R the spectral resolution. From this it is also helpful to calculate the velocity resolution;

$$\Delta v = c\, \frac{\Delta\nu}{\nu}, \tag{1.3.4}$$

commonly used for expressing channel width. The IRAM 30 meter telescope supports multiple observing strategies tailored to source type and atmospheric conditions. Common observing modes include:

- **Position switching:** alternating between the source and a nearby reference (off-source) position.
- **Frequency switching:** rapidly switching the LO frequency to sample baseline and line emission without moving the telescope.
- **On-the-fly (OTF) mapping:** continuous scanning across the source to cre-

ate maps for efficient wide-field imaging.

Single-dish telescopes are well-suited for observations covering broad areas of the sky or mapping extended sources. However, their sensitivity to noise from atmospheric and ground-based interference, combined with their limited resolution, restricts their utility for imaging fine details in compact or distant sources.

Chapter 4 of this thesis utilises data from a successful IRAM 30m proposal from the winter 2023 cycle (project code: 102-23). The observing setup used the E2 band, observing at 1.3 mm. The observations used the FTS200 backend, and the OTF mapping observing mode.

1.3.2 Interferometry

Figure 1.6: An impressive view of the ALMA array, in compact configuration, during a moonlit night, that anyways reveals a very starry sky in the Chajnantor Plateau. Credit: Alex Pérez

The Atacama Large Millimeter/submillimeter Array (ALMA), located in the Atacama Desert of northern Chile, is one of the most advanced examples of a radio interferometer. ALMA's high-altitude location and dry environment minimise atmospheric interference, enabling unprecedented sensitivity and resolution. Operational since 2013, ALMA is an international collaboration between the European Southern Observatory (ESO), the U.S. National Science Foundation (NSF), and the National Institutes of Natural Sciences (NINS) of Japan, in cooperation with Chile.

With up to 66 antennas distributed over baselines from 150 m to as long as 16 km, combining signals from multiple antennas, allows the array to achieve the angular resolution of a telescope with a diameter equal to the maximum antenna separation. Unlike single-dish telescopes, where angular resolution is limited by the diameter of a single reflector, interferometers use aperture synthesis to construct high-resolution images. The effective angular resolution of an interferometer is given by:

$$\theta \approx \frac{\lambda}{B_{\mathrm{max}}}, \tag{1.3.5}$$

where λ is the observing wavelength and B_{max} is the longest baseline in the array. Each antenna pair samples the sky's brightness distribution at one point in the (u, v)-plane. This plane represents the two-dimensional Fourier transform of the sky. As the Earth rotates, the projected baselines change, allowing the array to sample different points in the (u, v)-plane and effectively build up spatial frequency coverage of the source. According to the van Cittert–Zernike theorem, the visibility function $V(u,v)$ is related to the sky brightness distribution $I(l,m)$ by the two-dimensional Fourier transform:

$$V(u,v) = \iint I(l,m)\ e^{-2\pi i(ul+vm)}\ dl\ dm, \tag{1.3.6}$$

where (u, v) are the projected baseline coordinates, and (l, m) are the projections onto the celestial hemisphere. An image of the sky is then reconstructed via the inverse Fourier transform:

$$I(l,m) = \iint V(u,v)\ e^{2\pi i(ul+vm)}\ du\ dv. \tag{1.3.7}$$

The (u, v)-plane is not fully sampled in practice, so resulting image (the dirty image) is the convolution of the true sky brightness with the beam — the point spread function of the interferometer. To recover the true image, deconvolution algorithms such as CLEAN (Högbom, 1974) are used to remove the side lobes and reconstruct the underlying emission. This data is then transmitted to a central correlator, which calculates the cross-correlations (visibilities) between all antenna pairs. The resulting visibility data are calibrated and imaged using dedicated software such as CASA (CASA Team et al., 2022). Interferometers have a limited ability to detect large-scale, diffuse emissions due to their reliance on spatial frequencies corresponding to the separations between dishes. This is known as the missing short-spacings, and can be a problem in the final data product, which can be mitigated by combining interferometric data with observations from single-dish telescopes.

Data used in Chapter 2 and Chapter 4 come from the ALMA large program ALMAGAL (the ALMA evolutionary study of high mass protocluster formation in the Galaxy). These are a combination of observations from three different ALMA array configurations: two configurations of the main 12m ALMA array and one from the 7m Atacama Compact Array. This combination allows for angular scales ranging from 0.3″ to 10″.

1.3.3 Molecular line emission

Table 1.1: Protostar tracers - mm/submm

Molecule	Used for	Reference
CO	Low density probe	Liu et al. (2013)
$C^{18}O$	Envelope tracer	Tychoniec et al. (2021)
OH	Magnetic field probe	Stahler & Palla (2004)
NH_3	Temperature probe	Ho & Townes (1983)
SiO	Outflow shock tracer	Vasyunina et al. (2011)
SO	Outflow shock tracer	Tychoniec et al. (2021)
H_2O	Warm gas probe	van Dishoeck et al. (2021)
CH_3OH	Dense gas tracer, outflow tracer and temperature probe,	Tychoniec et al. (2021)
CH_3CN	Temperature probe in hot cores, and warm dense regions	Vasyunina et al. (2011)
N_2H^+	Quiescent gas tracer for structure and kinematics	Vasyunina et al. (2011)
$CS/^{13}CS$	High density tracer	Vasyunina et al. (2011)
HC_3N	Low optical depth, dense gas tracer	Vasyunina et al. (2011)
HNC	Dense gas tracer, HCN/HNC ratio depends on temperature	Vasyunina et al. (2011)
HCO^+	Dense gas of embedded molecular outflows	Vasyunina et al. (2011)
$H^{13}CO^+$	Mostly optically thin, similar to HCO^+ -	Vasyunina et al. (2011)
HCN	High density gas tracer, infall in low mass SF	Vasyunina et al. (2011)
$H^{13}CN$	High density gas tracer	Vasyunina et al. (2011)
C_2H	Traces early stages	Vasyunina et al. (2011)
CH_3C_2H	Traces dense gas and temperature	Vasyunina et al. (2011)
H_2CO	Probe of density and kinematic temperature in dense cores	Tychoniec et al. (2021)
DCO^+	Cold gas tracer	Caselli et al. (2002)
DCN/DNC	Dense cold gas	Gerner et al. (2015)

To interpret the physical and chemical properties of the ISM, observations of emission lines in the mm and submm regimes provide essential diagnostics. These spectral lines arise from a variety of atomic and molecular species. Each traces different conditions such as density, temperature, ionisation, and kinematics. In particular, mm and submm wavelengths are suitable for probing cold and dense regions of gas and dust, often obscured at optical wavelengths, making them especially valuable for studying star-forming environments, molecular clouds, and galaxy evolution. Table 1.1 lists a selection of commonly used mm and submm molecular lines relevant to protostar studies, along with the physical processes or conditions they trace. It includes molecules like CO and its isotopologues, which serve as general tracers of gas mass and structure, as well as more specialised species like SiO and CH_3OH that highlight energetic processes such as shocks and outflows. By combining information from these diverse tracers, we can construct a more complete picture of the physical conditions and dynamic processes shaping protostellar evolution. Chapters 2 and 4 both make use of observational lines for their analysis. Chapter 2 focusing on H_2CO and SiO and Chapter 4 focusing on $C^{18}O$. Missing short baselines can result in the loss of flux from extended emission. This issue does not affect data from the IRAM 30m, but it can affect ALMA observations. To address this, we carefully inspected the spectral lines, and our analysis and reasoning behind choice of molecular lines is detailed in the respective chapters.

1.4 Flow rate equation

In this subsection, the formula used for the measurement of the flow rates along filamentary structures throughout this thesis is derived and explained from first principles. Starting from mass conservation in hydrodynamics, namely the continuity equation

$$\frac{\partial}{\partial t}\rho + \nabla \cdot (\rho \boldsymbol{v}) = 0 \tag{1.4.1}$$

with the density ρ and the velocity $\boldsymbol{v}$. If the filament is represented as a cylindrical object, and checked for the temporal change of mass within a section of the cylinder of real length w_r and fixed volume V, we can take the volume out of the time derivative:

$$\frac{\partial}{\partial t} M_V = \dot{M}_V = -V \nabla \cdot (\rho \boldsymbol{v}) \tag{1.4.2}$$

We assume the medium density to be uniform along the spatial scale of interest w_r, we take the density out of the spatial derivative, and the volume V cancels out:

$$\dot{M}_V = -M_V \nabla \cdot \boldsymbol{v} \tag{1.4.3}$$

For a one-dimensional flow along the filament, we can approximate the divergence of the velocity field $\nabla \cdot \boldsymbol{v}$ as the velocity difference $\Delta v_{\mathrm{out-in}}$ of the flow out of the section of length w_r and into it:

$$\dot{M}_V = -M_V \frac{\Delta v_{\mathrm{out-in}}}{w_r} \tag{1.4.4}$$

Eq. (1.4.4) represents the mass conservation within the section w_r of the filament. As an example: for a uniform velocity field, the inflow and outflow velocities are identical $\Delta v_{\mathrm{out-in}} = 0$ and the mass within the section remains unchanged. To obtain a formula for the flow rate $\dot{M}_r$, we have to substitute the velocity difference by the absolute, local velocity v_r of the flow (subscript "r" meaning the real values and subscript "obs" the corresponding observed values):

$$\dot{M}_r = M_V \frac{|v_r|}{w_r} \tag{1.4.5}$$

Here, we included the convention that the flow rate is always treated as a positive value, regardless if the flow is pointing towards the observer or away from the observer.

So far, we have discussed the system only in its local (unobserved) properties. The absolute, local velocity v_r can be obtained from the observational data by subtracting the systemic velocity v_{sys} from the observed velocity v_{obs} with $\Delta v_{\mathrm{r}} = |v_{\mathrm{obs}} - v_{\mathrm{sys}}|$:

$$\dot{M}_r = M_V \frac{\Delta v_{\mathrm{r}}}{w_r}. \tag{1.4.6}$$

The mass M_V can be approximated by the column density Σ times the beam. Since we use $1''$ length scale, roughly a beam width, we can approximate the beam with

$$A_{\text{beam}} \sim w_{\text{obs}}^2. \tag{1.4.7}$$

Substituting in the beam area we get

$$M_V = \Sigma_{\text{obs}} \cdot A_{\text{beam}} = \Sigma_{\text{obs}} \cdot w_{\text{obs}}^2, \tag{1.4.8}$$

where we chose our measured length scale as the size of the beam. Including now the inclination dependence of the observed parameters:

$$\Delta v_{\text{r}} = \frac{\Delta v_{\text{obs}}}{\sin i} \tag{1.4.9}$$

and

$$w_{\text{r}} = \frac{w_{\text{obs}}}{\cos i}. \tag{1.4.10}$$

Substituting Equations (1.4.8)-(1.4.10) into Equation (1.4.6) we get

$$\dot{M}_r = \Sigma_{\text{obs}} \cdot w_{\text{obs}}^2 \cdot \frac{\Delta v_{\text{obs}}}{w_{\text{obs}}} \cdot \frac{\cos i}{\sin i}, \tag{1.4.11}$$

which in its final form is

$$\dot{M}_r = \Sigma_{\text{obs}} \cdot \frac{\Delta v_{\text{obs}}}{\tan(i)} \cdot w_{\text{obs}}. \tag{1.4.12}$$

1.5 Theoretical simulations

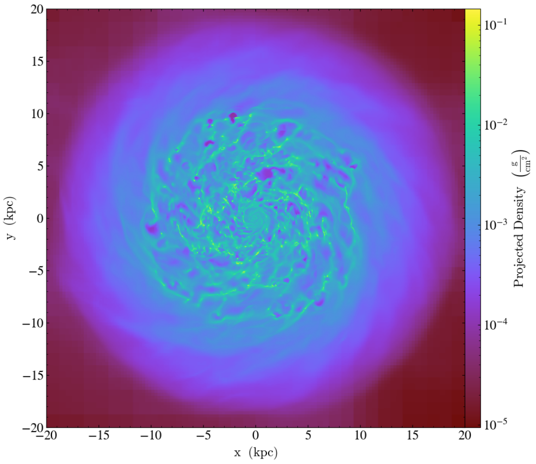

Figure 1.7: Column density map of the simulated galaxy at an age of 283 Myr, produced from Zhao et al. (2024). The view is limited to a 40 x 40 kpc box, showing both the dense and diffuse gas portions of the disk.

In addition to observational data, this thesis makes use of theoretical simulations to help interpret physical conditions and processes that are difficult to access observationally, particularly in the early stages of high-mass star formation. These simulations serve as a controlled laboratory to explore the role of filamentary flows in high mass star forming regions.

The simulations from Zhao et al. (2024), used to create the synthetic observation data cubes used in Chapter 3, model the evolution of a Milky Way-type galaxy using the RAMSES code, a publicly available adaptive-mesh-refinement (AMR) simulation framework (Teyssier, 2002), the simulated galaxy can be seen in Fig. 1.7. RAMSES is well-suited for studying galaxy formation and evolution, as it solves the magnetohydrodynamics equations while dynamically refining the computational grid in regions of interest. This allows for efficient high-resolution modelling of complex astrophysical processes. The code includes modules for star formation via star particles, stellar feedback, metal cooling, magnetic fields, and clump-finding algorithms. Gas cooling is handled using the GRACKLE cooling library, which incorporates pre-tabulated metal line cooling rates derived from CLOUDY models, along with photoelectric heating at a fixed rate. A temperature floor of 10 K is enforced, below which the cooling routines become unreliable for diffuse gas. Gravity and softening are treated using standard RAMSES methods, and a non-thermal Jeans pressure floor is applied to prevent artificial fragmentation due to unresolved pressure gradients. A weak magnetic field is initialised, scaling with gas density, and is initially set well below equipartition, allowing for saturation through dynamo processes. Star formation occurs stochastically in regions where the number density exceeds 100 cm^{-3}, following a Schmidt law with a star formation efficiency per freefall time of $\epsilon_* = 0.1$. Supernova feedback is implemented using the delayed-cooling method (Agertz et al., 2011), in which thermal energy is deposited into the surrounding gas and evolves adiabatically before cooling resumes. The disk is evolved for 200–300 Myr at a maximum resolution of 4.58 pc, reaching a quasi-equilibrium state with a self-regulated star formation rate of approximately $5\,\mathrm{M}_\odot\,\mathrm{yr}^{-1}$.

At the end of the large-scale simulation, the galactic disk exhibits a rich, multiphase ISM composed of spiral arms, dense filamentary structures, and hot bubbles driven by supernova feedback. These features emerge naturally from the interplay of gravity, cooling, magnetic fields, and feedback processes. The self-regulated star formation results in realistic global properties, while the turbulent ISM remains highly structured and dynamic.

Using a zoom-in region, the simulation captures the fine-scale morphology of turbulent gas, revealing the formation and evolution of dense clumps and structures analogous to giant molecular clouds (GMCs). These structures are shaped by the combined effects of local self-gravity, turbulent compression, and magnetic support. Although the short zoom-in duration does not include the onset of new star formation, the simulation provides valuable insight into the physical conditions and processes that precede it. The two-stage simulation approach — a global disk evolution followed by localised, high-resolution zoom-ins — offers a powerful framework for understanding star-forming environments in the broader galactic context.

1.6 Scientific motivation

The movement of material towards GMCs, filament intersections, clumps, or small scale cores plays a major role in how the star formation in these regions plays out. The nature of these flows influences how and when stars form, how mass is distributed, and how efficiently gas is converted into stars. This thesis investigates the broad question;

What are the properties of accretion flows in and onto star-forming clusters?

Despite their importance, accretion flows are challenging to measure observationally, and many questions remain. How do flow properties vary with distance, mass, or evolutionary stage? How much does environment affect the observed flow rates? And how do these flows behave across different spatial scales? This thesis seeks to address these questions using a combination of large-sample observations, synthetic observations of simulations, and multi-scale datasets.

Each chapter contributes a different perspective to answering the overarching question:

- Chapter 2 examines a large sample of ~ 180 cores to investigate the characteristics of accretion flows onto individual cores. It explores how flow rates vary with distance from the core, core mass, and evolutionary stage, offering insight into which factors have the strongest influence on the behaviour of the flows.

- Chapter 3 uses theoretical simulations of star-forming regions in two different environments to test the robustness of observational techniques and to examine how these different galactic environments shape the properties of the flows. This chapter also assesses the impact of unknown inclination angles – an uncertainty in observational data that is well-constrained in simulations – on the derived flow rates.

- Chapter 4 addresses the question of scale by examining flows across multiple spatial levels. Using unique data from ten regions observed at three distinct spatial resolutions, this chapter evaluates whether the relationships between flow rates and physical parameters are consistent or change with different spatial scales.

Together, these chapters aim to build a comprehensive understanding of how material flows shape the formation and evolution of star-forming clusters.

2

ALMAGAL: FLOWS ALONG FILAMENTARY STRUCTURES

M. R. A. Wells, *H. Beuther, S. Molinari, P. Schilke, C. Battersby, P. Ho, Á. Sánchez-Monge, B. Jones, M. B. Scheuck, J. Syed, C. Gieser, R. Kuiper, D. Elia, A. Coletta, A. Traficante, J. Wallace, A. J. Rigby, R. S. Klessen, Q. Zhang, S. Walch, M. T. Beltrán, Y. Tang, G. A. Fuller, D. C. Lis, T. Möller, F. van der Tak, P. D. Klaassen, S. D. Clarke, L. Moscadelli, C. Mininni, H. Zinnecker,d Y. Maruccia, S. Pezzuto, M. Benedettini, J. D. Soler, C. L. Brogan, A. Avison, P. Sanhueza, E. Schisano, T. Liu, F. Fontani, K. L. J. Rygl, F. Wyrowski, J. Bally, D. L. Walker, A. Ahmadi, P. Koch, M. Merello, C. Y. Law, L. Testi*

The following Chapter is based on the work ***Dynamical Accretion Flows - ALMAGAL: Flows along filamentary structures in high-mass star-forming clusters*** published in the October, 2024 issue of Astronomy&Astrophysics (Wells et al., 2024). I led this work under the supervision of Henrik Beuther and in collaboration with the ALMAGAL consortium where I conducted all scientific analysis. I created all figures and tables and wrote all text for the paper with help from Rolf Kuiper for the inclination analysis. All co-authors provided comments and feedback for the manuscript.

ABSTRACT

Investigation of the flow of material along filamentary structures towards the central core can help provide insight into high-mass star formation and evolution. Our main motivation is to answer the question: what are the properties of accretion flows in star-forming clusters? We use data from the ALMA Evolutionary Study of High Mass Protocluster Formation in the Galaxy (ALMAGAL) survey to study 100 ALMAGAL regions at $\sim 1''$ resolution located between ~ 2 and 6 kpc distance. Making use of the ALMAGAL ~ 1.3 mm line and continuum data we estimate flow rates onto individual cores. We focus specifically on flow rates along filamentary structures associated with these cores. Our primary analysis is centered around position velocity cuts in H_2CO ($3_{0,3}$ - $2_{0,2}$) which allow us to measure the velocity fields, surrounding these cores. Combining this work with column density estimates we derive the flow rates along the extended filamentary structures associated with cores in these regions. We select a sample of 100 ALMAGAL regions covering four evolutionary stages from quiescent to protostellar, Young Stellar Objects (YSOs), and HII regions (25 each). Using dendrogram and line analysis, we identify a final sample of 182 cores in 87 regions. In this paper, we present 728 flow rates for our sample (4 per core), analysed in the context of evolutionary stage, distance from the core, and core mass. On average, for the whole sample, we derive flow rates on the order of $\sim 10^{-4}$ $M_\odot\,yr^{-1}$ with estimated uncertainties of ± 50 %. We see increasing differences in the values among evolutionary stages, most notably between the less evolved (quiescent/protostellar) and more evolved (YSO/HII region) sources and we also see an increasing trend as we move further away from the centre of these cores. We also find a clear relationship between the calculated flow rates and core masses $\sim M^{2/3}$ which is in line with the result expected from the tidal-lobe accretion mechanism. The significance of these relationships is tested with Kolmogorov-Smirnov and Mann-Whitney U tests. Overall, we see increasing trends in the relationships between the flow rate and the three investigated parameters; evolutionary stage, distance from the core, and core mass.

2.1 Introduction

The formation and evolution of high-mass stars has been the subject of intense scientific interest for decades. High-mass stars play a crucial role in shaping not only their parental clouds but also the interstellar medium on kpc scales, enriching it with heavy elements, and influencing the dynamics of their surrounding environments via the energy they release through radiation and stellar winds (e.g., Kahn 1974; Yorke & Kruegel 1977; Wolfire & Cassinelli 1987; Zinnecker & Yorke 2007; Arce et al. 2007; Frank et al. 2014; Smith et al. 2009; Zhang et al. 2015; Motte et al. 2018; Kuiper & Hosokawa 2018). This in turn triggers new waves of star formation and helps sculpt the physical conditions of the Interstellar Medium (ISM) in galactic disks. Therefore, understanding the intricate processes involved in the birth and subsequent evolution of high-mass stars is fundamental not only for stellar physics but also for comprehending the broader aspects of galaxy formation and evolution. High-mass stars are rare due to their short lifetimes and comparatively low numbers when compared to low-mass stars. Looking at the initial mass function (IMF) we see one reason they are in limited numbers is that the IMF at high mass values follows a power law (e.g, Salpeter 1955; Bonnell et al. 2007; Offner et al. 2014). Moreover, high-mass stars typically stay embedded in their natal clusters until they reach the main sequence, making it much more difficult for us to study and constrain how they form and evolve. This leaves us with a large knowledge gap in not only star formation but astrophysics in general.

What we do know, is that the most common place for star formation to occur is in clustered environments inside giant molecular clouds (GMCs) (e.g., Lada & Lada 2003; Bressert et al. 2010). These are immense reservoirs of cold, dense gas and dust that provide the material for new generations of stars. Molecular clouds are commonly described to have a hierarchical structure (e.g, Scalo 1985; Thomasson et al. 2022). Following Williams et al. (2000) and Beuther et al. (2007) these clouds host massive condensations of gas called clumps ($\sim 1\,\mathrm{pc}$), which form clusters, within which more compact cores ($\sim 10\,000\,\mathrm{au}$) are observed that form gravitationally bound single, binary, or multiple systems. The process begins with the fragmentation of these GMCs due to gravitational instabilities, resulting in the formation of clumps and cores (e.g., Zinnecker 1984; Bonnell et al. 2003; Traficante et al. 2017; Urquhart et al. 2018; Svoboda et al. 2019). The extreme pressures and temperatures within these cores facilitate the collapse of material, leading to the creation of protostellar objects. The rapid accretion of surrounding material onto these protostars can trigger the release of intense radiation and powerful outflows, establishing an intricate balance between inward gravitational forces and outward pressure. The interplay of physical forces during high-mass star formation contributes to the observed clustering of these stars. These clusters play a crucial role in shaping the subsequent evolution of the stars within them, as well as the galaxies in which they reside (e.g, McKee & Tan 2003; Zinnecker & Yorke 2007).

One of the key components that profoundly influences the high-mass star formation process is the filamentary structure prevalent in molecular clouds. These elongated, thread-like structures, have been observed in various molecular tracers and continuum emission, indicating their essential role in the formation and distribution of high-mass stars assisting in the flow of material onto individual cores (e.g, Goldsmith et al. 2008; Myers 2009; André et al. 2010; Schneider et al. 2010). Accretion is a central process in the early stages of star formation. By examining how mass flows onto a core, the mechanisms driving their growth can be investigated. Understanding the interplay between accretion, radiation pressure, and other physical processes provides a clearer picture of how these massive objects form from their natal material. Filamentary structures have been found on many spatial scales, a full review of the filamentary ISM can be found in (e.g, Hacar et al. 2023; Schisano et al. 2020). Notable Galactic scale structures, extended up to tens and even more than hundreds of parsecs, include "Maggie" (Syed et al., 2022), "Nessie" (Jackson et al., 2010), and the Radcliffe wave (Alves et al., 2020). On smaller scales, the filamentary structures prevalent in molecular clouds and their surrounding have been studied too, some examples include Serpens South (Kirk et al., 2013), G035.39 00.33

(Henshaw et al., 2014) and infrared dark cloud G28.3 (Beuther et al., 2020); with mass accretion estimates on the order of 10^{-5} $\mathrm{M}_\odot\,\mathrm{yr}^{-1}$ for all three studies. Previous examples of flow rate analysis carried out with the Atacama Large Millimetre Array (ALMA), are seen in the works from Peretto et al. (2013), Sanhueza et al. (2021), Redaelli et al. (2022), and Olguin et al. (2023) all giving estimates on the order of 10^{-4} $\mathrm{M}_\odot\,\mathrm{yr}^{-1}$.

Evidence for both radial and longitudinal flows have been observed, each representing different kinds of material transport. Radial traces flows from the environment onto the filament and help build up its mass, however longitudinal flows trace flows along the filament and onto cores, building up the core mass. The kinematic molecular gas study done by Tackenberg et al. (2014) complimenting work done on 16 high-mass star-forming regions from the *Herschel* key project The Earliest Phases of Star formation (EPoS) shows that profiles perpendicular to the filament have almost constant velocities and that the velocity gradient occurs predominantly along the filament. Regions often have unique filamentary structures, but in most cases, velocity gradients can be identified along these filamentary structures towards the central hubs of clumps, which allows mass accretion estimates to be calculated. Looking at derived parameters throughout the stages of evolution can provide constraints for theoretical models. It is especially important to investigate all aspects of the high-mass star formation process throughout the complete evolutionary sequence so that we can compare and analyse how these results change through the lifetimes of (proto)stars.

In this paper we use a subset of the regions from the ALMA Evolutionary study of High Mass Protocluster Formation in the Galaxy (ALMAGAL) survey (Molinari et al. in prep) (see Sect. 2.2.1) to investigate properties of flow rates, focusing on longitudinal flows along filamentary structures towards the high-mass cores. Making use of selected spectral lines we estimate flow rates onto individual cores as a function of the evolutionary stage (see Sect. 2.2.3), distance from the cores or core masses. Qualitative and quantitative results are discussed in the context of high-mass star-forming clusters. The structure of the paper is as follows: the survey introduction and overview are given in Sect. 2.2.1. In Sect. 2.2 we introduce the sample along with how and why the regions were selected. In Sect. 2.2.5 we investigate the selected cores in more detail looking at signs of potential outflow signatures and line properties for velocity estimation. Details of how the flow rate calculation is done with detailed parameter descriptions are presented in Sect. 2.3. Sect. 2.4 presents the results of this calculation on our sub-sample before discussions in Sect. 2.5 including an expansion to theory and a wider context. We draw our conclusions in Sect. 2.6 and discuss opportunities for future work.

2.2 Sample selection

For this analysis, we choose a smaller subset of 100 regions for a focused study on flow rates and the relationship between them and other core properties. These sources were selected visually based on having strong continuum and line emission so that the initial sample includes 25 regions from each of the 4 evolutionary stages (quiescent, protostellar, Young Stellar Object (YSO), and Hii region, see Sect. 2.2.3).

2.2.1 ALMAGAL survey details

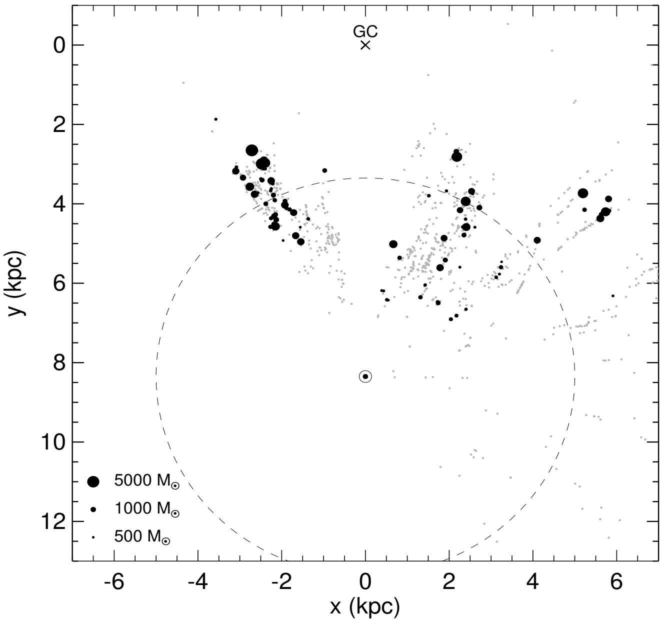

Figure 2.1: Source distribution for the regions in our ALMAGAL sub-sample is shown as black dots. The size of the markers scales with the masses of the ALMAGAL clumps. Grey dots are the rest of the ALMAGAL survey and the dashed line is a heliocentric distance circle at 5 kpc.

Table 2.1: Observational parameters

Parameter	Value
Mean beam size	$0.8''$
Continuum RMS	$\sim 0.15\,\mathrm{mJy/beam}$
H_2CO ($3_{0,3}$ - $2_{0,2}$) RMS	$\sim 9\,\mathrm{mJy/beam}$
SO (6_5 - 5_4) RMS	$\sim 5\,\mathrm{mJy/beam}$
Velocity resolution	$\sim 488\,\mathrm{kHz} \sim 0.7\,\mathrm{km\,s^{-1}}$

The ALMAGAL survey (2019.1.00195.L; PIs: Sergio Molinari, Peter Schilke, Cara Battersby, Paul Ho) is a large program approved during in ALMA Cycle 7. The ALMAGAL targets consist of 1013 compact dense clumps, covering different evolutionary stages, the majority being selected from the Herschel Hi-GAL survey

(Molinari et al. 2010a; Elia et al. 2017, 2021), with $\sim$ 100 regions come from the Red MSX Source (RMS) survey (Hoare et al. 2005; Urquhart et al. 2007; Lumsden et al. 2013). The 1017 targets are spread across the Galaxy. Figure 2.1 shows their distribution in the face-on view of the Galactic plane. The 1017 regions were observed in ALMA band 6 at frequencies from 217 to 221 GHz (corresponding to 1.3 mm). Information about the observations, data reduction and image generation are presented and discussed in more detail in the ALMAGAL data reduction paper (Sanchez-Monge et al., in prep). Here, we present a brief description of those aspects relevant for the scientific analysis of this work. The ALMAGAL spectral setup was designed to have four different spectral windows, two of them covering a broad frequency range of 2x 1.875 GHz being sensitive to the continuum emission, as well as many spectral lines at low spectral resolution ($1.3\,\mathrm{km\,s^{-1}}$); and two narrower spectral windows (2x 0.468 GHz) aimed at studying specific molecular species (e.g., H_2CO, CH_3CN) at higher spectral resolution ($0.3\,\mathrm{km\,s^{-1}}$). In this work, we make use of the spectral lines H_2CO ($3_{0,3}$ - $2_{0,2}$) at 218.222 GHz and SO SO (6_5 - 5_4) at 219.949 GHz. The ALMAGAL observations made use of three different array configurations to observe each source, including two different configurations of the main 12m ALMA array, and observations with the 7m Atacama Compact Array. This allows observations sensitive to angular scales from $0.1''$ up to $10''$. The data products used in this work are images with combined data from the 7m array (7M hereafter) and the most compact 12m array configuration (TM2 hereafter). We note that this work does not make use of the most extended array configurations available within the ALMAGAL project. The resulting images have angular resolutions of $0.5 - 1.0''$, depending on the distance of the source, which result in similar linear resolutions of 5000 au for all the targets. See Table 2.1 for details on typical observational parameters. The entire survey, including full observational details, is described in Molinari et al. (in prep.) while the details of the data-reduction pipeline are in Sanchez-Monge et al. (in prep.).

2.2.2 Sample

Looking at our sample compared to the whole survey we check how the mass, luminosity, luminosity-to-mass ratio and distance distributions compared to each other and whether there were signs of any bias. We see no signs of bias in distance, luminosity or luminosity to mass ratio. For the mass we specifically chose regions over $500\,\mathrm{M_\odot}$ and so this is reflected here. Histograms of these distributions can be found in A.1. For more information on how the survey parameters were calculated we refer to Molinari et. al (in prep.), but as an overview, the distances were derived with the Mège et al. (2021) method using the ALMAGAL spectral cubes and following this the distance dependent quantities were calculated.

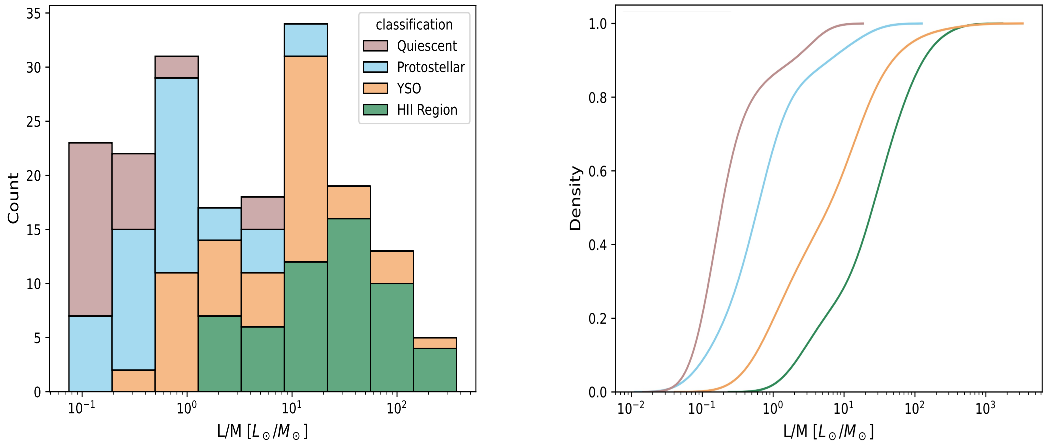

(a) Stacked histogram

(b) Cumulative distribution function

Figure 2.2: Colour coding for both figures is on evolutionary stage, legend shown in panel (a). These plots show the sample of 17 quiescent, 23 protostellar, 22 YSO and 25 HII regions. (a) Stacked histogram distribution of the luminosity-to-mass ratio for the regions in the ALMAGAL sub-sample being used for this work. (b) Individual cumulative distribution functions (CDF) of regions in each evolutionary stage, generated from kernel density estimates (KDEs) of the data shown in (a).

2.2.3 Evolutionary stage

Before selecting the regions for the analysis, the ALMAGAL sample is classified by evolutionary sequence. We use the sequence and classification scheme defined by Urquhart et al. (2022), which divides the sources into four evolutionary stages; Quiescent, Protostellar, Young Stellar Object (YSO), and HII regions. The classification is done by looking at the sources at three wavelengths: Hi-GAL 70 µm (Elia et al., 2017), MIPSGAL 24 µm (Carey et al., 2009), and GLIMPSE 8 µm (Churchwell et al., 2009). Quiescent sources have a central area free of emission at all three wavelengths. For protostellar sources, there is a point source in the 70 µm image, potentially a 24 µm counterpart but the source is not visible in the 8 µm image. A YSO is detected as a point-like source at all 3 wavelengths. HII regions also have a point source at all three wavelengths but the source in the 8 µm image becomes more extended and 'fluffy'.

Initially, the ALMAGAL sample was cross-matched with the ATLASGAL (Schuller et al. 2009; Urquhart et al. 2018, 2022) sample to see how many sources overlap and how many classifications can be immediately adopted. Cross-matching on Galactic coordinates with an error margin of 40″ leads to an initial match of roughly 600 regions out of 1013. The remaining ALMAGAL regions were classified visually according to the same rules as described above.

As an alternative evolutionary indicator, one can also look at the luminosity-to-mass ratio. This ratio increases with time, being very low in the early quiescent stage (e.g., Molinari et al. 2019; Elia et al. 2021). The distribution of the regions in

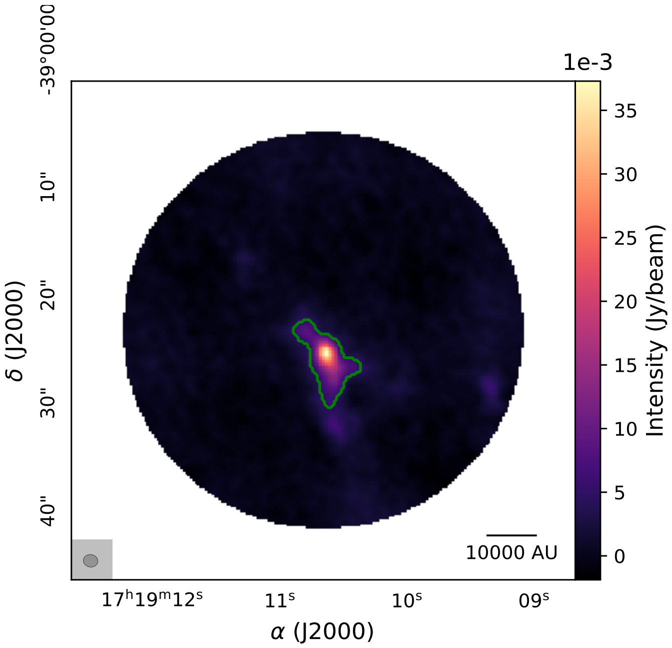

Figure 2.3: Continuum image of ALMAGAL source AG348.5792-0.9197 from the `astrodendro` package where the green contours indicate the "leaves" which are the areas we focus on here, the cores.

each classification stage can be seen in Fig. 2.2a which shows the peak luminosity-to-mass ratio progression as the cores become more evolved. Figure 2.2a enables a comparison of our evolutionary sequence with this evolutionary indicator, and as expected the two classification schemes roughly agree, with some overlap. This can also be seen in Fig. 2.2b showing a cumulative distribution. These classifications are done for the entire cluster-forming clump. However, within individual ALMAGAL regions, HII regions, YSO, Protostellar, and even Quiescent regions often co-exist. Examples of this include NGC6334I (e.g., Beuther et al. 2005), G29.96+0.02 (e.g., Cesaroni et al. 1998), or ISOSS J23053+5953 (Gieser et al., 2022).

2.2.4 Core identification

Each source in the subset of our ALMAGAL sample contains up to seven cores identified via the following process. We used the `astrodendro`[1] program on the continuum data for core identification, obtaining the peak position of these identified cores and estimating their peak and integrated flux density values. The `astrodendro` package allows us to break down the hierarchical structures in our observational data. The highest hierarchical level for each structure is a "leaf" (i.e a structure with no substructure), these correspond to what we define as a core. We can see an example of a "leaf" in Fig 2.3, which shows the case of source AG348.5792-0.9197. The three main input parameters of `astrodendro` are *min_value* (the minimum pixel intensity to be considered), *min_delta* (the minimum height for any local

---

[1] http://www.dendrograms.org/

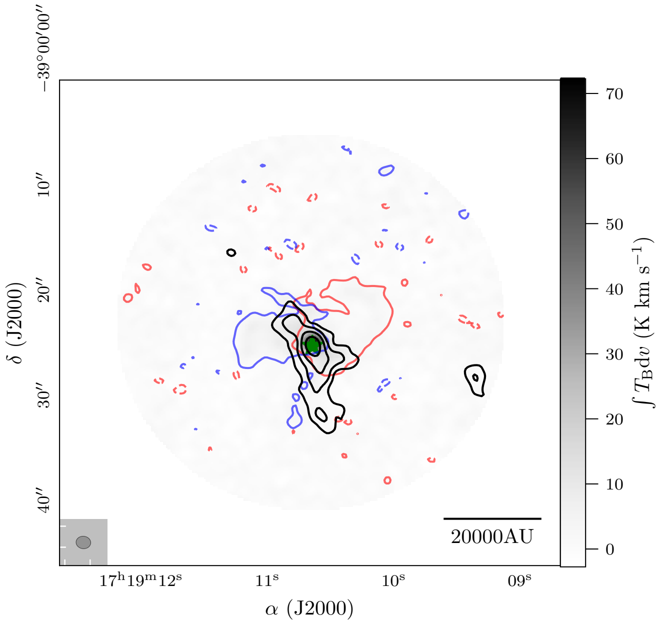

Figure 2.4: 0th moment map of SO (6_5 - 5_4) in grey-scale for source AG348.5792-0.9197 overlaid with continuum contours in black (levels 3,6,9 $\sigma_{\rm cont}$). A green star to show the peak intensity position of the core. Red and blue contours show the "wings" of the spectral line emission, from 3 to 20 $\rm km\,s^{-1}$ either side, with respect to the region velocity of rest.

maximum to be defined as an independent entity), and *min_npix* (the minimum number of pixels for a leaf to be defined as an independent entity). We decided to have a large significance level for the cores to be identified so that we were left dealing with just the cores themselves and their structures and not the extended parental cloud. We use *min_value* = 5 $\sigma_{\rm cont}$, *min_delta* = 5 $\sigma_{\rm cont}$ and *min_npix* = beam area. With the combination of our choices of *min_value* and *min_delta*, all cores have a peak flux density $\geq$ 10 $\sigma_{\rm cont}$. Here $\sigma_{\rm cont}$ or $\sigma_{\rm line}$ are the rms values of either the continuum image or the spectral cube for the lines being used. Running the analysis with these parameters we identify 203 cores within the 100 regions. Of these 100 regions, five regions had no cores identified with our criteria, so these were removed from the sample leaving an initial 95 regions with 203 cores. The official core catalogue for ALMAGAL calculated on the final data products, including also more extended ALMA configurations, will be available in Coletta et al. (in prep.).

2.2.5 Analysis

We start the analysis with a detailed look into the main lines suitable for identifying outflows, such as SiO (5 - 4) and SO (6_5 - 5_4) and making Position-Velocity (PV) cuts along the filamentary structures surrounding each core (identified visually from the continuum contours which can be seen in Figs. 2.4 and 2.5a), in the H_2CO ($3_{0,3}$ - $2_{0,2}$) line.

Outflows

This work focuses primarily on longitudinal flows along filamentary structures. To ensure there was no contamination from any associated outflows we looked at the shock tracers available in the ALMAGAL survey. After a comparison of shock/outflow tracers SiO (5 - 4) and SO (6_5 - 5_4) it was evident that SO (6_5 - 5_4) presented the most outflow signatures, manifested as blue- and red-shifted line wing emission ("wing" structures on 0th-moment maps, inspected visually, seen in Fig. 2.4) (e.g, Widmann et al. 2016; van Gelder et al. 2021). It must be noted that these are not definite detections, just indications of outflows, and this decision was made by visually inspecting the data and results for both lines. We investigated the presence of any red and blue shifted SO (6_5 - 5_4) emission, before continuing with our analysis. Figure 2.4 shows an example of such an analysis, and we can see signatures of a bipolar outflow from the central core in source AG348.5792-0.9197 (denoted by a green star in the figure). We see red-shifted emission extending to the west and blue-shifted emission to the east, both almost perpendicular to the filamentary structure. With such an analysis, we can focus on the filamentary structures and calculate flow rates along this axis without major outflow contamination.

Position-Velocity diagrams

Of all the strong lines available to use in the ALMAGAL spectral setup we decided to cut along the visibly elongated filamentary-like structures in the PV space using H_2CO ($3_{0,3}$ - $2_{0,2}$) due to its intermediate critical density ($\sim 7 \times 10^5$ cm^{-3}, Shirley (2015)) that is similar to the densities we expect to trace in our regions. H_2CO ($3_{0,3}$ - $2_{0,2}$) is also a tracer of relatively cool gas ($E_u/k \sim 21\,\mathrm{K}$) and can be used in combination with another H_2CO line as a well-known temperature tracer ($\sim 100\,\mathrm{K}$; e.g., Shirley 2015; Mangum & Wootten 1993; van der Tak et al. 2007; Gieser et al. 2021; Izumi et al. 2024). Abundance may vary by an order of magnitude over the evolutionary stages (Gerner et al., 2014).

The angle at which the PV cut was taken was determined by the outflow signatures and the filamentary structures. To ensure as little contamination from the potential outflows, the cut was made perpendicular to any signatures where possible, whilst keeping the cut inline with the filamentary structure. This is shown in Fig. 2.5. Any cores that did not have suitable emission in the PV cuts were removed from the sample (8 regions, 21 cores).

2.3 Flow rates

After sample selection, core identification, and line analysis the final sample consists of 87 regions with 182 cores in total. Table 2.2 shows how this sample is split among the evolutionary stages.

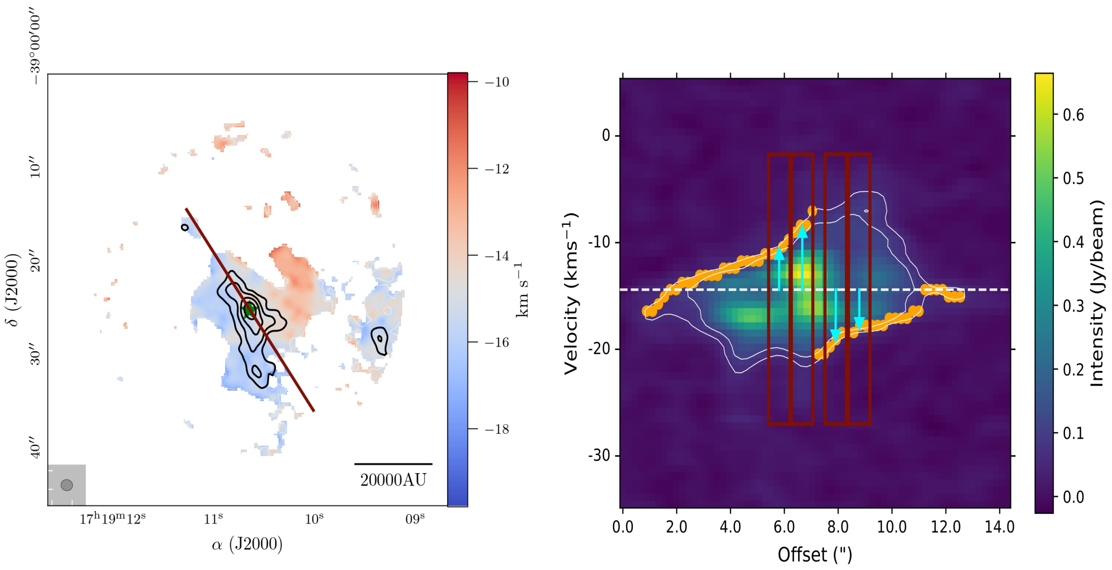

(a) 1st moment map.

(b) Position-Velocity cut.

Figure 2.5: **(a)** 1st moment map of YSO source AG348.5792-0.9197 in H_2CO ($3_{0,3}$ - $2_{0,2}$). The position of the continuum peak flux density is shown by the green star, and continuum contours are shown in black (levels 3,6,9 $\sigma_{\rm cont}$). The red line indicates the axis along which the PV cut was taken. **(b)** PV cut with 3 and 5 $\sigma_{\rm line}$ contours in white, and the $V_{\rm LSR}$ of the region shown by the white dashed line. The orange points show the nearest pixels at the 3 $\sigma_{\rm line}$ contours. The red boxes are examples of the areas where we estimate the flow rates across ($\sim 1''$). The peak flux density position of the continuum core is located at the center of each axis.

Table 2.2: Final sample distribution

Classification	Regions	Cores
Quiescent	17	28
Protostellar	23	48
YSO	22	51
HII region	25	55

2.3.1 Quantifying flow rates

To estimate the flow rates along the filamentary structures leading toward the cores, we follow the approach outlined in Beuther et al. (2020). The mass flows rates $\dot{M}$ are estimated as

$$\dot{M} = \Sigma \cdot \Delta v \cdot w, \tag{2.3.1}$$

where Σ is the surface density in units of $\rm g\,cm^{-2}$ (converted from the column density calculated in Sect. 2.3.2), Δv is the velocity difference from the velocity of rest to the 3 $\sigma_{\rm line}$ contour of the PV cut in $\rm km\,s^{-1}$, considered for the specific flow rate, and w is the width of the area along which the flow rate is measured in au. The final values of $\dot{M}$ are converted to $\rm M_\odot\,yr^{-1}$. In the following, we describe the parameter determinations in more detail along with details of the calculation (see Appendix A.2).

2.3.2 Column density

Column density maps were made using Equation 2.3.2 (modified black body emission equation from Schuller et al. 2009) assuming optically thin dust emission at mm wavelengths (Hildebrand, 1983),

$$N_{\mathrm{H_2}} = \frac{F_\nu R}{B_\nu(T_\mathrm{D})\Omega\kappa_\nu \mu m_\mathrm{H}}. \tag{2.3.2}$$

Here F_ν is the continuum flux density, $B_\nu(T_\mathrm{D})$ is the Planck function for a dust temperature T_D (see Sect. 2.3.3), Ω is the beam solid angle, μ is the mean molecular weight of the interstellar gas, assumed to be equal to 2.8, and m_H is the mass of a hydrogen atom. We also assumed a gas-to-dust mass ratio $R = 150$ (with the inclusion of heavy elements Draine (2011)), and $\kappa_\nu = 0.899\,\mathrm{cm^2\,g^{-1}}$ (interpolated to 1300 µm from Table 1, Col. 5 of Ossenkopf & Henning (1994)). This was used to compute the column density for each pixel from the continuum image. The column density maps will be used to select the specific positions where we compute the mass flow rates. In addition to the column densities, we also estimate the core masses following Equation 2.3.3 below,

$$M = \frac{d^2 F_\nu R}{B_\nu(T_\mathrm{D})\kappa_\nu}, \tag{2.3.3}$$

(e.g., Schuller et al. (2009)). Here we use the same values for κ_ν and the gas-to-dust ratio, and d is the distance to the source, F_ν is taken from the integrated flux density from the cores (leaves) from the `astrodendro` analysis. Details of how we use these values can be found in Sect. 2.4.4.

2.3.3 Temperature estimates

Different possibilities exist to estimate the temperatures needed for deriving the column density and mass. Individual estimates per core via molecular line emission of high-density tracers for the ALMAGAL sample will be presented in Jones et al. (in prep.). While one could use the dust temperatures derived from Hi-GAL (Molinari et al., 2010b), they have the disadvantage that they, in general, only sample the colder gas because of the *Herschel* far-infrared wavelength coverage and the large Herschel beam size. In a different approach, Molinari et al. (2016) and Traficante et al. (2023) calculated temperatures from spectral line emission, where they used luminosity to mass ratio (L/M) values as cut-off points for different temperatures. Following a similar approach, Coletta et al. (in prep.) have estimated temperatures that can be assigned to sources based on their evolutionary stage (indicated by

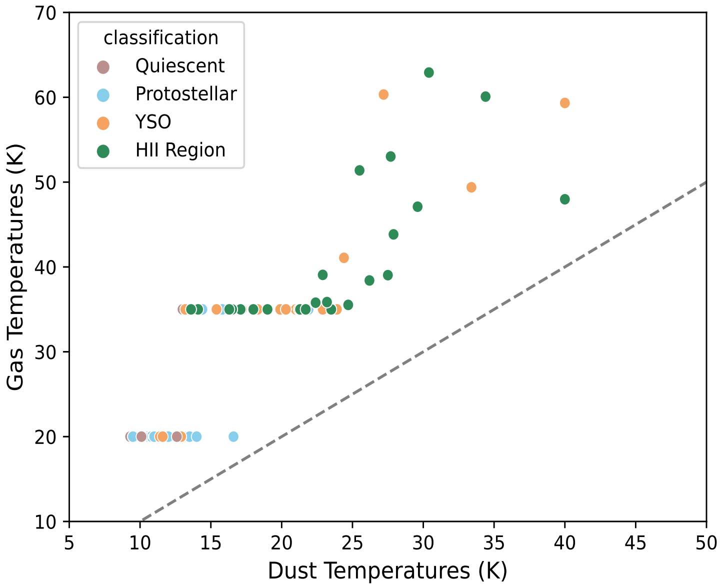

Figure 2.6: The *Herschel* derived dust temperature and the gas temperature plot against each other colour-coded in evolutionary stage. The grey dashed line shows the temperature equivalence line between the dust and the gas temperatures.

luminosity to mass ratio):

$$T(L/M) = \begin{cases} 20\ \mathrm{K} & \text{if} \quad L/M < 1, \\ 35\ \mathrm{K} & \text{if} \quad 1 \leq L/M < 10, \\ \max(21.1 L/M^{0.22}, 35\ \mathrm{K}) & \text{if} \quad L/M > 10. \end{cases}$$

Figure 2.6 shows the temperatures derived via these two approaches plotted against each other for each region. The gas temperatures show, as expected from Fig. 2.2b, that quiescent and protostellar sources have temperatures of 20 K, while at 35 K and above we see mostly YSOs and HII Regions, with some exceptions. Comparing this with the dust temperatures where there are some YSO and HII region sources with dust temperature values below 15 K leads us to investigate further how this selection would affect the end result. The calculation of the flow rates was therefore done with both the Hi-GAL dust temperatures and the gas temperatures. Comparing the results there were no qualitative and only small quantitative differences ($\sim$ 5-10 %) so we are confident to proceed with the gas temperatures with the reasoning that the dust temperatures are tracing primarily cold gas, whereas the gas temperatures take the warmer protostellar cores into consideration, which aligns more with our aims.

2.3.4 Width

The width parameter w, in Equation 2.3.1 is the width of the area along the filament we calculate the flow rate across. We take four areas along each PV cut to allow comparison between results at different offsets from the core. Two inner and two outer positions ($0.75''$ and $1.75''$ away on either side of the core) excluding the central most $0.5''$ (approximately half a beam size) to avoid contamination as this area is where the flows from all directions are merging. This width is taken as $1''$, the approximate beam size of the data, for all four areas toward each core. An example of this is shown in Fig. 2.5b with the red box showing the width we are looking at to be $1''$. With any conversion to linear distance, we have to take into account the range of distances to the sources in this work. Looking at our range of ~ 2 to 6 kpc (see Fig. 2.1), the more distant sources could have linear width parameters up to a factor three higher. Given that our widths are defined by the (approximate) beam width, at larger distances we capture a larger physical scale, and hence are more likely to have diffuse gas within our source area. This in turn results in more distant sources typically having a lower average column density. While these distance effects may be possible, our derived flow rates show no significant distance dependence, hence the effect should be small.

2.3.5 Velocity difference

To calculate a velocity difference we used the KeplerFit code from Bosco et al. (2019). The code works by dividing the PV cut into quadrants, taking the strongest (largest intensity) opposing quadrants and reading out the velocity values from the pixels that the specified σ_{line} contours go through (here we used 3 σ_{line}). These points are highlighted in orange in Fig. 2.5b. The velocity measurements are then taken as the difference between the velocity value from the central pixel along the contour confined to each red box in Fig. 2.5b, and the velocity of rest (white dashed line in Fig. 2.5b). In order to use the region's rest velocities as a proxy for the core velocities we compared the rest velocity values to the velocities measured toward the core peak positions in the H_2CO 1st moment maps. Comparing the difference between the two, we find that the majority of the values are less than our velocity resolution of $0.6\,\mathrm{km\,s^{-1}}$. In comparison to our median velocity difference measurement Δv of $3.4\,\mathrm{km\,s^{-1}}$, this is less than a 20 % error margin. Considering that the ALMA H_2CO emission is also affected by missing flux (see Sect. 2.3.6 for more information), especially near the peak velocities, this makes the rest velocity a good proxy for the reference velocity.

2.3.6 Error analysis

Data

Interferometric data without short spacing observations always suffer from missing flux. Regarding the continuum data, comparing to similar studies, e.g., the CORE project in the northern hemisphere with 20 regions was observed with a similar spectral setup and similar baseline ranges, Beuther et al. (2018) estimate 60 to 90%

missing flux across their range of sources. Regarding the spectral line emission, typically the extended emission around the rest velocity is more strongly affected than compact emission offset from the rest velocity. Therefore the lower-level contours (outlined in Figure 2.5b) needed for the PV analysis are not strongly affected. Hence, we are confident that the velocity structure from the H_2CO ($3_{0,3}$ - $2_{0,2}$) line is relatively well recovered. Missing flux has effects on our mass and column density estimates, so we take these values as lower limits.

Constants

For the gas-to-dust ratio, we use 150 (Draine, 2011). The mean molecular weight of the ISM μ, and the mass of a hydrogen atom m_H both have standard values that were used in our equations (Draine, 2003). The dust opacity, κ_ν was chosen for our conditions and suitable wavelength. For different densities and ice mantels the value could vary up to 30-40 %. Any uncertainties in these parameters here are considered minor compared to the systematic uncertainties discussed above and below, and we are confident that the overall trends we observe will remain consistent.

Error propagation

We consider five of our parameters used across this project to have significant uncertainties. These are the flux density, temperature, distance, width, and velocity difference. To calculate the effects this has on our overall results we use Gaussian error propagation for each equation that contains one or more of these parameters. To calculate a mean, standardised error for each flow rate we use mean values combined with the following errors; for the flux density we take 10 % from the calibration uncertainty, for temperature, we take 5 K, for the distance we assume a kinematic distance error of 0.5 kpc, for width we take $0.1''$ for on sky offset discrepancy and finally for the velocity differences we take the spectral resolution of $0.6\,\mathrm{km\,s^{-1}}$ as the error from the nearest pixel approximation. When combining these we end up with ± 50 % error margins on our final flow rates. For the core mass, we also estimate roughly ± 50 % error margins using flux density, temperature, and distance in the Gaussian error propagation.

Inclination angle

We set the inclination angle, i, to 0 for the filamentary structures in the plane of the sky. Our input parameters are all affected by the unknown inclination angles. Considering these, Equation 2.3.1 becomes Equation 2.3.4, below (full derivation can be found in Appendix A).

$$\dot{M}_\mathrm{obs} = \Sigma_\mathrm{obs} \cdot \Delta v_\mathrm{obs} \cdot w_\mathrm{obs} = \dot{M}_\mathrm{r} \tan(i) \tag{2.3.4}$$

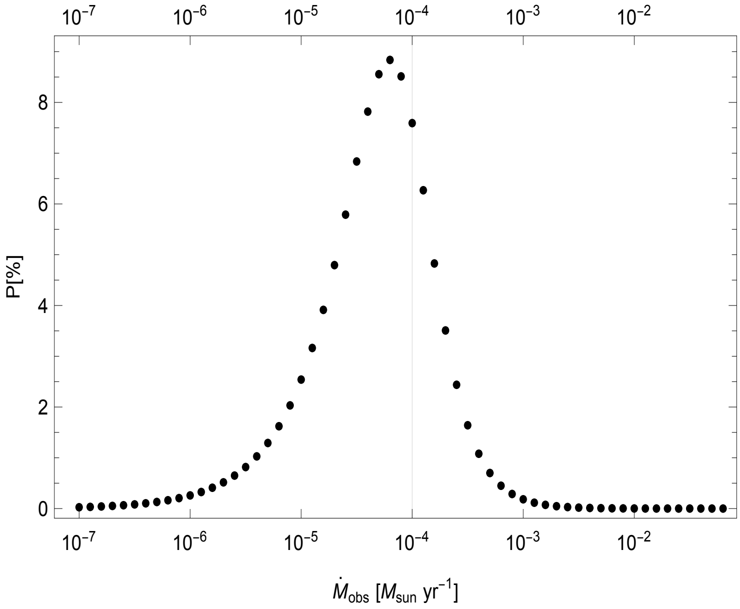

Figure 2.7: Theoretical spreading of the observed flow rate due to unknown inclination of the filament for a tube-like cylindrical filament model with a universal flow rate of $\dot{M} = 10^{-4}$ $\mathrm{M}_\odot$ yr^{-1} (marked as a vertical thin line). The probability distribution is generated for 60 bins with uniform binning width in log space.

Here we are left with a correction factor of $\frac{1}{\tan(i)}$. Hence, the inclination clearly affects the results, meaning our flow rate results have a more narrow distribution in reality as $\tan(i)$ will both increase and decrease with the inclination angle. In order to check for the potential spreading of the observed flow rates due to the unknown inclination angle between the filament direction and the observer's line-of-sight, we compute analytically the spreading for an idealised case: We assume a sample of an arbitrary number of filaments with an universal flow rate of $\dot{M} = 10^{-4}$ $\mathrm{M}_\odot$ yr^{-1} along all filamentary structures of the sample. We approximate the filaments as cylindrical tube-like structures with a constant and uniform flow rate, hereafter called the "real" flow rate $\dot{M}_{\mathrm{r}}$. The corresponding probability density of the observed flow rates is then given as

$$\rho_{\dot{M}_{\mathrm{obs}}}(\dot{M}_{\mathrm{obs}}) = \frac{1}{\dot{M}_{\mathrm{true}}}\left(1+\left(\frac{\dot{M}_{\mathrm{obs}}}{\dot{M}_{\mathrm{r}}}\right)^2\right)^{-1.5}. \tag{2.3.5}$$

We bin the flow rates in the range from 10^{-6} $\mathrm{M}_\odot$ yr^{-1} to 10^{-2} $\mathrm{M}_\odot$ yr^{-1} into 60 bins with uniform binning width in log space and compute the observational probability by numerically integrating the probability density over the bin. The final outcome is presented in Fig. 2.7.

The peak of the probability distribution is quite close to the true flow rate, especially compared to the overall uncertainties of the measurement of the observed flow rates. Also the spread is acceptable with a full width at half maximum of the distribution of quite exactly one order of magnitude in observed flow rate.

In reality, the longer slope toward smaller flow rates will be further reduced (i.e., will attain a lower probability to be observed) due to the fact that in the simple tube-like model the flow velocity is always aligned with the filament axis and an observer at inclination $i = 0$ is assumed to measure zero velocity; in reality, there will be a non-zero velocity in those directions, which in turn reduces the likelihood for observations of the smallest flow rates. Furthermore, a real sample of filaments will most likely deviate from the assumption of an universal flow rate through all filaments. This will yield an additional spreading of the distribution of observed flow rates, which is on purpose not taken into account in our analytical model, which analysis focuses on the effect of the unknown inclinations only.

2.4 Results

Following the initial analysis and methodology laid out in Sections 2.2.5 and 2.3 we present the results for our sample, which using the parameters discussed in Sect. 2.3 contains 728 measured flow rates. These are mainly constrained between 10^{-6} $\mathrm{M_\odot\,yr^{-1}}$ and 10^{-2} $\mathrm{M_\odot\,yr^{-1}}$, with the average values being on the order of 10^{-4} $\mathrm{M_\odot\,yr^{-1}}$, which is conducive to forming a high-mass star in a few hundred thousand years (e.g., McKee & Tan 2003; Beuther et al. 2007; Zinnecker & Yorke 2007; Tan et al. 2014; Motte et al. 2018). All flow rates can be found in Table A.2.

Our general assumption for the estimated flow rates is that they are directional toward the cores and hence they are accretion flows. This should certainly be valid for the earlier evolutionary stages: quiescent, protostellar, and YSO. However, that is less clear for the HII regions. If one has evolving HII regions, those could already be pushing the gas outwards. Hence, the HII flow rates are not necessarily accretion flows. An individual classification of each core is beyond the scope of this paper.

Table 2.3: p-values from the KS and Mann-Whitney U tests.

Combination	KS p-value	Mann-Whitney p-value
QP	0.0457	0.7810
QY	0.0004	0.5725
QH	0.0014	0.3593
PY	0.0406	0.8313
PH	0.1014	0.5501
YH	0.6553	0.7457

Notes. Combinations are coded with the first letter of the evolutionary stage involved: quiescent, Q; protostellar, P; YSO, Y and HII region, H. Row one denotes the quiescent protostellar combination, and so on.

2.4.1 Statistical testing

To determine the statistical relevance of the results we applied two different, well-known, significance tests, the Kolmogorov-Smirnov (KS) test and the Mann-Whitney U test (Chakravarti et al. 1967; McKnight & Najab 2010). Both tests are non-parametric, making them suitable for data that may not follow a normal distribution. The KS test focuses on the entire distribution function, while the Mann-Whitney U test looks at the ranks of observations. Both tests generate probability values (p-values), and the interpretation is based on comparing the p-value to a chosen significance level. Here we use 0.05, as used by Chakravarti et al. (1967). The null hypothesis for both tests is the assumption that the samples come from the same distribution (KS) or population (Mann-Whitney U). The KS test generates a p-value, indicating the probability of observing the observed or more extreme differences if the samples come from the same distribution. The Mann-Whitney U test generates a p-value, indicating the probability of observing the calculated U statistic or a more extreme value if the samples come from the same population.

If our p values from either test are greater than 0.05 then any difference between the distributions is sufficiently small as to be not significant. These results are discussed in sections 2.4.2, 2.4.3 and 2.4.4 below.

2.4.2 Evolutionary stage

Looking at our flow rates in the context of evolutionary stage may tell us about how the accretion process changes as a (proto)star evolves. This result is presented in Figure 2.8. The four panels show the distribution for each evolutionary stage from quiescent to the HII regions. Considering the ± 50 % errors, there is a trend between the means and medians of these sub-samples, most notably between Protostellar and YSO sources. In terms of outliers, we have a few that can be seen in Figure 2.8. Outliers on the lower end are present in the earlier stages: quiescent and protostellar, and on the higher end in the the more evolved sources. KS and Mann-Whitney tests were done for each combination of the four data sets, the p-value results can be seen in Table 2.3. Using a significance level of 5 %, any p-value above 0.05 tells us there is likely no statistical difference between the data sets. We see that quiescent sources in combination with any of the others are likely not from the same distribution using the KS test however the Mann-Whitney p-value suggests these are not statistically different. By eye, we see there is an increasing trend in the mean or median flow rate through the evolutionary stages. We also note the similarity between these histograms and the distribution in Fig. 2.7, looking at the theoretical spreading due to unknown inclination angle. This gives us an idea that the spread we see in these results is likely partly due to the unknown inclination angle for our observational data.

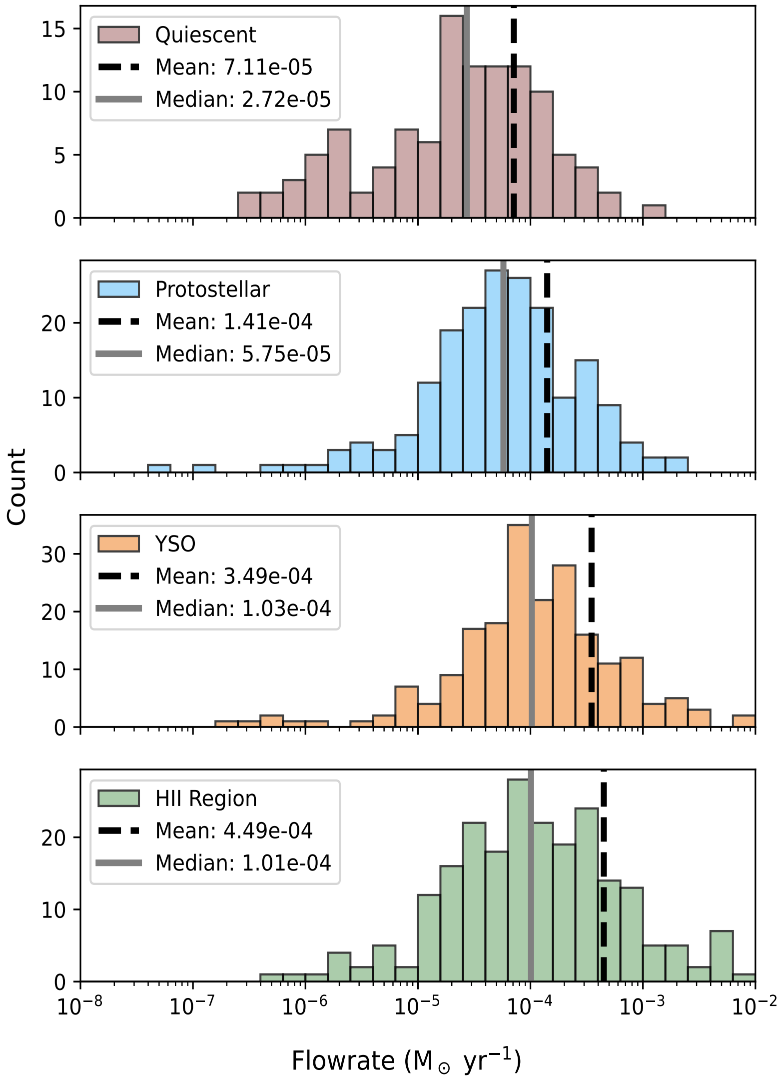

Figure 2.8: Histograms of the flow rate results for cores in each evolutionary stage quiescent to HII region from top to bottom. The mean and median are shown by the black dashed and grey solid lines, respectively, in each panel.

2.4.3 Offset from the core

We now discuss whether the flow rate changes with offset from the core. We look specifically at sections that are 1″in width at offsets from the central coordinates of 0.75 and 1.75″ away on either side of the core, along the filamentary axis. Figure 2.9 shows the distributions for the flow rates at 0.75″ (inner) and 1.75″ (outer) offsets. We see these two distributions have very similar median values but their means are qualitatively different by approximately a factor of two. Again, to determine if these two data sets have a significant difference KS and Mann-Whitney tests were performed (more information in Sect. 2.4.1). The p-values from the two tests were 0.0691 and 0.0731 respectively. Using our significance level of 0.05, we cannot reject the null hypothesis that these two distributions are from the same origin. As a further analysis, we looked at the difference between the inner and outer flow rates per core. The distribution can be seen in Fig. 2.10 where we can see the distribution centred around 0, with less than 0 meaning the core had higher flow rates further away along the filamentary structure and more than 0 meaning the core has higher flow rates closer to the centre of the core. With a median of 1.12×10^{-5} $\mathrm{M}_\odot\,\mathrm{yr}^{-1}$, we see a trend that the inner flow rates are larger than the outer ones.

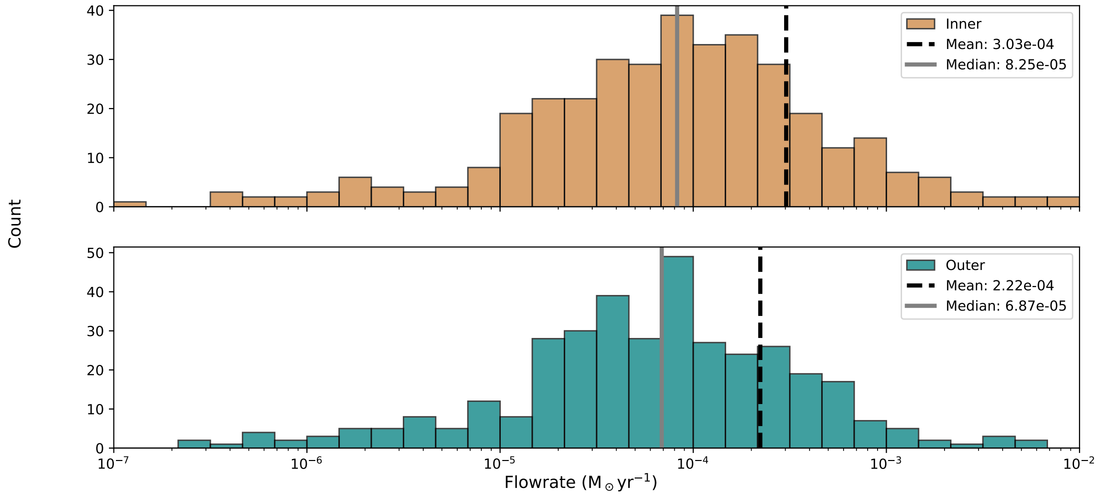

Figure 2.9: Histograms of the flow rate results in the context of offset from the core. The top panel shows the results from the inner regions and the bottom from those further from the core.

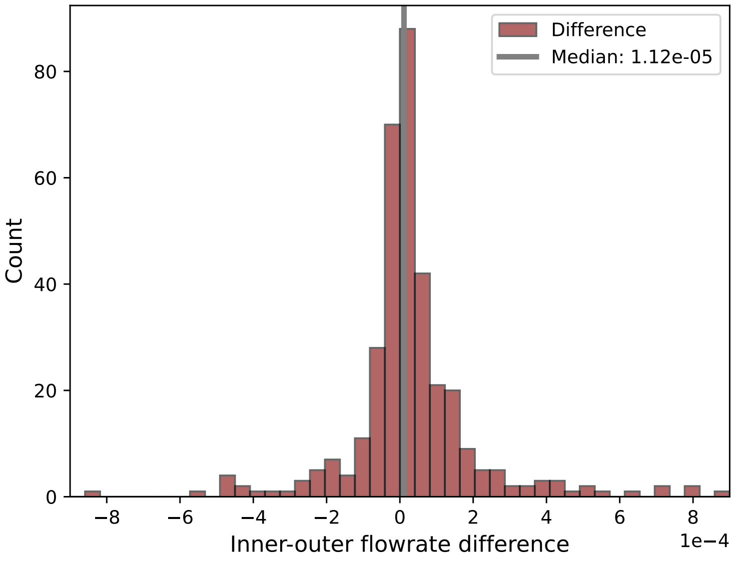

Figure 2.10: A histogram showing the distribution of the difference between the inner and outer flow rates per core ($\dot{M}_{\mathrm{inner}}$ - $\dot{M}_{\mathrm{outer}}$). The median of the distribution is shown as the grey line.

2.4.4 Core mass

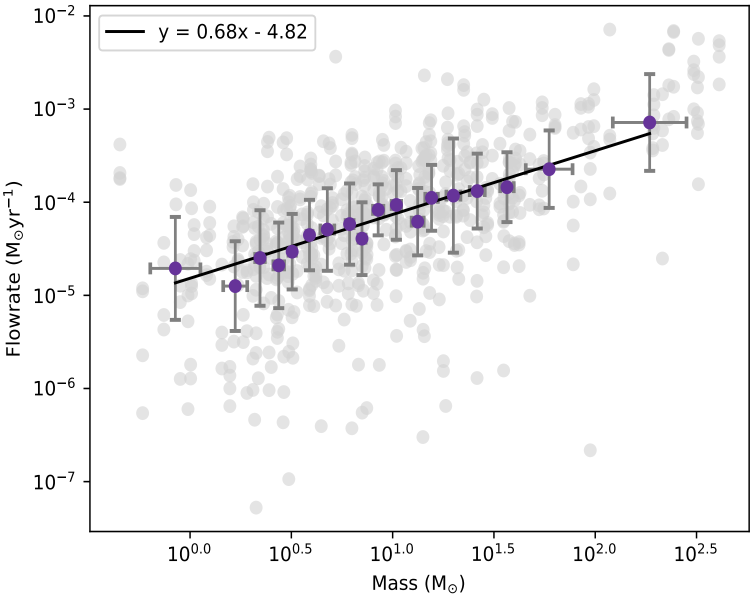

Figure 2.11: Scatter plot of the results of the whole sample showing flow rate vs. core mass in grey. The purple points are the average flow rate/mass values per bin, with the associated errors. Here, each bin contains the same number of cores. A line of best fit is shown in black.

Taking the integrated flux values for each core from the identification analysis (see Sect. 2.2.5) we calculated individual core masses, using Equation 2.3.3. The distribution of the flow rates vs. core mass is shown in Fig. 2.11 and we see a clear trend between the mass of these cores and the rate at which the material flows onto them. Overlaid in Fig. 2.11 in grey are the same points now binned, first per core (as there are four values per core), and then along the sample. Here we also have a line of best fit through these binned values. This suggests that we have a relationship where the flow rate follows $\sim$ $M^{2/3}$. We also looked to see if there was a relationship between these flow rates and the mass of the parental clump and we found no correlation. This indicates that flow rates are largely independent from the parental gas clump and that the found correlation is constrained to the smaller core scales.

As mentioned in Sect. 2.2.2 we looked into whether the sample had any bias' with respect to the whole ALMAGAL sample. Here we want to see if the distance spread, offset or evolutionary stage is causing any unexpected effects. We find no correlation between these flow rates and the distances of these clumps. For the offsets, the distance from the cores, we find that only taking into account the two flow rates closer to the cores gives a steeper relation than the one presented in Fig. 2.11 and if we look at just the flow rates further away from the cores we get a flatter relation. This is not surprising and is in support of Fig. 2.10 where we show that the inner flow rates are systematically larger than the outer ones. Comparative higher flow rates closer to the centre and a steeper relation with core mass are supportive that indeed gravity is dominating the infall dynamics. Figures with these relations shown can be found in Appendix A.1.

This is not the first time that a correlation between core mass and accretion rate has been found and or discussed in the literature. Beltrán & de Wit (2016) compiled YSOs with a range of masses and looked at the relationship between their mass and their accretion rates, getting an overall relationship proportional to $\sim \mathrm{M}^2$. During our analysis this relationship was looked at per evolutionary stage to see if in Fig. 2.11 we were seeing any of the evolutionary stages clumped together but this was not the case. We cannot comment on a specific relationship for our YSO values. Clark & Whitworth (2021) discuss what the resulting exponent in this relationship can mean in terms of different mass accretion mechanisms and also the star clusters system mass function. The two accretion mechanisms they discuss are tidal-lobe and Bondi-Hoyle (Bonnell et al., 2001). It is thought that tidal-lobe dominates when the potential of the cluster is still dominated by gas, this mechanism has an exponent of 2/3. The Bondi–Hoyle accretion mechanism dominates when the potential in the cluster is dominated by proto-systems, this mechanism has exponent 2. Our results are in clear agreement with the tidal-lobe accretion mechanism where the potential is dominated by the gas. This is consistent with the ALMAGAL sample covering early evolutionary stages.

2.5 Discussion

2.5.1 Comparison between low- and high-mass regions

In this section, we discuss how the flow rates estimated in this work compare to previous studies that quantitatively describe flow rates. The flow rates we present here are comparable to others in the literature for different mass ranges and scales,(e.g, López-Sepulcre et al. 2010; Duarte-Cabral et al. 2013; Kirk et al. 2013; Peretto et al. 2013; Henshaw et al. 2014; Traficante et al. 2017; Beuther et al. 2020; Sanhueza et al. 2021; Redaelli et al. 2022). Looking at an example from the low mass case, Kirk et al. (2013) uses their Mopra survey of multiple molecular emission lines to look for possible accretion flows onto the central cluster. They present values on the order of 2.8×10^{-5} $\mathrm{M}_\odot\,\mathrm{yr}^{-1}$. For an example of a high mass region, Henshaw et al. (2014) investigates the filamentary structure of an infrared dark cloud G035.39-00.33 in $\mathrm{N_2H^+}$ and finds mass accretion rates of 7×10^{-5} $\mathrm{M}_\odot\,\mathrm{yr}^{-1}$ with individual filaments feeding individual cores. An example with varying distances from the core is shown in Beuther et al. (2020), where they look at infrared dark cloud G28.3 using ^{13}CO and, depending on the distance from the core, they present values around 5×10^{-5} $\mathrm{M}_\odot\,\mathrm{yr}^{-1}$. If we zoom out and look at larger clumps, Traficante et al. (2017) report mass accretion rates between 0.04×10^{-3} and 2×10^{-3} $\mathrm{M}_\odot\,\mathrm{yr}^{-1}$. They also report seeing an apparent increase in the accretion rate depending on the presence of embedded 24 µm sources. This correlates to seeing a difference between our less evolved protostellar sources and more evolved YSO sources.

The results presented here are consistent with the results from the works in the literature mentioned above. The work done by Kirk et al. (2013) in the Serpens South region results are between a factor of 10 and 1000 times smaller than the results we present. If we think about the relationship between flow rate and core mass shown in Sect. 2.4.4 this is to be expected. Furthermore, comparing low to high-mass star formation, actual accretion rates in the high-mass regime tend to be much higher. There are many competing models discussing the formation timescale of high mass stars (e.g., Bonnell et al. 1998, 2001; McKee & Tan 2003; Beuther et al. 2007; Bonnell et al. 2007; Hartmann et al. 2012; Tan et al. 2014; Motte et al. 2018) giving approximately 10^5–10^6 yr. This then explains that our protostellar and YSO sources, similar to the one studied in Henshaw et al. (2014), exhibit very similar results.

2.5.2 Comparison to simulations

Observational studies and theoretical models are extremely complementary to each other for advancing our knowledge in many topics. Here we compare our results to theoretical models that have quantitatively produced accretion flow rates, looking specifically at the work done by Padoan et al. (2020a) and Gómez & Vázquez-Semadeni (2014).

Looking at the simulations by Padoan et al. (2020a), they produce a sample of roughly 1,500 stars within a volume of 250 pc and study the physical conditions surrounding the sample. The range of this simulation provides a large statistical sample of massive stars, forming realistic distributions of initial conditions. They present mean mass accretion rates on the order of $\sim 10^{-5}\ \mathrm{M_{\odot}\,yr^{-1}}$ onto the core and they also look at the mass accretion rate 1 pc away from the core and find it increases by an order of magnitude, which agrees with Traficante et al. (2017) on their values for larger scale accretion rates. They also state that their largest values are nearly 10 times higher than these mean values. The range of results we get from our sample agrees with the orders of magnitude discussed in their work. They go on to discuss whether the accretion rate grows systematically with time. We agree with their interpretation that this is not systematic (in their case at the ends of the prestellar phase, in our case throughout our evolutionary sequence).

Turning to Gómez & Vázquez-Semadeni (2014), they simulate the formation of a molecular cloud from converging gas flows resulting in a dynamic cloud with a lot of substructures, and the cloud grows due to accretion through filamentary structures channelling gas onto the clumps. They look at accretion rates radially along the filament and see a dependence that correlates to changes in the column density profile along the filament. Whilst the method produces filamentary structures the difference in scale makes it hard for a complete interpretation and comparison. Taking into account our work and the examples in this discussion there are definite similarities. The discussion of perpendicular versus parallel flows looking at accretion onto the filament itself and then along towards the central clump is also something discussed by many of these works. In the Gómez & Vázquez-Semadeni (2014) study, they looked at flows both along the filament and perpendicular and even compared themselves to the perpendicular results in Kirk et al. (2013) stating similar values, however also pointing out that their scales are slightly different.

2.6 Conclusions

This work aims to answer the question: what are the properties of accretion flows in high-mass star-forming clusters? This paper presents a subset of the regions from the ALMAGAL survey chosen to investigate the properties of flow rates, focusing specifically on longitudinal flows along filamentary structures towards the central core. A summary of the main results is as follows:

- Using calculated column density values and derived velocity differences using the H_2CO ($3_{0,3}$ - $2_{0,2}$) we were able to estimate flow rates for 182 cores from 87 regions of the ALMAGAL survey. We get flow rates on average on the order of $\sim 10^{-4}$ $M_\odot\,yr^{-1}$ with error margins of ± 50 %.

- We see trends of increasing flow rates through the evolutionary stages, and along the filamentary structure, increasing as we get closer to the central cores.

- We also see a relationship between the flow rates and the masses of these cores of $\sim M^{2/3}$, which supports the tidal-lobe accretion mechanism.

- Our results are in line with other observational studies and complementary to theoretical studies in the literature using different methods and mass ranges. Specifically, from the examples discussed, our flow rates are consistent with Padoan et al. (2020b), but we couldn't directly compare to Gómez & Vázquez-Semadeni (2014).

In addition to the conclusions drawn from this project, it is worth noting several supplementary contributions including evolutionary classifications being assigned to the whole ALMAGAL sample to allow for analysis in the context of evolutionary stage, and outflow signatures being detected in this ALMAGAL sub-sample using the SO (6_5 - 5_4) spectral line; looking at the "wings" of the spectra. Building on the trends we have seen in this work, important next steps would be to see what these relationships look like at both smaller and larger scales, and how these link to each other.

3

COMPARING THEORY AND OBSERVATION

M. R. A. Wells, *R. Pilsworth, H. Beuther, R. Pudritz, E. Koch.*

This following Chapter is based on the work ***From theory to observation: understanding filamentary flows in high-mass star-forming clusters*** which has been submitted to Astronomy&Astrophysics and is under review for publication.

I led this work under the supervision of Henrik Beuther and in close collaboration with all authors. Most scientific analysis was conducted by me, with R. Pillsworth contributing text to Sect. 3.2 and 3.6.1 and helping with the creation of Figures 3.1, 3.2, 3.12, 3.13, 3.14. All other text in the paper was written by me, and I created all remaining figures and tables. All co-authors provided comments and feedback for the paper.

ABSTRACT

Filamentary structures on parsec scales play a critical role in feeding star-forming regions, often acting as the main channels through which gas flows into dense clumps that foster star formation. Understanding the dynamics of these filaments is crucial for explaining the mechanisms of star formation across a range of environments.Here we use data from multi-scale galactic MHD simulations to observe filaments and star forming clumps on 10's of pc scales and investigate flow rate relationships along, and onto filaments as well as flows towards the clumps.Using the `FilFinderPPV` identification technique, we identify the prominent filamentary structures in each data cube. Each filament and its corresponding clump are analysed by calculating flow rates along each filament towards the clump, onto each filament from increasing distances, and radially around each clump. This analysis is conducted for two cubes, one feedback dominated region, and one with less feedback, as well as for five different inclinations (0, 20, 45, 70, and 90°) of one filament and clump system. Looking at the face-on inclination of the simulations (0°), we observe different trends depending on the environmental conditions (more or less feedback). The median flow rate in the region with more feedback is 8.86×10^{-5} M$_\odot$ yr^{-1} and we see that flow rates along the filaments toward the clumps generally decrease in these regions. In the region with less feedback we have a median flow rate of 2.92×10^{-4} M$_\odot$ yr^{-1} and when looking along the filaments here we see the values either increase or remain constant. We find that the flow rates from the environments onto the primary filaments are of an order of magnitude sufficient to sustain the flow rates along these filaments. When discussing the effects of galactic and filamentary inclination, we also observe that viewing the filaments from different galactic inclinations can reveal the presence of feeder structures (smaller filamentary structures aiding in the flow of material). Additionally, considering the inclination of the filaments themselves allows us to determine how much we are overestimating or underestimating the flow rates for those filaments. The different trends in the relationship between flow rate and distance along the filaments in both the feedback and non-feedback dominated cubes confirm that the environment is a significant factor in accretion flows and their relationship with filament parameters. The method used to estimate these flow rates, which has been previously applied to observational data, produced results consistent with those obtained from the simulations themselves, providing high confidence in the flow rate calculation method.

3.1 Introduction

Giant Molecular Clouds (GMCs) serve as essential structures within galaxies, acting as intermediaries (on the order of several tens of parsecs) that connect large-scale galactic dynamics to the smaller-scale localised star formation processes. The collapse and fragmentation of GMCs into dense regions capable of star formation is driven by a combination of gravitational instabilities and external pressures from the surrounding interstellar medium (e.g., Zinnecker 1984; Bonnell et al. 2003; André et al. 2014; Urquhart et al. 2018; Svoboda et al. 2019; Padoan et al. 2020b). As these clouds cool and accumulate mass, they fragment into smaller, denser regions under gravitational contraction. With extreme temperatures and pressures these smaller dense regions continue to collapse, forming clusters of protostellar objects.

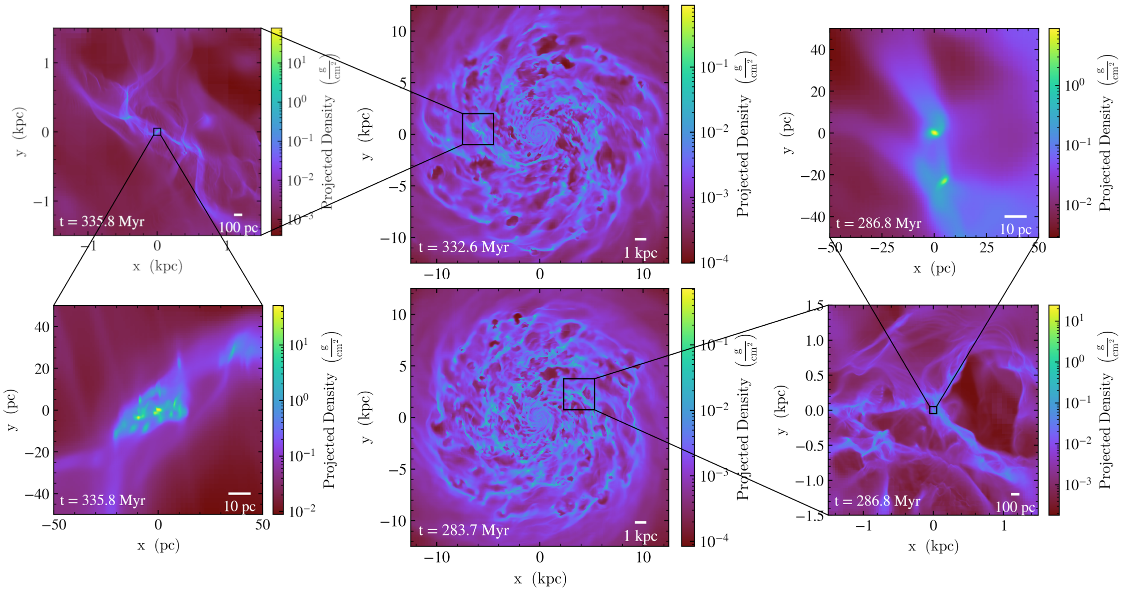

Figure 3.1: Galaxy overview from Zhao et al. (2024). The central panels show the two snapshots of the galaxy we are using, the top showing the location of the less feedback dominated region (quiet) and the bottom showing the location of the feedback-dominated region (active). The first zoom-in panels show the regions down to a few kpc (top left and bottom right panels), followed by the close ups of the regions in 100 x 100 pc boxes (bottom left and top right panels).

Intersections within these filamentary networks, known here as “hubs”, often serve as sites for the formation of high-mass stellar clusters, where the convergence of gas flows provide perfect conditions for the majority of stellar births (e.g, Lada & Lada 2003; Goldsmith et al. 2008; Myers 2009; André et al. 2010; Schneider et al. 2010; Bressert et al. 2010; Kirk et al. 2013; Krumholz 2014; Kumar et al. 2020; Grudić et al. 2021; Hacar et al. 2025). We see a self-similarity among the scales here too, where GMC’s are hub sites on larger scales too (e.g, Zhou et al. 2024). These filaments and filamentary-like structures have been a part of the discussion for years in different shapes and forms, looked at in different tracers, and as a part of many different studies both theoretically and observationally (e.g., Fiege & Pudritz 2000; Jackson et al. 2010; Kirk et al. 2013; Gómez & Vázquez-Semadeni 2014; Henshaw et al. 2014; Chira et al. 2018; Padoan et al. 2020b; Alves et al. 2020; Beuther et al. 2020; Schisano et al. 2020; Hacar et al. 2023; Pillsworth & Pudritz 2024; Wells et al. 2024). Evidence for the feeding of clouds, clumps and cores being done by filamentary structures can be seen in many of the studies mentioned above. These studies highlight how filaments, ranging in scale from galactic kpc scales down to sub-parsec levels, connect the parental molecular clouds, cluster forming hubs, clumps and individual cores, demonstrating the critical role they play in channelling mass and angular momentum. Despite the progress made in understanding filamentary structures and their role in star formation, several questions remain. The precise mechanisms by which material is transported through, along and around filamentary networks are still not well defined and their impact on the formation of high-mass star clusters are still not completely understood. Current simulations and observations continue to challenge our understanding of these processes, emphasising the need for further research to unravel the complexities of filament dynamics and their contributions to stellar cluster formation.

The advancement of theoretical model capabilities combined with large mm/sub-mm interferometers, such as the Atacama Large Millimeter/submillimeter Array (ALMA), the Northern Extended Millimeter Array (NOEMA) and the Submillimeter Array (SMA), has allowed in-depth research into more complex galactic structures such as filaments, on multiple scales. Observational (e.g., Ragan et al. 2014; Zucker et al. 2015; Russell et al. 2017; Hacar et al. 2018; Olivares et al. 2019) and computational (e.g., Gómez & Vázquez-Semadeni 2014; Federrath 2016; Haid et al. 2019; Li & Klein 2019; Padoan et al. 2020b; Zhao et al. 2024) studies are complementing each other, using observational constraints in models, or theoretical limitations in observational analysis which allow the field to progress further (e.g., Clark et al. 2014; Hillel & Soker 2020; Duan & Guo 2024). This collaborative approach is often underscored in reviews of the field, such as those by André et al. 2014; Pineda et al. 2023, which emphasise the importance of combining theoretical and observational perspectives. Together, these methodologies are advancing our understanding of the nature of filaments, allowing researchers to investigate their dynamics and trace their evolution in unprecedented detail.

In this paper, we use theoretical data cubes from the simulations by Zhao et al. (2024) at 5 different inclination angles (0, 20, 45, 70 and 90°, assuming face on is 0) and 2 different environments (more and less feedback) to measure flow rate properties along filaments, onto filaments and radially onto cluster forming clumps. Here we are investigating larger scale relations between flow rates and filamentary parameters, environment, and inclination. We also test the validity of observational methods to calculate flow rates on these theoretical data cubes by comparing calculated values with values from the simulation itself. The structure of the paper is as follows: the data is introduced in Sect. 3.2. In Sect. 3.3, we introduce `FilFinder`, the package used to identify filaments, and discuss the different parameters for our data cubes. Details of how perpendicular, parallel and polar flow rates in these regions are calculated are presented in Sect. 3.4, before showing the results in Sect. 3.5. Discussions happen in Sect. 3.6, including other scales and projects in the literature before we draw our conclusions and discuss opportunities for future work in Sect. 3.7.

3.2 Simulation data

We use data from multi-scale MHD simulations of a Milky Way type galaxy from Zhao et al. (2024). Those simulations were run in RAMSES with the AGORA project initial conditions (Kim et al., 2016). These include a dark matter halo with $\mathrm{M}_{\mathrm{DM\ halo}}$ = 1.074 x 10^{12} $\mathrm{M}_{\odot}$, $\mathrm{R}_{\mathrm{DM\ halo}}$ = 205.5 kpc, and a circular velocity of $\mathrm{v}_{\mathrm{c,DM\ halo}}$ = $150\,\mathrm{km\,s^{-1}}$, an exponential disk with $\mathrm{M}_{\mathrm{disk}}$ = 4.297 x 10^{10} $\mathrm{M}_{\odot}$, and a stellar bulge

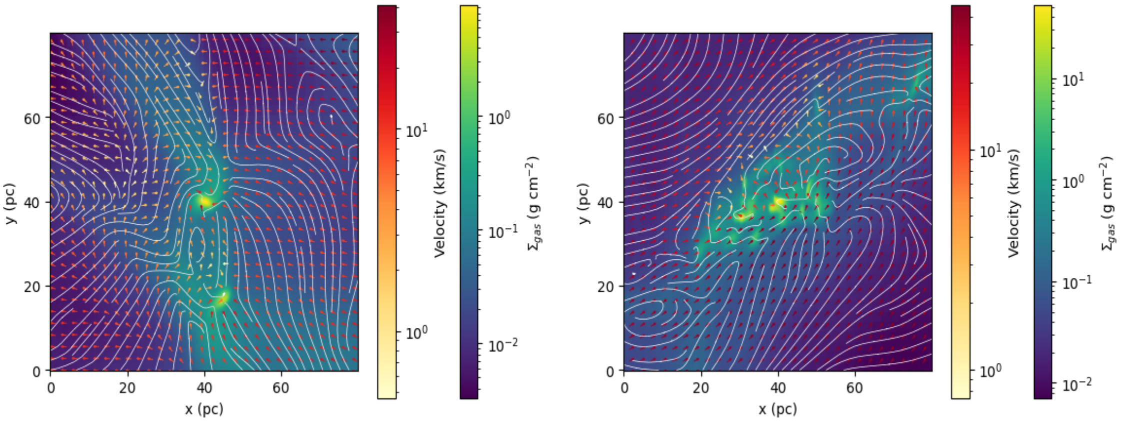

(a) Active region, taken at a snapshot of ≃ 283 Myr. **(b)** Quiet region, taken at a snapshot of ≃ 332 Myr.

Figure 3.2: Density projections of high-resolution zoom-in simulation data of Zhao et al. (2024). White streamlines represent magnetic field structure. Quivers show velocity direction and magnitude relative to the velocity of the central cores in each snapshot.

with $M_{\text{bulge}} = 4.297 \times 10^{10}\ M_\odot$ ((Kim et al., 2016)). For further simulation details we refer to Zhao et al. (2024); Kim et al. (2016).

Recently, Pillsworth et al. (2025) characterised the properties of over 500 galactic scale filaments in the Zhao et al. (2024) simulations using the Filfinder package (Koch & Rosolowsky, 2015). That work derived the mass distribution function and gravitational stability of filaments but did not investigate their flow dynamics.

This paper focuses specifically on the so-called active and quiet zoom-in regions within the galactic disk of Zhao et al. (2024). Figure 3.1 shows this galaxy in the central panels, with the two regions used in this work marked on top, and zoom panels shown either side. The active region (right panels) is dominated by feedback, in an area of converging super bubbles, whereas the quiet region (left panels) has less feedback and is in a spiral arm like area of the galaxy. These zoom-in regions are 3 kpc wide boxes around dense proto-clusters that achieve a spatial resolution of up to 0.28 pc. We extract data from 60 pc around the densest cell to focus on the star-forming cluster.

In Fig. 3.2 we show the two regions in projected density. Arrow quivers indicate the rotation-corrected velocity flow in the plane on projection, while streamlines track magnetic field structure. These figures outline the larger-scale gas flows. In panel (a), the feedback-dominated region, one sees that the gas flows onto the filamentary structures. This is caused by the feedback of the surrounding super bubbles. The velocities there have ordered gradients with clear increasing trends, direction pointing towards the central clump. In panel (b), the non-feedback region, on larger scales the velocities are almost parallel to the dense filament whereas on small scales the velocity field appears more chaotic leading to the many clumps. Looking at the magnetic field lines displayed in white we see they are more disordered in the region with less feedback (panel (b)), where as in panel (a), where we have more feedback, the lines follow parallel to the filament structure.

The extracted cubes are run through a position-position-velocity (PPV) post-processing code, using YT (Turk et al., 2011) and the YT astro analysis extension [1]. This step is key for the observational comparison as observations only produce PPV data cubes and not position-position-position (PPP). The cubes are 212 x 212 px at a resolution of 1 px = 0.285 pc with velocity channels at resolution of 0.8 $\mathrm{km\,s^{-1}}$. In terms of how this compares to resolutions we see in observation data, the velocity resolution is of a similar value to what was used in Wells et al. (2024). Spatially we have a likeness to larger scale single-dish data. Since we leave the galactic rotation to be corrected at a later point in the analysis, the bounds of the velocity channels change with inclination as the rotation of the galaxy becomes more dominant. For the face on (0°) cubes we have a velocity range of $-19.6\,\mathrm{km\,s^{-1}}$ to $19.6\,\mathrm{km\,s^{-1}}$. The PPV processing does not include any spectral line post-processing on the data, and instead returns column densities of the areas in $\mathrm{cm^{-2}}$.

3.3 Filament identification

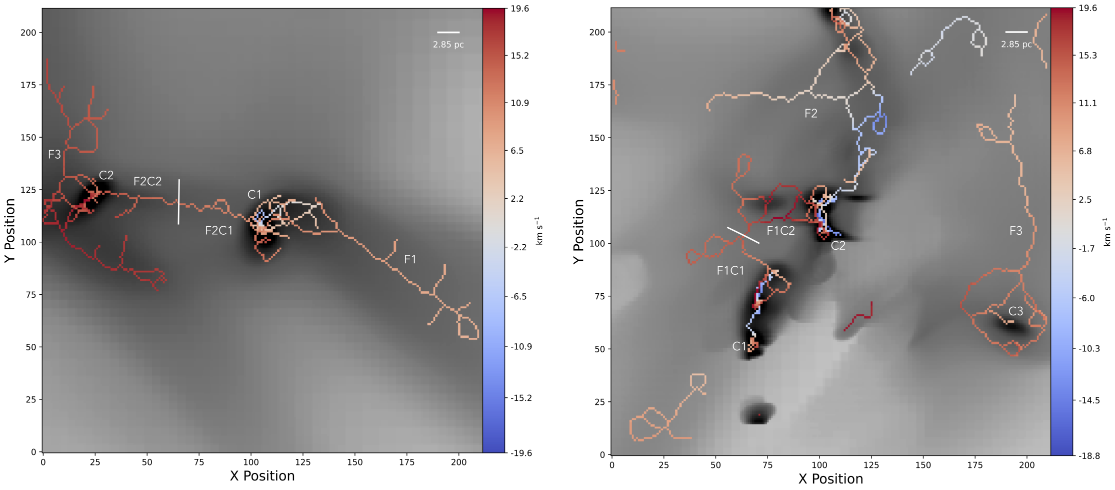

(a) Active (feedback-dominated) region

(b) Quiet (non feedback-dominated) region

Figure 3.3: 0th moment maps of the column density cubes with the identified filamentary structure, colour coded by velocity, overlaid on top. 2.85 pc scale bars are shown in the top right corners.

We identify filaments in the PPV cubes using `FilFinder` (Koch & Rosolowsky, 2015). Specifically, we make use of `FilFinder`'s new 3D identification technique (to be presented in E. Koch et al. in preparation), which is also used for 3D filament identification in Zucker et al. (2021) and Mullens et al. (2024). `FilFinder` in 3D uses similar morphological operations to the previous 2D version, namely using adaptive thresholding to identify locally bright structure over a large dynamic range. One

---

[1] Astro analysis code here: https://github.com/yt-project/yt_astro_analysis

Table 3.1: `FilFinderPPV` parameters

Cube	*adapt_thresh*	*glob_thresh*	pruning (px)
Active	13	0.0125	0
Quiet	21	0.0075	50

key change is `FilFinder`'s use of the `skan` package to improve efficiency to handle 3D skeletons structures (Nunez-Iglesias et al., 2018).

We use the following steps and parameters to define the filaments investigated in the subsequent analyses. First, we create a binary filament mask using a local threshold (`adapt_thresh`) and only keep structures above a minimum surface density (`glob_thresh`) with a minimum number of contiguous pixels (`min_size`) to minimise spurious isolated peaks. The resulting mask is skeletonised to produce the filament spines and structure for further analysis and pruning of spurious branches on the skeleton. Table 3.1 shows our choice of these key parameters for the different cubes we analyse. Lastly, we note that `FilFinder` is optimised to work on elongated, filamentary structures with aspect ratios of 3:1; the masking and pruning operations described above naturally removes compact and isolated structures, though we note that isolated compact structures without surrounding filamentary structures are not found in the simulated cubes we analyse. For our analysis, we define the location of the filament and its extent using the pruned skeletons produced by `FilFinder`.

3.4 Methods

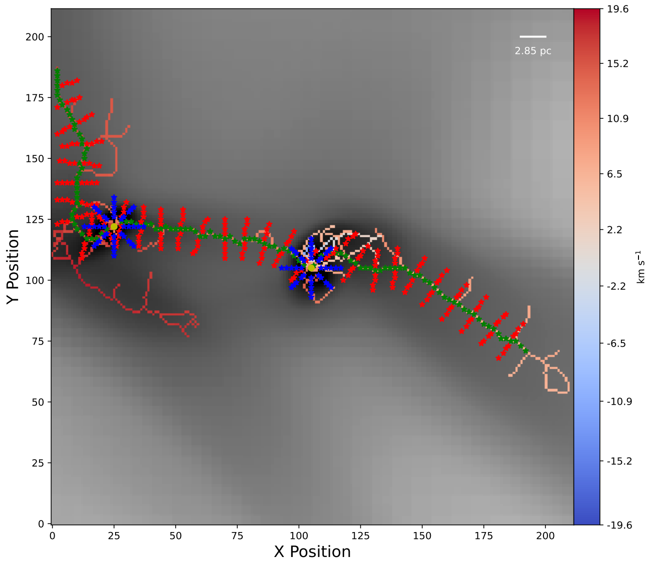

Figure 3.4: 0th moment map of the active column density cube with the identified filamentary structure, colour coded by velocity, overlaid on top. Green, red and blue points indicating the different types of flow rate, green is along the filamentary structure, red is onto, and blue is polar around the clumps. 2.85 pc scale bar in the top right corner.

To estimate the flow rates along and onto filamentary structures leading toward the clumps and radially around the clumps, we follow the approach outlined in Wells et al. (2024) based on Beuther et al. (2020). The mass flows rates $\dot{M}$ are estimated as

$$\dot{M} = \Sigma \cdot \Delta v \cdot w \cdot \frac{1}{\tan(i)} \tag{3.4.1}$$

where Σ is the surface density in units of g cm^{-2}, taken from the data cube directly, Δv is the velocity difference in km s^{-1}, calculated in different ways depending if its along, onto or polar (see Sect. 3.4.1). w is the width of the area along which the flow rate is measured in AU, we use two pixels (0.58 pc). The final values of $\dot{M}$ are converted to M$_\odot$ yr^{-1}. The correction factor of $\tan(i)^{-1}$ is for the unknown filament inclination, based on the discussion in Wells et al. (2024). Here, we do not apply that correction directly but we investigate inclination separately in Sect. 3.5.3.

3.4.1 Velocity difference

For this analysis we are investigating three different types of flow rates. The flow of material along filamentary structures, towards the central cluster forming clumps. The flow of material from the environment onto the filamentary structures, and radially around the cluster forming clumps. Each of these scenarios needs a slightly different method for calculating the velocity difference, these are outlined in the following sections.

Along

Moving along the filament we calculate the velocity gradient between each point on the filament spine and the "hub" where the filaments converge. These “hubs” are typically cluster-forming regions and we will refer to them as clumps throughout this work. In Fig. 3.4, the green points indicate the positions along the filament at which we calculate the flow rates. We use between 30-50 points per filament, at 0.58 pc (2 px) distance increments. We use the velocity value identified by `FilFinder` along the filament and calculate the difference between that value and the clump velocity which is estimated by fitting a Gaussian to the spectrum at the central pixel of the clump.

Onto

To calculate the flow rate onto the filaments, we take four positions on either side of the filament, (see the red points in Fig. 3.4), at 0.58 pc distance increments (2 px). Here the velocity difference is calculated in reference to the point where the perpendicular points meet the filament. For the perpendicular points we use the Gaussian fit to the spectrum method to get the velocity at the point, and the velocity on the filament is the same as above.

Polar

Clumps are fed by a number of filaments. We calculate the flow rates radially outwards from the core, along these converging filaments to include the contributions from each of the primary and feeder filaments (filamentary sub-structures). Here we define feeder filaments as smaller filamentary structures aiding in the flow of material either onto the primary filaments or onto the central star forming clump. These positions are marked by the blue points in Fig. 3.4, again at 0.58 pc distance increments. These points use the Gaussian fit to their spectrum for their velocity values and the difference is in relation to the core velocity, also calculated with this method.

3.4.2 Error analysis

Our flow rate equation consists of three parameters. Two are taken directly from the data cube itself, the column density and spatial resolution. The velocity values (`FilFinder` identified or Gaussian fitted) introduce the majority of the error to the final flow rate values. The velocity resolution in the cubes is 0.8 km s^{-1}, so we take an estimate for the `FilFinder` skeleton identification error to be one channel, 0.8 km s^{-1}. As for the Gaussian fitting, we take between $\sim$ 10 and 20 %, as the average error of the Gaussian fit. We conservatively assume an uncertainty of $\sim$ 20 % on the estimated flow rates. We note that in real observations the uncertainties are larger because additional systematic errors from the column density estimates and projection effects come into play. These values are without error bars in our analysis because they are taken directly from the simulations.

3.5 Results

Measuring the flow rates along and onto the filaments for both regions at 0 deg inclination as outlined in Sect. 3.4, Figs. 3.5 and 3.6 present the corresponding flow rates histograms. The distribution on the left panel of each figure is for flow rates along the filaments, while the distribution on the right corresponds to flow rates onto the filaments.

In Fig. 3.5, we present flow rate distributions for flow rates along the filaments (left panel) and onto the filaments (right panel) in the active cube. These range between 10^{-8} M$_\odot$ yr^{-1} and 10^{-2} M$_\odot$ yr^{-1} with median values of 8.85×10^{-5} M$_\odot$ yr^{-1} along and 1.95×10^{-5} M$_\odot$ yr^{-1} onto. We also see that the active distributions have similar mean and median values within our reported errors (see Sect. 3.4.2). In Fig. 3.6, we see the same but for the quiet cube. Here, the range of flow rates is between 10^{-7} M$_\odot$ yr^{-1} and 10^{-1} M$_\odot$ yr^{-1}, with median values of 2.92×10^{-4} M$_\odot$ yr^{-1} along and 2.31×10^{-5} M$_\odot$ yr^{-1} onto. This figure also shows that the quiet region has a significant difference between the distribution for along and onto the filaments, with their medians being separated by a whole order of magnitude.

The distribution for the flow rates onto the filaments is wider for both the active and the quiet cubes. These values range from being right next to the filament to $\sim 2.5\,\mathrm{pc}$ away, so there is likely to be a large variation. We would like to note that the flow rates onto the filaments are estimated only a selected cuts across them, but that ultimately gas flows onto the filament everywhere. Therefore, the flow rates onto the filaments have to be considered as lower limits. Having only an order of magnitude difference in these individual cuts, we conclude that the flows onto are more than enough to be "feeding" the flows along the filament and towards the central clumps.

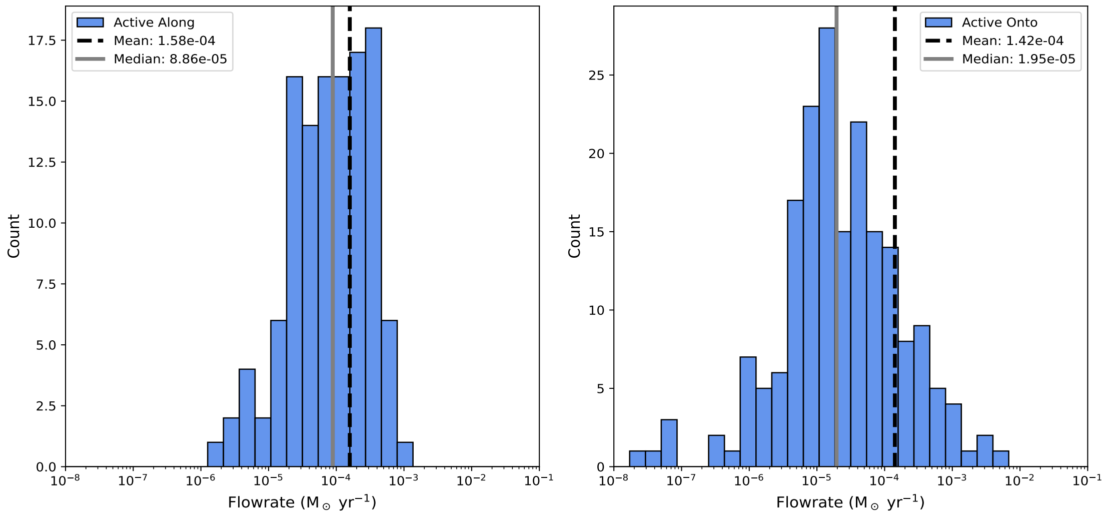

Figure 3.5: Distributions of flow rates *Left:* along filaments *Right:* onto the filaments in the active cube.

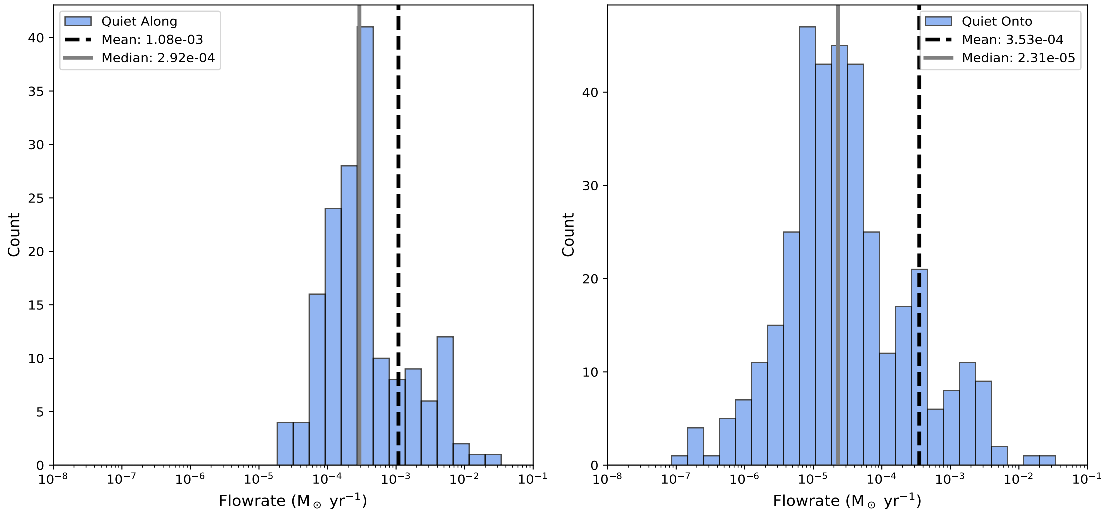

Figure 3.6: Distributions of flow rates *Left:* along filaments *Right:* onto the filaments in the quiet cube.

3.5.1 Along

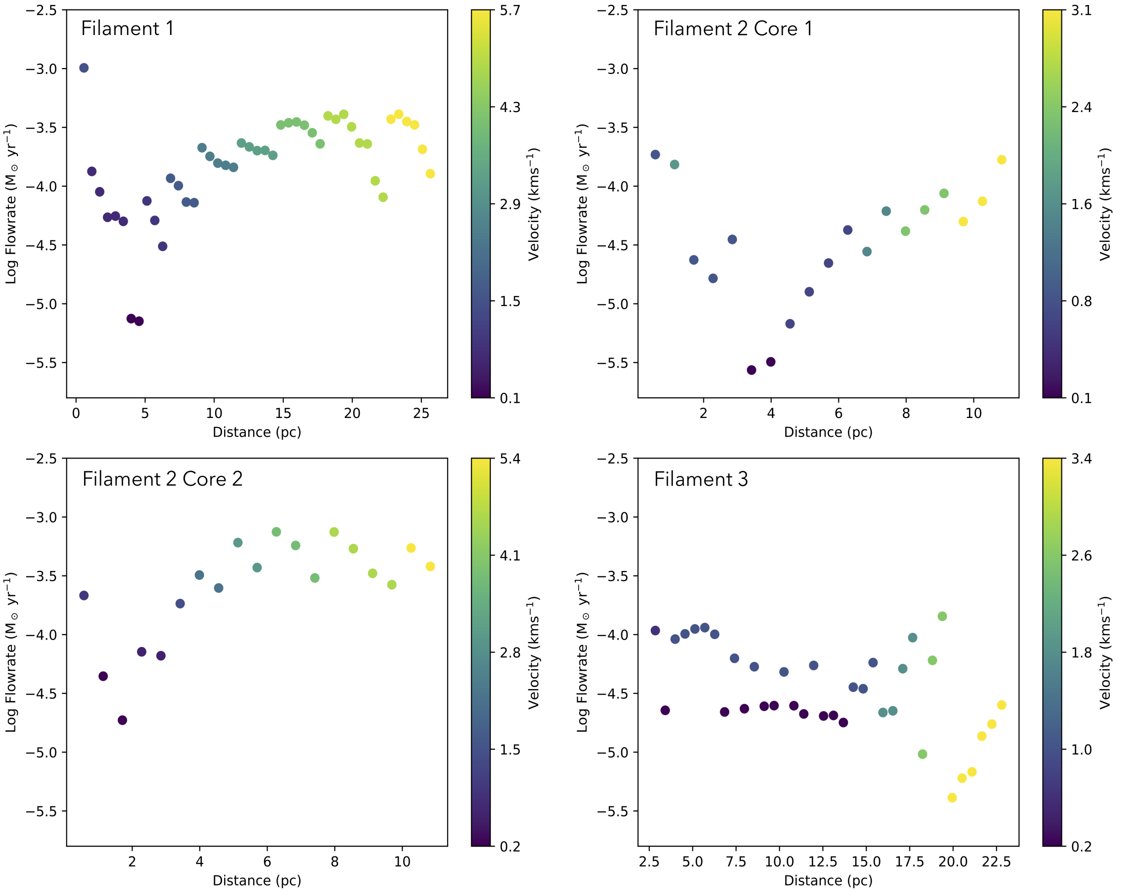

Figure 3.7: Distance vs flow rate, in log space, relationship for each filament in the active cube (filaments are labelled in Fig. 3.3a), colour coded by velocity difference.

For flows along the filaments, we analysed four different filaments in each region, focusing on flows directed towards the clumps. In the active region (Fig. 3.7), the filaments exhibit a trend of increasing flow rates with distance from the clump. This is consistent with the idea that at large scales the material is feeding whole clusters and getting closer to the central clumps this feeding can split up into several separate flows, which has also been seen on smaller scales (e.g., Padoan et al. (2020b)).

In the quiet region (Fig. 3.8) however, we see different trends. In two instances we see flow rates decreasing as the distance to the clump increases (see top two panels in Fig. 3.8), and also a more constant relationship after initial peaks (potentially due to higher column density). Comparing the filament morphology in both regions reveals that these differences can be explained by the presence and distinct roles of feeder filaments alongside the main filaments analysed. In the active region, feeder filaments primarily occur at the clump end of the main filaments. Here, the main filament splits into feeders as it approaches the hub, channelling the large flow rates across multiple paths and thereby reducing the flow rates closer to the core on the main filament. In contrast, the quiet region shows a different pattern. Feeder

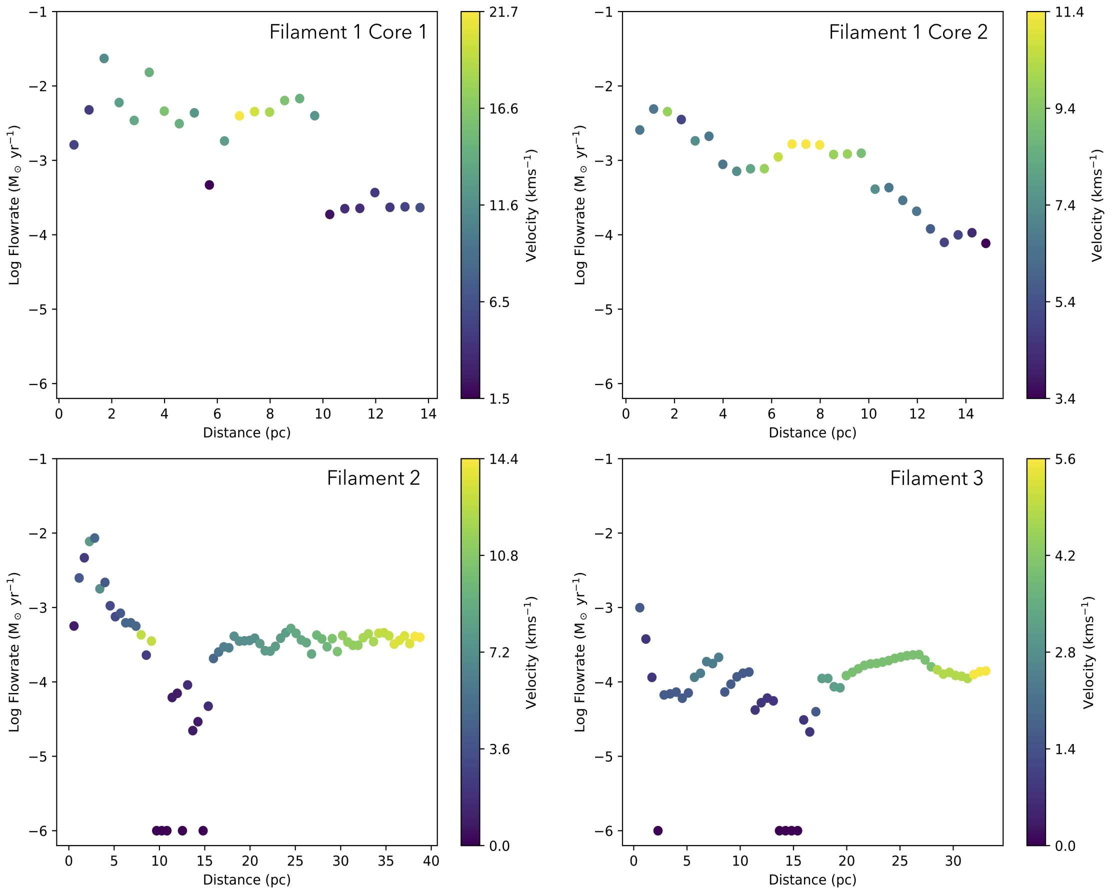

Figure 3.8: Distance vs flow rate, in log space, relationship for each filament in the quiet cube (filaments are labelled in Fig. 3.3b), colour coded by velocity difference.

filaments are not concentrated near the hub but are distributed along the length of the main filaments. These feeders merge into the main filaments at various points, resulting in higher flow rates reaching the central hubs.

This concept also accounts for the velocity peaks observed in the top panels of Fig. 3.8, which correspond to the locations where these feeders join the main filaments. In the bottom panels of Fig. 3.8 the trends start off with high flow rates close to the clump before evening out to constant flow rates with distance. This initial peak can be attributed to the column density contributions due to the extended area around the core where the column densities are higher.

3.5.2 Polar

By examining the flow rates radially around the central star-forming clumps we can identify the directions from which the largest contributions of material to the hub clump arise. Figures 3.9 and 3.10 show the flow rate values around each clump in both cubes. The red and blue lines overlaid show where the main filaments connect to the hub and where feeder filaments are. We see that there are far more feeder filaments around clumps in the active cube, and that their contribution is significant

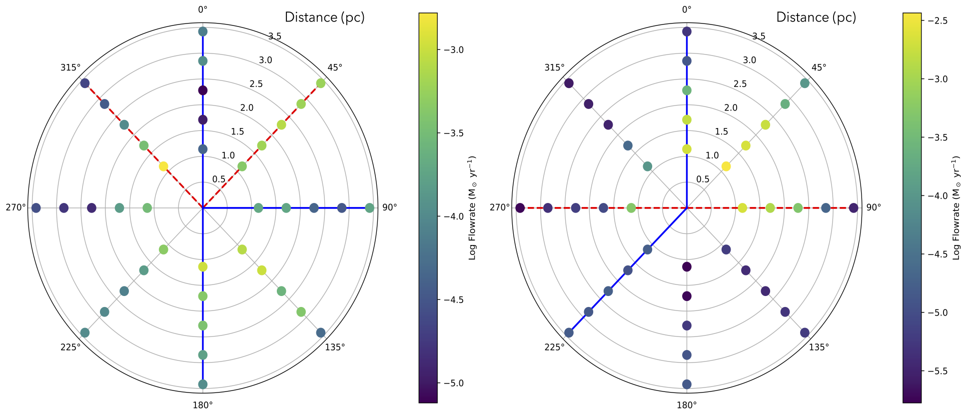

Figure 3.9: Radial distance - flow rate relationship for eight different angles around each clump in the active region. Numbers from 0.5 to 3.5 represent the distance from the centre for each of the concentric circles, in pc. Red dashed lines indicate the 'primary' filaments and blue solid lines indicate directions of the 'feeder' filaments.

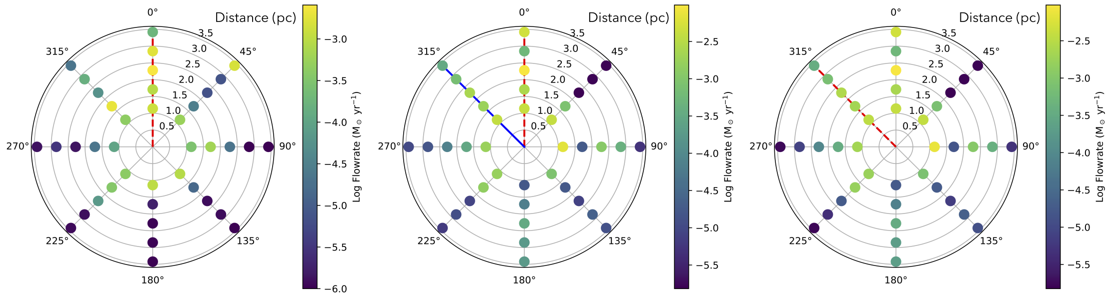

Figure 3.10: Radial distance - flow rate relationship for eight different angles around each clump in the quiet region. Numbers from 0.5 to 3.5 represent the distance from the centre for each of the concentric circles, in pc. Red dashed lines indicate the 'primary' filaments and blue solid lines indicate directions of the 'feeder' filaments.

to the flow of material onto the clump. The quiet cube, in contrast, has almost no contributions outside of its main filaments connecting to the clumps. In both Fig. 3.9 and Fig. 3.10 we see that from most angles around the clumps there is a gradient where the flow rate is increasing towards the centre which agrees with what we see in Figs. 3.7 and 3.8.

3.5.3 Galactic inclination

The inclination angle — both of the filament and galactic disc — directly influences the magnitude of the velocities measured in observations. Although the galactic disc inclination angle can typically be measured in external galaxies, inclination effects of filaments in the Milky Way are often poorly constrained. This uncertainty motivates us to take an in-depth look at the effects of Galactic and filament inclination on our estimated measurements of the flow rates along filamentary structures towards the central clump.

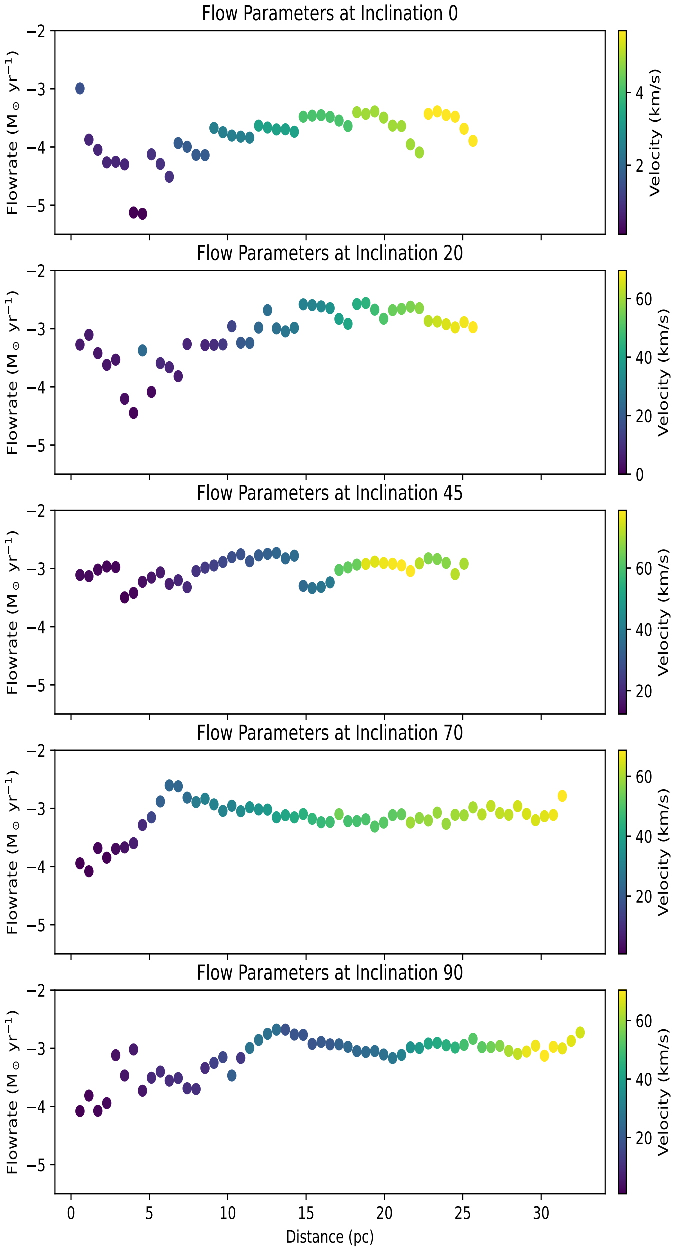

Figure 3.11: The effect of Galactic inclination on the distance vs. flow rate relationship, in log space, for filament 1 from the active region. Results are shown for five different Galactic inclinations, 0, 20, 45, 70, and 90°.

To pursue this goal, we take one filament and clump structure from the active region to focus on throughout the inclinations of 0 (face on), 20, 45, 70 and 90° (edge on). The results are shown in Fig 3.11. We see overall throughout the five inclinations the relationship between distance and flow rate varies by a factor 10. Looking at 0 and 20° we see initial peaks and then a small drop before steadily increasing by an order of magnitude, for 0° to $\sim 10^{-3.5}$ $\mathrm{M_\odot\,yr^{-1}}$ and for 20° to $\sim 10^{-2.5}$ $\mathrm{M_\odot\,yr^{-1}}$. At 45° the values are almost constant around 10^{-3} $\mathrm{M_\odot\,yr^{-1}}$. At the final two inclinations, 70 and 90°, we see the values start lower, at 10^{-4} $\mathrm{M_\odot\,yr^{-1}}$, than the previous inclinations before increasing, peaking around $10^{-2.5}$ $\mathrm{M_\odot\,yr^{-1}}$ and plateauing to become constant at larger distances from the clump, around 10^{-3} $\mathrm{M_\odot\,yr^{-1}}$. Flow rates onto the filament were also calculated at each inclination, the median values for each inclination are all on the order of 10^{-5} $\mathrm{M_\odot\,yr^{-1}}$, ranging between 1-7 $\times\,10^{-5}$ $\mathrm{M_\odot\,yr^{-1}}$ with a small increasing trend from 0 through to 90° inclination.

3.6 Discussion

These results provide us with several key insights on the effect that the environment plays in the morphology and kinematics of filaments and in particular upon the flow rate trends we measure. The largest flow rates, on the order of $\sim 10^{-1.5}$ $\mathrm{M_\odot\,yr^{-1}}$, are found along the filaments in the quiet (less feedback dominated) region (see Fig. 3.6). These are over an order of magnitude ($\sim 10^{-1.5}$ $\mathrm{M_\odot\,yr^{-1}}$ vs. $\sim 10^{-3}$ $\mathrm{M_\odot\,yr^{-1}}$) greater than the filamentary flow in filaments formed by the collision of super bubbles - characteristic of the active, feedback-dominated, region. This suggests that the spiral arms are more effective in funneling material than the active region.

This is supported upon examination of Fig. 3.2 which plots the column densities of filaments in the two regions. The column density values are, on average, higher in the spiral arm (quiescent) region, suggesting higher flow rates. Also, these higher column density regions are more spatially extended from the clumps in comparison to the active region where this intensity is concentrated on the clumps themselves. Both of these differences suggest that the dynamics of flows in spiral arms may play a more important role than stellar feedback in driving filament-aligned flow rates that feed gas into clumps and cluster-forming regions. Clearly many more such regions need to be examined before we can make firm conclusions - see Pillsworth et al. (2025). Several trends emerge from the measurements of the flow rates within both the active and quiet cubes. The active cube exhibits a clear pattern where flow rates increase with distance from the core, indicating that the flow dynamics are heavily influenced by the presence of feeder filaments near the hubs. These feeder filaments distribute the flow into multiple pathways, reducing the flow rate in the central regions of the main filaments. Conversely, in the quiet cube, flow rates are highest near the core and decrease with distance, suggesting a more centralised accumulation of material. The distribution of feeder filaments along the main filaments in the quiet cube contributes to this pattern, as these feeders progressively merge, allowing more material to reach the clump without significant distribution away from the central core. The order of magnitude difference in median flow rates also suggests a more dynamic process is taking place closer to the central clumps in the active cube, driven by the presence of multiple feeder filaments. In contrast, the higher median flow rate in the quiet cube indicates that even in regions of less feedback, a significant amount of material is still funnelled towards central clumps.

3.6.1 Comparison with 3D simulation values

A particularly interesting aspect of these observed measured flow rates for each filament is that we can directly compare them to their "true" values from the full, 3D simulation data. As such, we take an approximation of the filament in 3D by masking the (x,y) values contained in the skeleton and finding the peak density along the z-axis at each point. Within the region being explored, the peak density in z will represent the third dimension of the spine of the filament, assuming the spine is aligned with the dense ridge of the filament (as is done in filament profile fitters, such as RadFil in Zucker & Chen (2018)). We visually check for connectivity of this filament, ensuring that the z-values contribute to a continuous filament in 3D projections of the gas density. With an extracted 3D approximation of the filament, we project cartesian velocity fields onto the axis of the filament to measure the parallel components. The perpendicular vector is then the vector subtraction of the original velocity vector and the filament's parallel axis, and provides us with perpendicular components of the velocity field. The cross product of the two existing vectors contributes to the second perpendicular vector, allowing us to measure flows along four directions onto the filament. Flow rates onto the filament, perpendicular to its spine, are computed in 4 directions (0, $\pi/2$, π, $3\pi/2$). Each measurement is taken as the average flow rate from a vector extending 2.8 pc away from the spine of the filament. The flow rate of gas moving onto a single fluid element can be expressed with the density, velocity and the area being measured. For a single fluid cell, this is

$$\dot{m} = \rho \boldsymbol{v}_n A \tag{3.6.1}$$

where ρ is the volume density of gas moving through area A at a velocity normal to the surface $\boldsymbol{v}_n$. Measuring a flow rate, as opposed to tracking the change in mass over multiple timestamps, allows us to separate between parallel and perpendicular flow rates (i.e. along and onto the filament, respectively) while being able to neglect any changes that may be due to the changing morphology of the filamentary structure itself due to the dynamics in the larger galactic environment. With this approach, we measure the following flow rates on the two main filaments identified in the active cube that feed each clump. Figure 3.12 shows the flow rates measured along the spines of the filaments in the active region, corrected for the distance from the main core in the structure. The scatter points are coloured by velocity magnitude, similar to Figure 3.7, using the 3D vector. The top plot in Figure 3.12 represents Filament 1, which feeds the more massive clump. Flow rates along this filament average 3×10^{-4} $\mathrm{M_\odot\,yr^{-1}}$, but spreads to both higher and lower flow rates than the observational methods show. While the average flow rate agrees with the mean parallel flow rate in the active cube, the larger spread in the distribution of flow rates might suggest that lower values of flow rates are overestimated. The bottom plot in Figure 3.12 represents Filament 3, which feeds the smaller, less compact clump in the data. Flow rates along the filament show little spread, only 2 orders of magnitude,

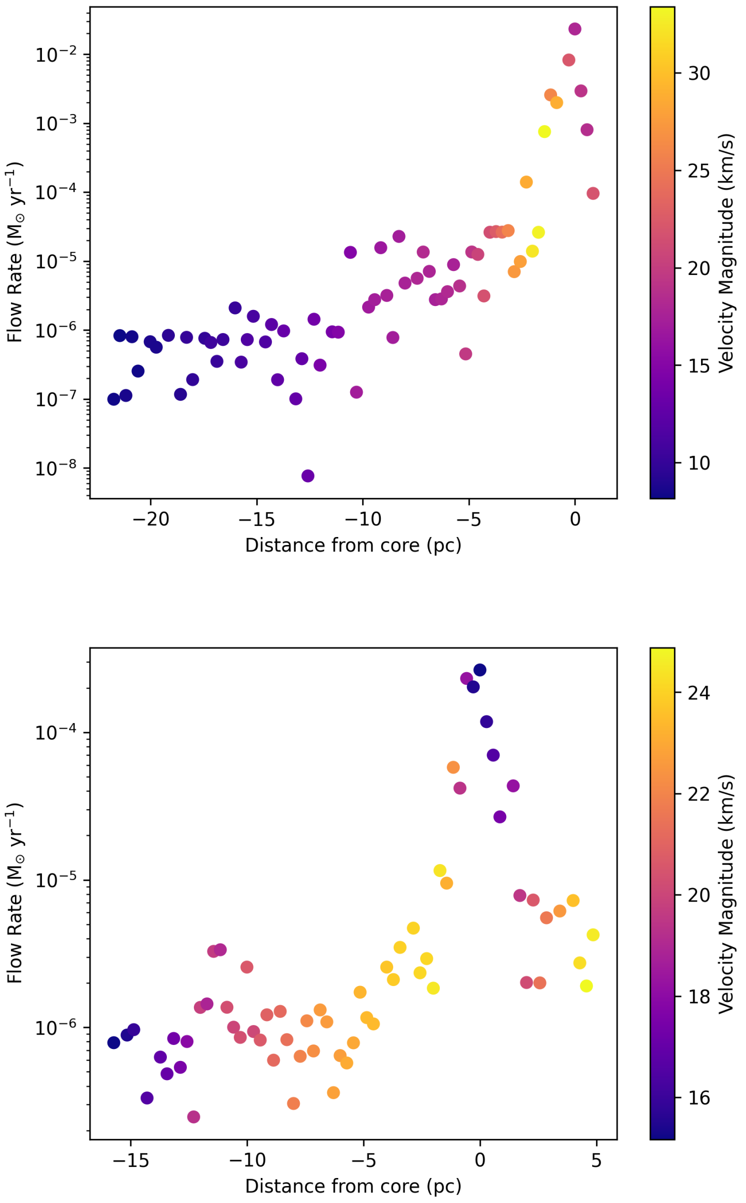

Figure 3.12: Flow rates along the filaments in the active cube, with colour bar representing the velocity magnitude at that point. *Top:* 3D filament corresponding to filament 1 in Figure 3.3a, feeding the central, massive clump. *Bottom:* the 3D filament representing Filament 3 in figure 3.3a, feeding the non-central clump. Negative values represent positions leftwards of the clump, i.e. lower values of x and y. On the x-axis 0 corresponds to the clump position.

and average to 1.5×10^{-5} $M_\odot\,yr^{-1}$. These averages agree with the median flow rate measured in our observational methods presented above. Figure 3.13 shows the distributions of the perpendicular flow rates for both of our 3D filaments in the active region. The left panel gives a median value of 3.73×10^{-5} $M_\odot\,yr^{-1}$ for Filament 1, the right panel gives a median value of 4.11×10^{-5} $M_\odot\,yr^{-1}$ for the Filament 3. Both values agree on order of magnitude with the observationally calculated distribution.

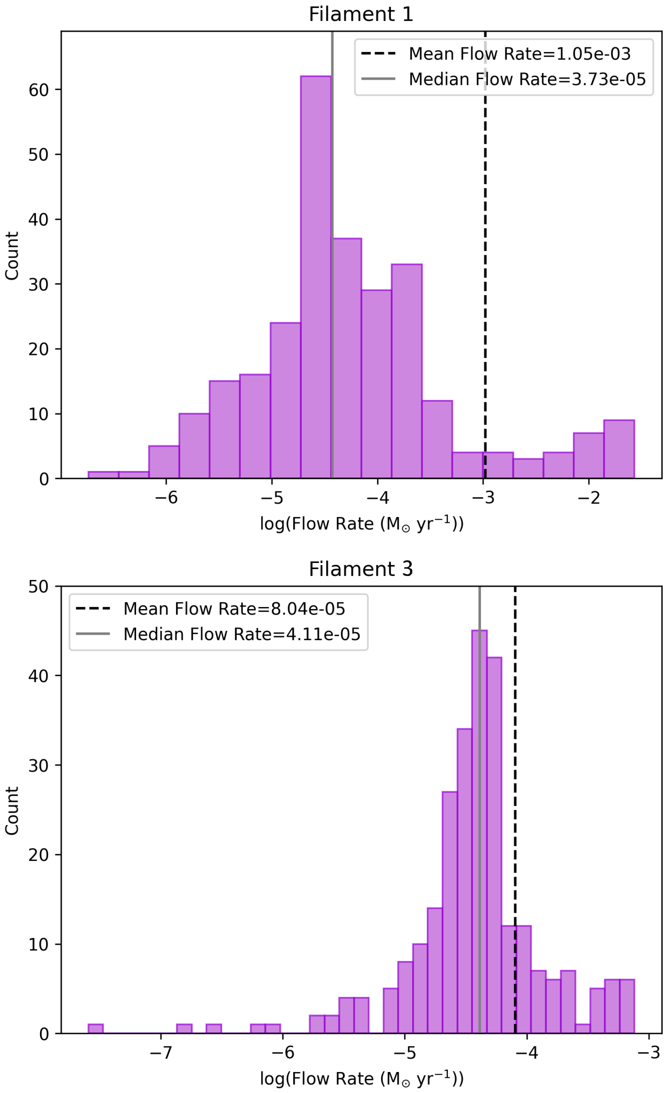

Figure 3.13: Distributions of all the perpendicular flow rates measured at 0, $\pi/2$, π, and $3\pi/2$ for the 3D filament spines in the active region. Black dashed and grey solid lines sit at the mean and median flow rate values, respectively, with numbers shown in the legend. *Left:* Filament 1, which feeds the central, massive clump. *Right:* Filament 3, which feeds the non-central clump.

We similarly conclude here that these values are enough to sustain the flow rates along each of these filaments.

Our simulation results for flow rate-distance relationships show the opposite relation to those measured in Padoan et al. (2020b), where the flow rates are increasing towards the core, while Padoan et al. (2020b) find that the flow rates decrease towards the core (their Fig. 17). We expect that this difference is primarily due to the different scales on which the flow rates are measured, as we explore the trends across $\sim 20\,\text{pc}$ scales while Padoan et al. (2020b) focus on the innermost $1\,\text{pc}$. For this part of the work we have focused on the filaments of the active, feedback-dominated region on scales of $\sim 20\,\text{pc}$. Our results may imply different flow behaviour in these larger scale regions than the small-scale turbulent box simulations from Padoan et al. (2020b). At $\sim$ 20 pc from the central clump, the gravitational force from it is unlikely to be the dominant effect on the velocity field, whereas the innermost 1 pc is situated within the gravitational potential of the forming cluster and the region's fields will naturally be affected by the dense clump's gravitational influence.

3.6.2 Filament inclination

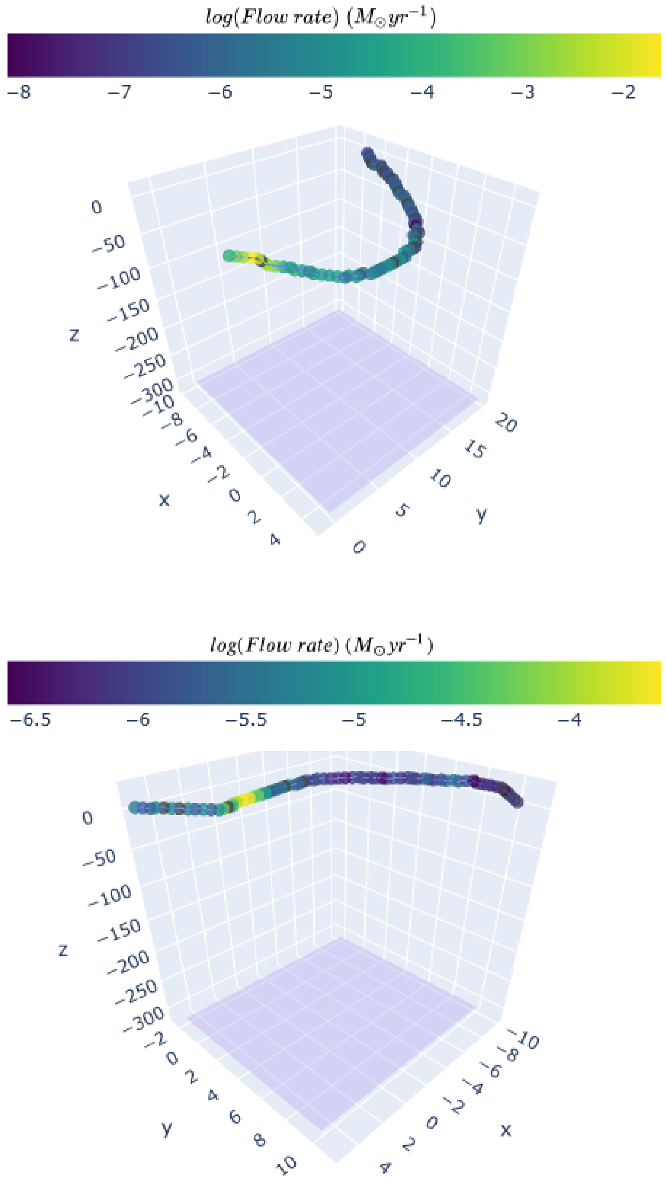

Figure 3.14: 3D projection of the filament spines for Filaments 1 (*top*) and 3 (*bottom*) in the active cube. Colour bar shows the parallel flow rate at that point in the spine, grey coloured markers depict points for which the direction vector of the spine was null. The light purple plane surface shows the position of the galaxy midplane. Interactive views of these filament spines can be viewed at `https://pillswor.github.io/research/`.

Filament inclination with respect to the galactic plane is more complicated. We can deduce that the filament is in the plane of the sky if there is no velocity gradient, but otherwise, the inclination angle is often treated as unknown in observational studies. For example, Wells et al. (2024) estimate the effects unknown inclination values have on the final flow values. They report that with unknown inclination angle they see a larger spread in the flow rate values, with the distribution peaking close to the "true" flow rate. However, with simulation data we can now obtain an estimate for an average inclination along the filament with respect to the galactic plane. We measure the angles of the filaments with respect to the galactic plane by sampling direction vectors along the 3D spines of the filaments. The angle between the two vectors is easily determined via their dot product. We measure the circular mean both unweighted and weighted by the parallel flow rate to calculate the average inclination for the entire filament. We calculate the weighted mean using the parallel flow rate, at each point along the spine as the weight. As such, the regions closer to the forming cluster with higher flow rates are weighted more heavily by the value of the inclination.

The results presented in Sect. 3.5.3 show the effects of galactic inclination where we incrementally increase the galactic inclination from 0° (face on) to 90° (edge on). We see that the range of velocity differences increases in the inclined cubes relative to the face-on cube. As a result, we see trends at all inclinations shown in Fig. 3.11 with typical flow rates of 10^{-3} $\mathrm{M_\odot\,yr^{-1}}$ to 10^{-4} $\mathrm{M_\odot\,yr^{-1}}$. Both the inclination and the presence of feeder filaments work together in this region to create different effects. The unknown inclination here will have similar effects on the feeder filaments as the primary filament. On the other hand, galactic inclination rotates the filament, with the potential to reveal other feeder filaments or more details about the structures that are not apparent from other angles.

In Figure 3.14, we present 3D plots of the filaments we have identified. Importantly, these show the position relative to the mid-plane of the galactic disk (shown by the light purple plane in the plot). This cluster-forming area sits 313 pc above the mid-plane of the galaxy, just within one scale height of the galaxy. For Filament 1, we measure an unweighted average of $|49.8|^\circ$ and a flow rate-weighted average of $|48.4|^\circ$. The two averages are consistent within error implying that the angle is similar along the entire filament. For Filament 3, we measure an unweighted average angle of $|10.9|^\circ$ and a flow rate-weighted average of $|0.8|^\circ$. From this, we deduce that the angle with respect to the plane is not consistent along the entire filament, with the highest flow rate areas closest to the clump tending to be more parallel to the plane. However, we note that both of these filaments are not coplanar with the galaxy midplane as they sit more than 300 pc above the mid-plane, as shown in Figure 3.14.

Taking into account the flow rate weighted average inclination angles we estimated from the simulation, we can compare the affect of the $1/\tan(i)$ inclination correction factor for on the the distribution of the flow rates for these two filaments.

For Filament 1, we find $1/\tan(i) \sim 0.8$, which means that our observed flow rates for this filament are slightly overestimated when inclination angle is unknown. For Filament 3, however, the inclination factor is $1/\tan(i) \sim 72$, meaning that our estimates are underestimated by over an order of magnitude. This is not surprising when looking at Fig. 3.7 we see the bottom right panel, Filament 3, has the lowest flow rates of the region. In general, it's important to consider unknown inclination angles when measuring and discussing observational flow rates, as they are a key factor in accurately interpreting the results and understanding the flow behaviour.

3.6.3 Comparison with observations

Whilst we have seen that using our observational method on the simulated data gives results that agree with the values derived directly from the models themselves, it is also important to see how the results compare with previous observational studies. Schneider et al. (2010) described the impact of filamentary structures on star formation with an in-depth study of the DR21 region, and show that flows onto the primary filaments can be enough to sustain them and their flow of material. For comparison to an observational study on similar scales to these simulations we turn to Beuther et al. (2020) where they look at the flow rates in the cloud surrounding IRDC G28.3 at distances up to $\sim 15\,\mathrm{pc}$, similar to some of the filaments we look at here. Their results are on the order of $10^{-5}\ \mathrm{M}_\odot\,\mathrm{yr}^{-1}$, appear constant over the extent of the cloud. Kumar et al. (2020) emphasised the role of hub-filament systems (HFSs) in star formation, concluding that hubs can trigger and drive longitudinal flows along the filaments in their systems, this fits in nicely with the idea of feeder filaments and the two roles we have detailed in this work.

Zhang et al. (2024) look at filamentary sub-structure on much smaller scales than ours; $\sim 0.17\,\mathrm{pc}$ long. They report flow rates, at the higher end of the range we see here, between $\sim 1.8 \times 10^{-4}\ \mathrm{M}_\odot\,\mathrm{yr}^{-1}$ and $\sim 1.2 \times 10^{-3}\ \mathrm{M}_\odot\,\mathrm{yr}^{-1}$. The different scales of their filaments is a key factor here for comparison with this work, which are around $20\,\mathrm{pc}$ in length. The authors also measure the flow rates within areas corresponding to the smallest scales covered by our simulations. Their values appear at the upper end of our distributions, and additional small scale effects, e.g., additional gravitational attraction, may increase their values.

These comparisons suggest that while broad trends and values are consistent across studies, the detailed morphology and arrangement of filaments are key factors in the flow dynamics of star-forming regions and it is of the upmost importance that we understand them. Future studies covering both larger and smaller spatial scales are needed to explore how these parameters vary with simulations and observations to shed further light on these issues.

3.7 Conclusions

Our analysis of the flow rates in different environmental conditions from a simulated Milky Way-type galaxy by Zhao et al. (2024) provides significant insights into the dynamics of filamentary structures in different star-forming environments. The use of `FilFinder` identification techniques allowed us to extract and analyse filaments, revealing differences in flow patterns between these regions. Overall we see flow rates on the order of 10^{-4} $\mathrm{M_\odot\,yr^{-1}}$ and 10^{-5} $\mathrm{M_\odot\,yr^{-1}}$ which are in good agreement with observations (e.g., Kirk et al. 2013; Henshaw et al. 2014; Beuther et al. 2020; Zhang et al. 2024; Wells et al. 2024). The key take away points from this work are as follows:

- Values for flow rates along individual cuts onto the filaments are lower than those along the filament, the cumulative flow rates summed from these individual cuts along the filaments is enough to sustain the flow rates we see along the filaments.

- In the active, feedback-dominated, region, flow rates tend to increase with distance from the core, a pattern explained by the presence of multiple feeder filaments distributing the flow into various paths onto the central clump.

- The quiet, more spiral arm like, region displays higher flow rates near the core, suggesting a more centralised accumulation of material. The progressive merging of feeder filaments into main filaments in these regions supports a sustained material flow towards the central clumps.

- Radially around the clumps we identify the primary filaments along with the presence or absence of feeder filaments. These filaments align with the directions of the largest contributions to the flow of material onto the clump.

- Feeder filaments play distinct roles depending on the environment. In regions with higher feedback, they channel material from the primary filaments to feed the clumps. In contrast, in environments with less feedback, feeder filaments directly supply material from the surroundings to the primary filaments themselves

- Taking the average filament inclination for two of the filaments in the active region we discuss how our values are slightly overestimated for filament 1, the filament feeding the more massive clump, and they are underestimated by a factor of ~ 72 for filament 3, feeding the smaller clump in the region.

- We see that our method for estimating the flow rates produce results inline with those directly from the simulation, with similar statistics and distributions, giving us confidence in the values we could obtain using this method on observational data.

Finally, our findings align numerically with observational studies, highlighting the critical role of filamentary structures in star formation. The differences in flow dynamics and filamentary structures underscore the importance of feeder filaments in shaping the star-forming environment. Future work should focus on refining simulations to match more observational scales and exploring the impact of inclination on observed flow rates.

4

HIERARCHICAL FLOWS FROM CLOUDS TO CORES.

M. R. A. Wells, *H. Beuther, S. Molinari, P. Schilke, C. Battersby, P. Ho, Á. Sánchez-Monge, B. Jones, R. Kuiper, D. Elia, A. Traficante, R. S. Klessen, Q. Zhang, S. Walch, M. T. Beltrán, Y. Tang, G. A. Fuller*

This following Chapter is based on the work ***Hierarchical Flows from Clouds to Cores. Characterising the Flow from pc to 1000 au Scales with ALMAGAL + IRAM 30m*** which is in preparation to be submitted to Astronomy&Astrophysics.

I am leading this work under the supervision of Henrik Beuther and in collaboration with the ALMAGAL consortium, all scientific analysis has been conducted by me. All text in the paper was written by me, and I have created all figures and tables. Select co-authors have given comments on this early draft, with the next draft being circulated to all co-authors shortly.

ABSTRACT

Linking accretion mechanisms through the different scales of high-mass star formation is crucial to understanding how these stars accumulate their material, from the large-scale collapse of molecular clouds down to the flow of material onto the forming protostar. In this work we use data from the ALMA Evolutionary Study of High Mass Protocluster Formation in the Galaxy (ALMAGAL) survey and IRAM 30m data. We selected 10 ALMAGAL regions covering four evolutionary stages from quiescent to protostellar, Young Stellar Objects (YSOs), and HII regions. We study these 10 regions at small ($\sim 0.6''$ resolution from ALMAGAL), intermediate ($\sim 1''$ resolution, from ALMAGAL) and large scale ($\sim 12''$ resolution, from the IRAM 30m). We identify large scale clumps and filaments visually and identify intermediate and small scale cores using the `astrodendro` package. Our primary analysis is centred on the $C^{18}O$ (2-1) and H_2CO ($3_{0,3}$ - $2_{0,2}$) lines which allow us to measure the velocity fields surrounding these cores. We calculate flow rates using column densities and velocity differences across a set width, at each spatial scale and evolutionary stage. On the large scale we present results for the relationship between flow rates and distance from the clump, in which we generally see a decreasing trend or very little variation. Looking radially around the clumps we see alignment between the highest flow rates and the direction of any associated filaments, and we also see gradients with increasing flow rates onto the clump. Comparison between the scales shows small variation when taking into account the associated errors (1.06×10^{-4} M$_\odot$ yr^{-1} at the large scale, 6.28×10^{-5} M$_\odot$ yr^{-1} at the intermediate scale, 4.40×10^{-5} M$_\odot$ yr^{-1} at the small scale). The same is seen of the relationship between flow rate and evolutionary stage at each spatial scale. Overall, we have three data sets for the same 10 regions that allow us to investigate flow rate relationships across three spatial scales. We present results for the large scale clumps and filaments, and compare the distribution of the large scale results to those from the intermediate and small scales. We see no statistically significant consistent trends though scales or evolutionary stage, but report small variations.

4.1 Introduction

Throughout the universe, formation processes happen on many scales. This is not any different for the formation of high-mass stars. Connecting physical structures across multiple scales is a fundamental challenge in studying high-mass star formation. While large-scale (pc-scale) molecular clouds provide the initial reservoir of material, the substructure within these clouds determines how mass is transported inward to form stellar systems. Observations have demonstrated that material flows along filaments on scales of several parsecs, funnelling mass into hubs or ridges, which then collapse into cores on scales of hundreds to thousands of au (e.g., Kirk et al. 2013; Henshaw et al. 2014; Alves et al. 2020; Beuther et al. 2020; Schisano et al. 2020; Syed et al. 2022; Hacar et al. 2023; Wells et al. 2024; Beuther et al. 2025). Whether this hierarchical process involves a continuity in accretion mechanisms can only be determined by quantifying these flows across multiple scales. To unravel the complex physics of high-mass star formation, it is essential to examine the intricate structures and dynamics of the molecular clouds that serve as their

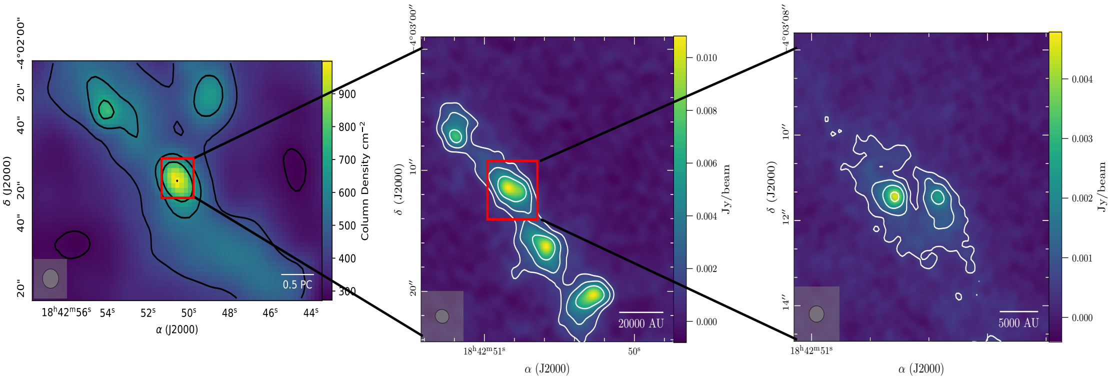

Figure 4.1: Three panel continuum figure showing the different data scales. *Left:* Reprojected Marsh et al. (2017) column density map of region AG028.3+0.06 to match the IRAM 30m data scales at 12″ spatial resolution. Contours overlaid in black (5 σ levels), with 0.5 pc scale bar. *Middle:* Zoom in of the large scale clumps to reveal the ALMAGAL intermediate scale cores, continuum contours (levels 3,6,9 σ_{cont}) overlaid in white, with 20 000 au scale bar. *Right:* Zoom in of one of the intermediate scale cores to reveal ALMAGAL small scale cores, continuum contours (levels 3,6,9 σ_{cont}) overlaid in white with a 5000 au scale bar.

birthplaces. High-mass stars challenge our understanding of stellar evolution due to their rapid formation, intense radiation fields, and significant feedback mechanisms (e.g., Kahn 1974; Yorke & Kruegel 1977; Wolfire & Cassinelli 1987; Zinnecker & Yorke 2007; Arce et al. 2007; Frank et al. 2014; Smith et al. 2009; Zhang et al. 2015; Motte et al. 2018; Kuiper & Hosokawa 2018). The process by which these stars form is not yet fully understood, and an important aspect of understanding this process comes from their formation environments.

The primary sites of star formation are Giant Molecular Clouds (GMCs), these are vast, cold, and dense regions of interstellar gas and dust. Within these clouds, gravitational collapse initiates star formation, but there are many influences along the way such as turbulence, magnetic fields, and external forces such as supernovae (e.g., Zinnecker 1984; Lada & Lada 2003; Bonnell et al. 2003; Bressert et al. 2010; Traficante et al. 2017; Urquhart et al. 2018; Svoboda et al. 2019). One of the most prominent and critical features of GMCs is the presence of filamentary structures that can stretch across parsec scales, and are also present on smaller scales (Hacar et al., 2023). These filaments act as vital conduits, channelling material from the large-scale cloud down to the scales of individual protostellar cores.

Filamentary structures are believed to form from the gravitational collapse of gas along certain linear pathways, often influenced by magnetic fields and turbulence within the cloud. These structures serve not only as a means of material transport but also as sites where dense cores form, which can eventually collapse to give birth to new stars. (e.g., Fiege & Pudritz 2000; Jackson et al. 2010; Kirk et al. 2013; Gómez & Vázquez-Semadeni 2014; Henshaw et al. 2014; Chira et al. 2018; Padoan et al. 2020b; Alves et al. 2020; Beuther et al. 2020; Schisano et al. 2020; Hacar et al. 2023; Pillsworth & Pudritz 2024; Wells et al. 2024). As material funnels through these filaments, the density and pressure increase, leading to core formation and ultimately triggering the formation of a star. The hierarchical nature of mass flows within GMCs, where material is transferred across different spatial scales—from the large, diffuse cloud down to the dense, star-forming cores—suggests that understanding these multi-scale dynamics is essential in explaining how high-mass stars gain their mass and evolve. The mass transfer across these different spatial scales is a central concept in understanding high-mass star formation. The dynamics of how mass flows from the large-scale environment down to the dense cores directly influence the rate at which protostars grow and the type of feedback they generate. Thus, a detailed understanding of the role of filaments, their interactions with surrounding gas, and the overall dynamics of the molecular cloud is crucial for developing a comprehensive picture of how high-mass stars are born and how they evolve throughout their lifecycle.

Although previous studies have focused on either cloud-scale accretion (e.g., Ragan et al. 2014; Zucker et al. 2015; Hacar et al. 2018) or small-scale accretion onto individual cores (e.g., Peretto et al. 2013; Sanhueza et al. 2021; Redaelli et al. 2022), a direct observational connection between these scales remains largely unexplored. Theoretical models predict that accretion should proceed in a self-similar manner across scales, with gravitational collapse driving material inward from GMCs down to protostellar envelopes. However, magnetic fields, turbulence, and radiative feedback may introduce scale-dependent variations in flow rates, potentially disrupting this simple picture (e.g., Krumholz & Federrath 2019; Vázquez-Semadeni et al. 2019; Padoan et al. 2020a; Zhao et al. 2024). By examining flows consistently across multiple scales, we can assess whether accretion mechanisms remain continuous or if different physical processes dominate at different stages of evolution. Incorporating evolutionary stage as a context to set these results in also allows us to investigate any trends with respect to evolution at the different spatial scales.

In this paper, we investigate the flow rates in 10 high-mass star-forming regions at three distinct spatial scales by systematically measuring flow rates at each of these levels, we aim to establish whether material transport remains self-similar across these differing orders of magnitude in spatial extent, or if accretion patterns change as gas moves toward smaller structures. The structure of the paper is as follows: an overview of the three data sets and the telescopes they were observed on is given in Sect. 4.2, along with an introduction to the 10 targets this work focuses on. In Sect. 4.3, we discuss the different methods used for calculating the flow rates at these different scales. Results of the flow rate calculation are presented in Sect. 4.4. Discussions on how these scales link to each other, literature comparisons, and result interpretations can be found in Sect. 4.5. We summarise our findings in Sect. 4.6, along with discussing future ideas.

Table 4.1: Parameters for the 10 regions.

Source name	RA	DEC	v_{lsr} km s^{-1}	Classification	Distance pc	Mass M$_\odot$	L_{bol} L$_\odot$	I_{cores}	S_{cores}
AG022.5-0.19	18:32:59.600	-09:20:03.320	74.8	Quiescent	4060	524	564	1	4
AG031.0-0.11	18:48:21.030	-01:45:00.180	77.1	Quiescent	4400	781	114	3	3
AG023.9+0.15	18:34:28.670	-07:52:16.860	82.7	Protostellar	4730	1691	188	2	3
AG028.3+0.06	18:42:50.580	-04:03:11.570	79.2	Protostellar	4490	1075	513	4	7
AG018.9-0.07	18:25:50.970	-12:25:45.240	62.6	Protostellar	4200	643	277	1	3
AG030.0-0.12	18:46:31.580	-02:39:32.730	99.5	Protostellar	5530	2220	302	1	1
AG029.5-0.61	18:47:31.660	-03:15:12.260	76.3	YSO	4350	2246	3108	3	4
AG025.1-0.27	18:38:09.590	-07:02:32.300	64.5	YSO	3920	1576	1094	4	7
AG023.2+0.07	18:33:23.910	-08:33:32.910	78.4	HII Region	4580	750	20784	2	5
AG024.4-0.22	18:36:40.650	-07:39:13.940	59.5	HII Region	3730	1641	7267	3	7

Notes. Distance, mass and luminosity values can be found with their associated errors in Molinari et al. (2025). I_{cores} and S_{cores} are the number of identified cores at the intermediate scale and small scale respectively.

4.2 Data

This project makes use of three different data sets, each looking at the same 10 regions. The first, and the largest scale, is data from the IRAM 30m telescope proposal 102-23, newly observed for this work. The intermediate and small spatial scales come from the ALMA Evolutionary Study of High Mass Proto-cluster Formation in the Galaxy (ALMAGAL) survey (Molinari et al., 2025). The regions and their parameters can be found in Table 4.1.

4.2.1 IRAM 30m

All 10 regions were observed with the IRAM 30m in April 2024 (project code 102-23). We used the on-the-fly mode to create maps centered on each region, all between 4-8 arcmin^2 in area. We observed line emission in band E2 (1.3 mm). The tuning of the receiver was such that we had the lower side-band (LSB) ranging from 212.808 GHz to 220.891 GHz and the upper side-band (USB) ranging from 228.803 GHz to 236.899 GHz. We used the Fourier Transform Spectrometer (FTS200) backend. This uses 195 kHz channels, which correspond to 0.33 km s^{-1} at 218.222 GHz and 0.34 km s^{-1} at 219.560 GHz. During the data reduction this was set to 0.5 km s^{-1}. The observations were completed with a total integration time of 21.9 hours, with roughly 1.2-2 hours per sources, with a resulting typical RMS of 0.2 K in 0.5 km s^{-1} channels. The observation data was reduced with CLASS in the GILDAS[1] package developed by IRAM.

4.2.2 ALMAGAL

The ALMAGAL large program[2] comprises of 1013 dense clumps that span the full evolutionary sequence described in Urquhart et al. (2022). These sources were selected from the Herschel Hi-GAL survey (Molinari et al. 2010a; Elia et al. 2017, 2021) and the Red MSX Source (RMS) survey (Hoare et al. 2005; Urquhart et al. 2007; Lumsden et al. 2013). For a comprehensive overview of the survey and details on data reduction, see Molinari et al. (2025) and Sánchez-Monge et al. (2025).

Observations were conducted using ALMA Band 6, covering frequencies between 217 and 221 GHz (corresponding to 1.3 mm). The ALMAGAL spectral setup includes four spectral windows: two broad windows for detecting continuum emission and a wide range of spectral lines at a low spectral resolution of 1.3 km s^{-1}, and two narrower windows targeting specific molecular species at a higher spectral resolution of 0.3 km s^{-1}. In this work, we utilise the spectral lines H_2CO ($3_{0,3}$ - $2_{0,2}$) at 218.222 GHz.

---

[1] https://www.iram.fr/IRAMFR/GILDAS

[2] 2019.1.00195.L; PIs: Sergio Molinari, Peter Schilke, Cara Battersby, Paul Ho

The ALMAGAL data products used in this study are a combination of observations from three different ALMA array configurations: two configurations of the main 12m ALMA array and one from the 7m Atacama Compact Array. This combination allows for angular scales ranging from $0.3''$ to $10''$, capturing structures across a broad range of spatial resolutions. The smallest-scale structures analysed in this work are derived from the combination of all three array configurations (hereafter referred to as 7MTM1TM2), while the intermediate-scale structures are obtained using data from the 7m array combined with the most compact 12m array configuration (hereafter 7MTM2).

Before analysing the regions, the ALMAGAL sample was sorted into four evolutionary stages; Quiescent, Protostellar, Young Stellar Object (YSO), and HII regions using the classification scheme from Urquhart et al. (2022). This classification is based on emission at three infrared wavelengths: Hi-GAL 70 µm (Elia et al., 2017), MIPSGAL 24 µm (Carey et al., 2009), and GLIMPSE 8 µm (Churchwell et al., 2009). Emission patterns at these wavelengths distinguish the evolutionary stages, for further information on the classification process see Urquhart et al. (2022); Wells et al. (2022, 2024). Initially the ALMAGAL sources were cross-matched with the ATLASGAL (Schuller et al. 2009; Urquhart et al. 2018, 2022) catalogue using a $40''$ radius, yielding $\sim$ 600 matches out of 1013. Remaining sources were visually classified using the same criteria.

The flow rate analysis in this work is based on Wells et al. (2024). In that work they take the intermediate scale 7MTM2 data and calculate flow rates for a subset of 100 ALMAGAL regions. The intermediate scales data and results from that study is used in this work and we add the large and small scales.

4.3 Methods

Flow rates along filamentary structures leading to cores are estimated for each data set following the method outlined in Wells et al. (2024). The mass flow rate ($\dot{M}$) is given by:

$$\dot{M} = \Sigma \cdot \Delta v \cdot w \cdot \frac{1}{\tan(i)}, \tag{4.3.1}$$

where Σ is column density, Δv is velocity difference, and w is the width of the measurement region. We note the $1/\tan(i)$ factor for unknown inclination, i. Values are converted to solar masses per year, with further parameter details provided in Wells et al. (2024). We will give an overview here but for an in-depth description please refer to that work.

4.3.1 Structure identification

Figure 4.1 shows an example region with the three datasets for the three different spatial scales. We cover scales from several pc down to roughly thousands of au.

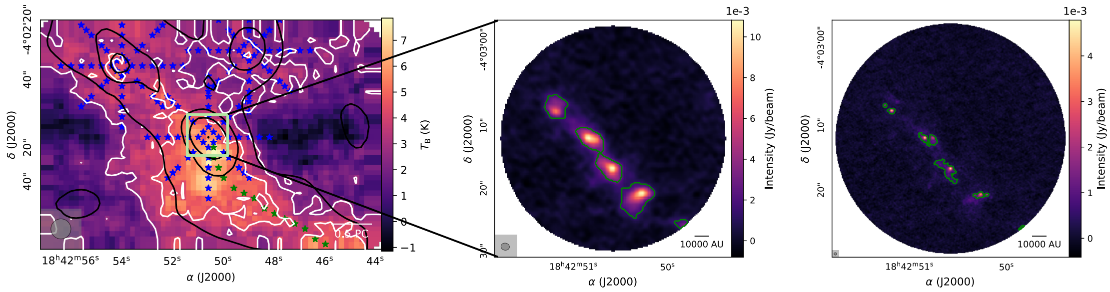

Figure 4.2: Three panel figure showing structure identification at each scale. *Left:* IRAM 30m $C^{18}O$ (2-1) 0th moment map of region AG028.3+0.06, Marsh et al. (2017) column density contours overlaid in black (5 σ levels), IRAM 30m $C^{18}O$ (2-1) 0th moment contours overlaid in white (5 $\sigma_{\rm line}$ levels). Blue stars indicate points where "polar" flow rates, around the hubs are calculated, green stars indicate points along identified extended filamentary structure where the flow rates are calculated. *Middle:* ALMAGAL intermediate scale cores identified with the `astrodendro` package where the green contours indicate the identified cores, background is ALMAGAL continuum. *Right:* ALMAGAL small scale cores identified with the `astrodendro` package where the green contours indicate the identified cores, background is ALMAGAL continuum.

For the large scale we have line data from the IRAM 30m, but for structure identification we use continuum maps. We used the Hi-GAL column density maps from Marsh et al. (2017) made using the PPMAP tool. The large scale structure, filaments and hubs, were determined in the continuum data. Hubs were identified by eye and the peak column density pixel used as the central reference point. For any extended filamentary structure the spine was defined along the filament through the pixels with highest column density values. This is demonstrated in the left panel of Fig. 4.2 which shows region AG028.3+0.06 and its identified structure.

Identification of cores and their extended structure for the intermediate and small scales was done using the `astrodendro` program on the continuum data for each of the targets. This gives us the peak position of the identified cores, along with estimates of their peak and integrated flux density values. The structures we are interested in are the 'leaves', as these are our core structures. The `astrodendro` program requires three main inputs, the minimum pixel intensity to be considered, the minimum height for any local maximum to be defined as an independent entity, and the minimum number of pixels for a leaf to be defined as an independent entity. We use $min\_value = 5\ \sigma_{\rm cont}$, $min\_delta = 5\ \sigma_{\rm cont}$ and min_npix = beam area. Examples of this can be seen in the middle and right panels of Fig. 4.2, showing the identified cores ('leaves') for the intermediate and small scale ALMAGAL data.

4.3.2 Column density

For the large scales, column density values were taken from the Marsh et al. (2017) column density maps, which were calculated with temperature maps of each region. For the intermediate and smaller scales we made column density maps using modified black body emission, assuming optically thin dust emission (Schuller et al., 2009).

The column density is calculated as:

$$N_{\mathrm{H}_2} = \frac{F_\nu R}{B_\nu(T_{\mathrm{D}})\Omega\kappa_\nu \mu m_{\mathrm{H}}}. \tag{4.3.2}$$

Relevant assumptions include a gas-to-dust mass ratio of 150 (Draine, 2011), an opacity value interpolated to 1300 µm, and mean molecular weight $\mu = 2.8$. Several approaches were looked into to estimate temperature, including molecular line tracers and dust temperatures from Hi-GAL (Elia et al., 2017). A method based on luminosity-to-mass (L/M) ratios was tested against the Hi-GAL dust temperatures:

$$T(L/M) = \begin{cases} 20\ \mathrm{K} & \text{if} \quad L/M < 1, \\ 35\ \mathrm{K} & \text{if} \quad 1 \leq L/M < 10, \\ \max(21.1 L/M^{0.22}, 35\ \mathrm{K}) & \text{if} \quad L/M > 10. \end{cases}$$

Comparison between gas and dust temperatures revealed minor differences (5-10 %), noting that within the intrinsic temperature uncertainties these are roughly in agreement, the gas temperatures were ultimately preferred for flow rate calculations as they take the warmer protostellar cores into account.

4.3.3 Width determination

The width w in the flow rate calculation corresponds to the measurement area between points along or around the filament. For the large scale data we took 2/3 beam size, 8″, which corresponds to two pixels in the data cubes. For intermediate and small scales we took four measurement positions per core at beam size spacings, $\sim 1''$ for the intermediate scale and $\sim 0.6''$ for the small scale. Distance variations (2-6 kpc) were considered, but no significant distance dependence in flow rates was found (Wells et al., 2024).

4.3.4 Velocity difference

For the large scale first moment maps, and hence the velocity analysis, we used C^{18}O (2-1) for each region. H$_2$CO ($3_{0,3}$ - $2_{0,2}$), H$_2$CO ($3_{2,2}$ - $2_{2,1}$) and C^{18}O (2-1) were all investigated prior to this decision, however neither H$_2$CO lines were reliably detected in all regions, where as the C^{18}O (2-1) was strong in all regions and traced similar structures as the continuum for each region. The emission typically exhibits simple Gaussian profiles, hence the first moment gives a meaningful statistical description of the peak velocity, so we decided to continue with the C^{18}O (2-1) for the velocity analysis. We took the velocities from the pixel values of the first moment maps, and calculated the velocity difference between that value and the source rest velocity.

Velocity differences for the intermediate and small scales were derived using the KeplerFit code (Bosco et al., 2019). The strongest opposing quadrants in the

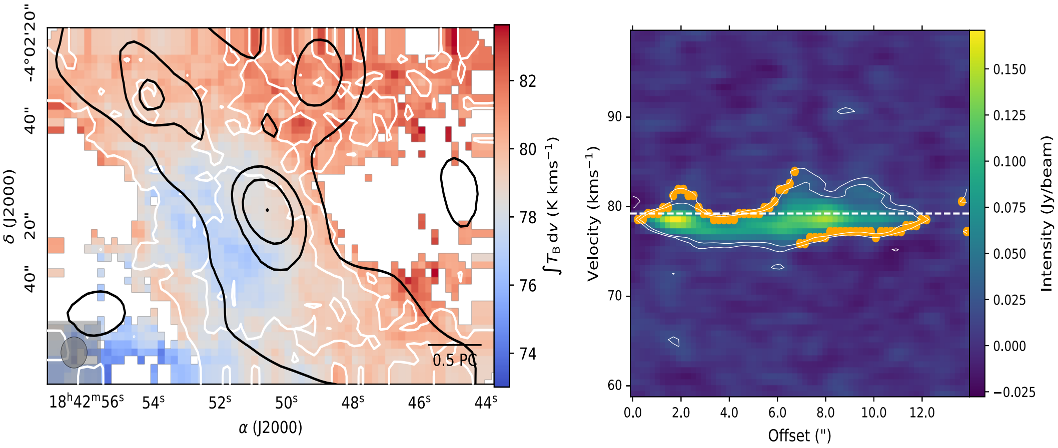

Figure 4.3: Two panel figure showing velocity analysis at different scales. *Left:* IRAM 30m $C^{18}O$ first moment map of region AG028.3+0.06, Marsh et al. (2017) column density contours (5 σ levels) overlaid in black, IRAM 30m $C^{18}O$ moment 0 contours (5 σ_{line} levels) overlaid in white. *Right:* PV cut with 3 and 5 σ_{line} contours in white, and the V_{LSR} of the region shown by the white dashed line. The orange points show the nearest pixels at the 3 σ_{line} contours.

PV diagram were selected, and the velocity difference was measured using the $3\sigma_{\mathrm{line}}$ contour. Rest velocities were compared to core peak velocities from H_2CO ($3_{0,3}$ - $2_{0,2}$) moment maps, with differences generally below the velocity resolution (0.6 km s^{-1}), confirming the rest velocity as a reliable reference. For further details on calculations and assumptions, refer to Wells et al. (2024).

4.3.5 Sources of error

Similarly across all scales we calculate effects from the associated errors to the parameters we are using. For the large scale we consider column density, distance, width and velocity difference (Wells et al., 2024). Those we consider for the intermediate and small scale are the flux density, temperature, distance, width, and velocity difference. To calculate the effects this has on our overall results we use Gaussian error propagation for Eq. (4.3.1). For the large scale, looking at Marsh et al. (2017) we take a 50 % error for the column density maps, for width we take 4″ for on sky offset discrepancy. For the intermediate and small scales we take the information from Wells et al. (2024); 10 % for the flux density from the calibration uncertainty, for temperature, we take 5 K and for width we take 0.1″ for on sky offset discrepancy. For all three scales we assume a kinematic distance error of 0.5 kpc, and for the velocity differences we take the spectral resolution of 0.6 km s^{-1} as the error from the nearest pixel approximation. When combining these we end up with ± 50 % error margins on the final flow rates.

We note that the equation makes assumptions regarding the origin of the observed velocity differences. To minimise the possibility that these differences arise from outflows, we rely on first moment maps, which trace the peak of the velocity distribution, rather than the wings of the Gaussian profile where outflow signatures typically appear. Although we cannot fully rule out the presence of rotational signatures, by analysing the velocity along the filament's axis, we reduce the influence of filamentary or systemic rotation. In regions near dense clumps, where local rotation or shear may occur, previous studies (e.g., Xu et al. 2020, 2024) show that, such motions contribute minimally. Therefore, we consider flows to be the dominant source of the observed velocity differences in this analysis.

4.4 Results

In the following section we present the results from this work, and we will show examples from the large scale of flow rates radially around the hubs and flows along the filamentary structure, before discussing how these trends appear throughout the 10 sources. We then present sample statistics and distributions for each scale.

Table 4.2: Median flow rate values per region, at the three different scales.

Source	Median$_L$ 10^{-5}	Median$_I$ 10^{-5}	Median$_S$ 10^{-5}
AG022.5-0.19	13.5	3.78	1.83
AG031.0-0.11	11.2	10.5	3.55
AG023.9+0.15	15.0	4.65	4.11
AG028.3+0.06	13.1	13.8	15.5
AG018.9-0.07	4.80	3.00	24.7
AG030.0-0.12	3.70	6.97	0.98
AG029.5-0.61	3.52	9.11	4.74
AG025.1-0.27	13.7	15.2	10.6
AG023.2+0.07	12.4	44.1	50.4
AG024.4-0.22	30.3	40.7	8.89

Notes. All values are in units of $M_\odot\,yr^{-1}$. Subscript L,I and S represent large, intermediate and small scales repectively.

4.4.1 Large scale

First, we present the results for our large scale sample, the 10 parental clouds and their extended environments mapped by the IRAM 30m. Their 0th and 1st moment maps in $C^{18}O$ (2-1) can be seen in Appendix B.2 and B.3. The overall distribution of flow rates for this scale is presented in Sect. 4.4.3 for comparison to the intermediate and smaller scales. In the following subsections we look at the large scale relationships between distance along the filamentary structure and the flow rate, and the flow rates at different annuli, radially around the hubs in these clouds. The points at which we calculate the flow rates can be seen in the left panel of Fig. 4.2.

Along the filaments

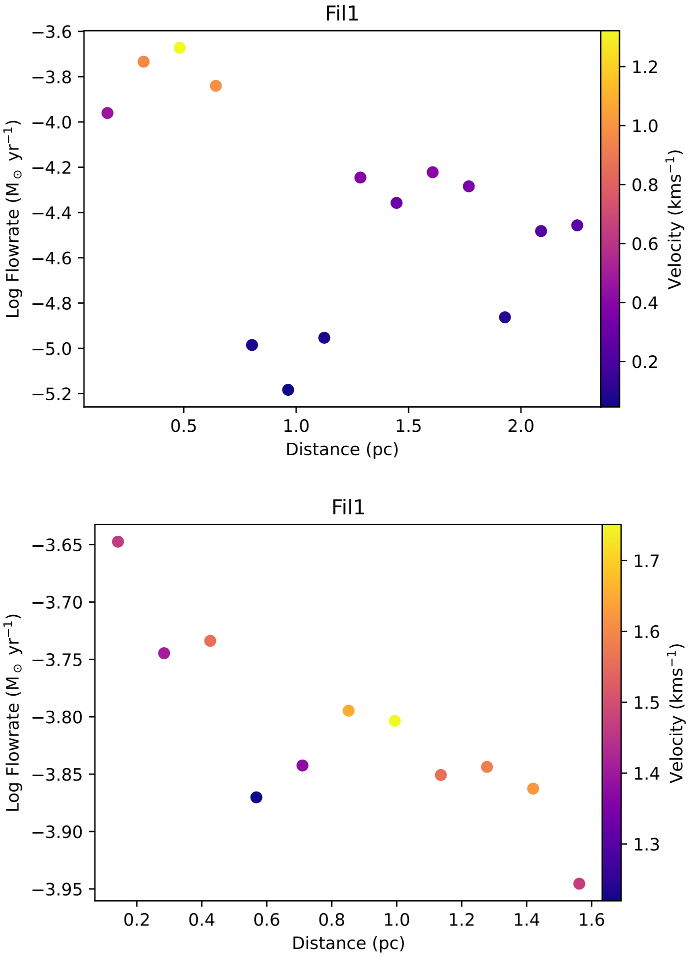

Figure 4.4: Relationship between flow rate and distance. Points are colour coded with the velocity difference. *Top:* for the identified filament in protostellar region AG028.3+0.06 *Bottom:* for the identified filament in YSO region AG025.1-0.27.

Depending on the region we see a different numbers of filaments, some regions have none and are more compact, and some have up to four with connections between hubs. Filamentary structures that are too short (less than 3 points identified) or where two hubs are too close together that the influence from either hub would be indistinguishable are not included. The chosen filaments have varying lengths between 0.5 and 3 pc. In Fig. 4.4 we present the relationship between flow rate and distance from the hub for two regions, AG028.3+0.06 (protostellar, top panel) and AG025.1-0.27 (YSO, bottom panel). We see that region AG028.3+0.06 has one identified filament. How flow rate changes along the filament is shown in the top panel of Fig. 4.4. Around 1 pc we see a significant drop in the flow rate values down to 10^{-5} M$_\odot$ yr^{-1}, indicating that the flow rates are inversely related to the distance from the hub.The points are colour coded by the velocity difference at each point, the largest difference being around 1.2 km s^{-1}, seen close to the core. This is also where we would expect the largest column density values, so combining the two, having the larger flow rates here is not unfounded. Region AG025.1-0.27 also has one identified filament, seen in the bottom panel of Fig. 4.4. We see a small decrease in flow rates further from the core ($10^{-3.65}$ to $10^{-3.95}$ $M_\odot\,yr^{-1}$), however the velocity differences here are a little larger, and there is a smaller range in velocity difference in comparison to the top panel (0.5 vs. 1.0 km s^{-1}). Looking at both filaments we see that the range and magnitude of the velocity difference has a noticeable effect on the flow rates. Figures 4.1, 4.2 and 4.3 for AG025.1-0.27 are available in the Appendix.

Polar around clumps

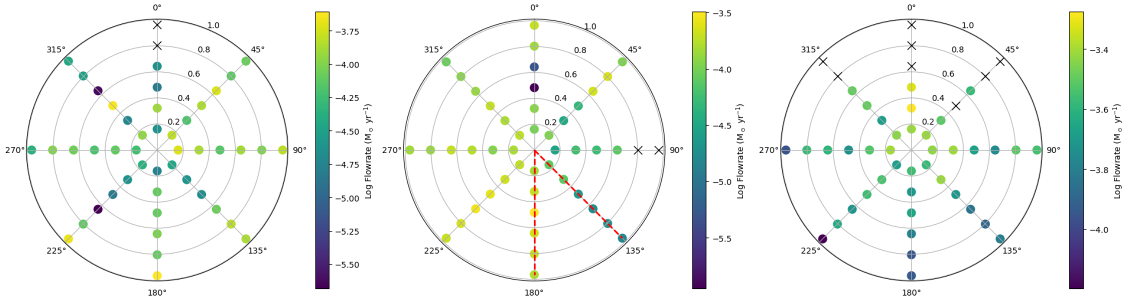

Figure 4.5: Polar plots for the three hubs in the protostellar region AG028.3+0.06, seen from left to right in the left panel of Fig. 4.2. We have six annuli, separated by 2 pixels (give dist in pc), and the points are colour coded on the flow rate value at each annuli and angle around the hub. Red dashed lines indicate angle of any identified filament associated with that hub. Black X points mark locations were the flow rate could not be calculated, either due to the point being out of bounds of the data cube, or there being no velocity information available for that pixel.

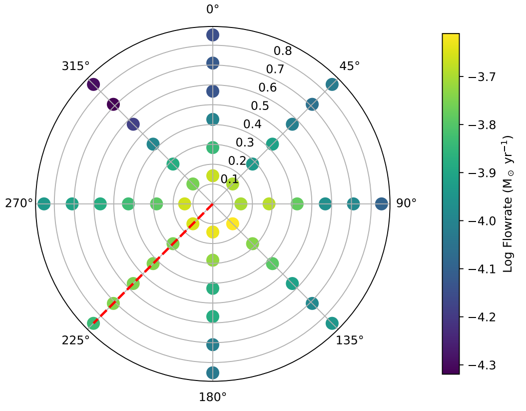

Figure 4.6: Polar plot for the single hub in the YSO region AG025.1-0.27. We have six annuli, separated by 2 pixels (give dist in pc), and the points are colour coded on the flow rate value at each annuli and angle around the hub. Red dashed lines indicate angle of any identified filament associated with that hub.

Looking at how the flow rates change with distance, radially around these hubs can also help identify the primary directions of the flow of material towards the hub.

We note that the regions in our sample have between one and three hubs. Here we show polar plots for the same example regions AG028.3+0.06 and AG025.1-0.27 in Fig. 4.5 and Fig. 4.6. Looking at Fig. 4.5 we see the three hubs have different trends. Looking at the left plot, there is no clear indication of a gradient through the annuli. This hub is in the top left of the structure and we see the column density and velocity covering that region do not display signs of any gradient or concentrations (Figs. 4.2 and 4.3 left panel). The central hub, has higher values all around especially to the lower left where we see lower velocities, and so the velocity difference will be larger in flow rates from this side of the hub. We note that the identified filament falls between the two indicated dashed red lines at 130 and 180°, leading to potential filamentary contributions from these angles. From the top panel of Fig. 4.4 we see flow rates close to the core are $10^{-3.6}$ $\mathrm{M_\odot\,yr^{-1}}$, which is in close agreement with the central annuli along 180°. Looking at region AG025.1-0.27 in Fig. 4.6 we have one central hub where we see all round, clear gradients in the flow rate, increasing towards the core. The direction of the identified filament is marked by the dashed red line, and like AG028.3+0.06 we see the values close to the core in Fig. 4.4 bottom panel match with what we see here in the polar plot at the marked angle.

4.4.2 Small scales

The intermediate scales were initially investigated in the Wells et al. (2024) study. Here we applied the same approach to the same regions at the smaller spatial scales from the ALMAGAL survey. Comparing the number of identified cores at the intermediate scale to the small scale we see fragmentation in almost all regions, and in the regions we do not see this, the identified cores are often compact. We can see an example of this in the middle and right panels of Fig. 4.1 and 4.2. Figure 4.9's right panel shows the distributions of the small scale flow rates according to evolutionary stage. If we look at the right panels we see minimal fluctuations around the mean of the whole distribution (seen in the right panel of Fig. 4.7) through the first three evolutionary stages, with the HII regions being the largest deviation. A notable difference, around a factor two, is seen between the quiescent and HII regions, this is a similar result to the intermediate scale where there is a factor three between these two stages. Overall the median of the small scales is smaller than the intermediate scales, 4.40×10^{-5} $\mathrm{M_\odot\,yr^{-1}}$ vs. 6.28×10^{-5} $\mathrm{M_\odot\,yr^{-1}}$.

4.4.3 Scale comparison

Hierarchical flows from large scales down to small scales can tell us more about the formation and evolution of high mass stars. One of the main aims of this work is to be able to compare the flow rates across multiple scales for 10 different regions, varying in evolutionary stage. Figure 4.7 shows the distribution for each scale, large to small from left to right, independent of evolutionary stage. Looking first to the

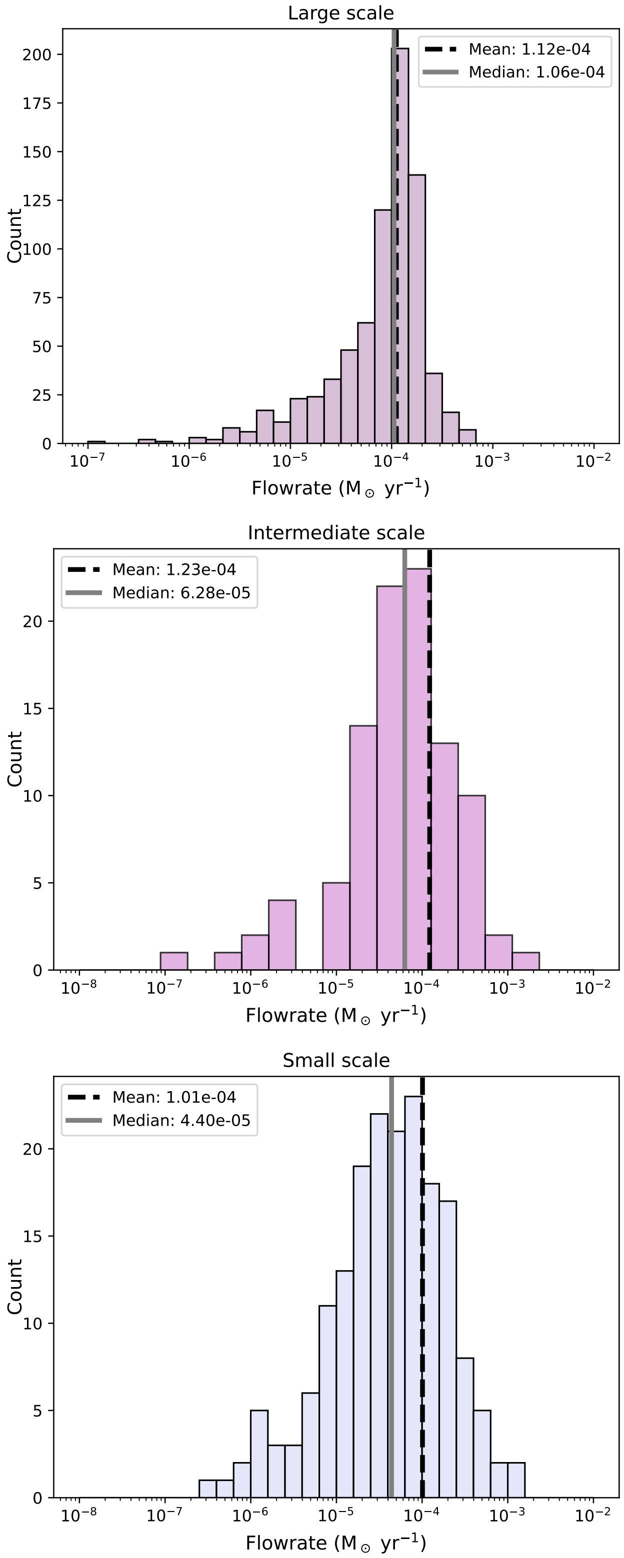

Figure 4.7: Three panel figure showing the distribution of flow rates for the 10 regions at each scale. In all three panels we see the mean, shown with the black dashed line, and the median shown with a solid grey line. *Left:* Large scale distribution *Middle:* Intermediate scale distribution *Right:* Small scale distribution.

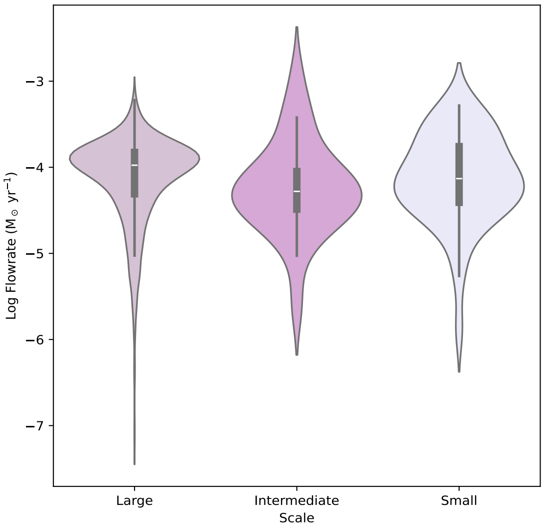

Figure 4.8: Violin plot showing the distributions of flow rates at large, intermediate and small scales. The small white line in the centre is the median, the thick grey bar is the interquartile range and the thin grey line is the rest of the distribution, the the rest determined to be outliers. On each side of the grey line is a kernel density estimation to show the distribution shape of the data.

large scale distribution we see there is a tail on the lower end of the distribution, also seen in Fig. 4.8, and that the distribution is not as wide as the intermediate and small scale distributions. The large scale distribution gives a median value of 1.06×10^{-4} M$_\odot$ yr^{-1}. The intermediate scale (middle panel) also has a small tail to the lower end. The distribution is wider in comparison to the large scale and the mean value is 6.28×10^{-5} M$_\odot$ yr^{-1}. Finally the small scale (right panel) is the widest distribution of the three and also has a tail down to 10^{-7} M$_\odot$ yr^{-1}. The median for the small scale is 4.40×10^{-5} M$_\odot$ yr^{-1}. For a breakdown of median flow rates per scale, per region we refer to Table 4.2.

4.4.4 Evolutionary stage

Figure 4.9 shows a breakdown of the flow rate distributions for each evolutionary stage at all three spatial scales. Looking at Fig. 4.9a (large scale), we see almost no change between quiescent and protostellar, a significant decrease (more than the associated errors of 50 %) to the YSOs by a factor 6 and again to the HII regions by a factor 2. For the intermediate scales, Fig. 4.9b, we see an significant increase between quiescent and protostellar (over a factor 2), but for the later stages they are all similar within the 50 % errors. At the small scale, Fig. 4.9c the median values for all stages are similar within the errors, indicating no significant trend.

Comparing each stage individually across scales we see order of magnitude difference between the large scale and the intermediate and small scales for the quiescent distributions. For protostellar the large scale again has the largest value by a significant amount. The YSO values are almost the same for the large and intermediate

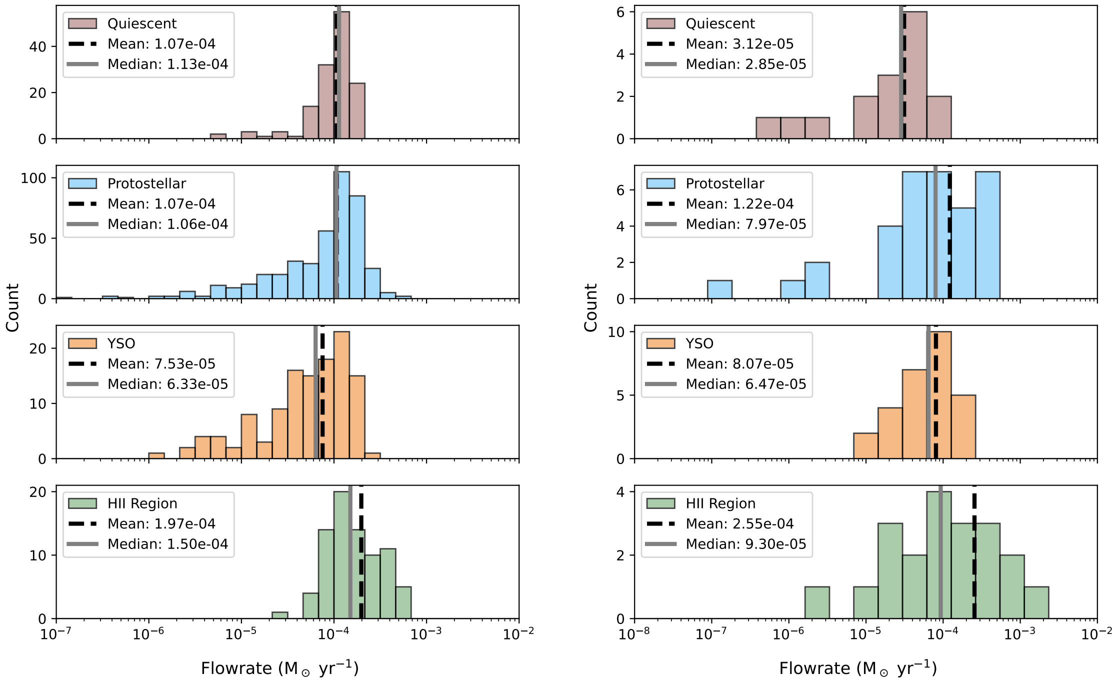

(a) Large scale (a few pc).

(b) Intermediate scale (< 1 pc.

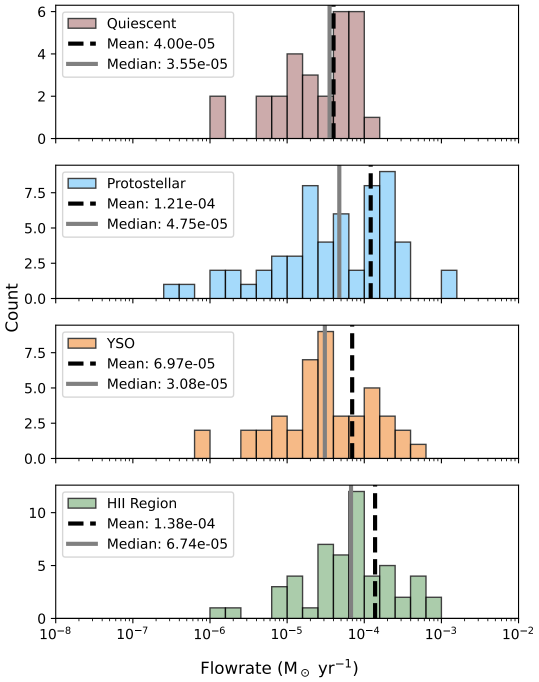

(c) Small scale (a few thousand au).

Figure 4.9: Three panel figure showing distributions for each evolutionary stage at each spatial scale. In all panels we see the mean, shown with the black dashed line, and the median shown with a solid grey line.

scales, with a decrease to the small scale. Finally, the HII regions again have similar large and intermediate scale values and a small decrease to the small scales.

Looking at the relationship between evolutionary stage and spatial scale we observe some variation in flow rates, however, these trends are subtle and not statistically robust across the scales. This can also be seen in Fig. 4.8. These findings are consistent with the results of Wells et al. (2024), who also report tentative trends in flow rate distribution with evolution, but note that these are not universally applicable across all regions.

4.5 Discussion

Observations increasingly support a multi-scale view in which large-scale cloud collapse, filamentary flows, and dense core accretion are connected components of a single process (e.g., Beuther et al. 2007; Motte et al. 2007; André et al. 2014; Beuther et al. 2025). These structures form a nested network in which material funnels from parsec-scale clouds through filaments and hubs, down to clumps and cores. Theoretical studies use observations to constrain models and simulations, with information about trends across multiple scales of the early star formation process we can further strengthen the predictions from these theoretical studies of high-mass star formation.

4.5.1 Different scales

The hierarchical structure in high-mass star formation has been a subject of increasing interest over the last few decades. There is, however, a gap in the literature when it comes to studies that investigate flow rates across different scales simultaneously. While individual studies have provided insight into either large or small-scale accretion, few have attempted to make direct comparisons between these rates or investigate the link between them (e.g, López-Sepulcre et al. 2010; Kirk et al. 2013; Peretto et al. 2013; Henshaw et al. 2014; Traficante et al. 2017; Beuther et al. 2020; Sanhueza et al. 2021; Redaelli et al. 2022; Olguin et al. 2023; Zhang et al. 2024; Wells et al. 2024).

On smaller scales, studies have provided estimates of flow rates directly onto the protostellar object. Notably Kirk et al. 2013 report flow rates of 4.5×10^{-5} $M_\odot\,yr^{-1}$, which is in agreement with our intermediate and small scale values. Work by Krumholz et al. (2009) and Kuiper & Hosokawa (2018) has suggested that these small scale flow rates may be governed by complex dynamics that are influenced by both radiation pressure and magnetic fields, which can significantly affect the efficiency of mass transfer.

Comparable to our large scale, observational studies, such as those by Schneider et al. (2010); Peretto et al. (2013); Henshaw et al. (2014); Beuther et al. (2020), report values on the order of 10^{-4} $M_\odot\,yr^{-1}$ and 10^{-5} $M_\odot\,yr^{-1}$, in line with our regions large scale values. Larger scales such as Traficante et al. (2017) report values on the order 10^{-3} $M_\odot\,yr^{-1}$. Zhang et al. (2014) discuss how surrounding molecular cloud gas and dust are drawn into the star-forming region via gravitational collapse or turbulent motions, concluding that the magnetic field is strong enough on the clump scale to guide the material along the field lines into dense cores. For our sample of 10 regions we can say that overall we see larger values at larger scales, but we do not report a definite or significant trend with respect to the spatial scales.

4.5.2 Theoretical predictions

Since we do not see significant trends in the flow rate relationships, but small variations across scales and evolutionary stages, we relate more towards theoretical models that propose a coherent, hierarchical inflow of material—from cloud scales down to individual cores—as a viable pathway for building up massive stars (e.g., Smith et al. 2009; Vázquez-Semadeni et al. 2019). In the context of global hierarchical collapse, our findings suggest that large-scale gravitational flows can indeed couple effectively to sustain smaller-scale accretion, maintaining a steady supply of material across multiple scales. While fragmentation and feedback may complicate flow geometries locally, our results imply that, on average, the underlying flow rates remain relatively stable, at least within the scales and evolutionary stages that we look at in our sample.

The absence of significant variation and defined trends in these flow rates also raises questions about the role of environmental factors such as turbulence and magnetic fields. Observational evidence for this is presented in the section above, however, simulations by Seifried et al. (2011) show that these effects can induce variability in accretion flows, but it is often a small amount, our results also suggest that any such variability may not dominate the overall flow rates. Instead, accretion may proceed in a somewhat overall steady, filament-fed fashion. This supports the growing view that filamentary structures serve as primary channels for mass transport, effectively linking diffuse cloud material to dense clumps and cores. Theoretical and observational studies (e.g., Fiege & Pudritz 2000; Jackson et al. 2010; Kirk et al. 2013; Gómez & Vázquez-Semadeni 2014; Henshaw et al. 2014; Padoan et al. 2020b; Alves et al. 2020; Beuther et al. 2020; Schisano et al. 2020; Hacar et al. 2023; Wells et al. 2024; Pillsworth & Pudritz 2024; Pillsworth et al. 2025; Hacar et al. 2025) have highlighted the importance of such structures in both low- and high-mass star-forming environments.

Flow rates reported by theoretical work (e.g., Yorke & Sonnhalter 2002; Krumholz et al. 2007; Kuiper et al. 2010; Hennebelle et al. 2011; Kuiper et al. 2011) provide values (10^{-4} $\mathrm{M_\odot\,yr^{-1}}$) that match the ranges we see across the scales. Gómez & Vázquez-Semadeni (2014) also report values at this order of magnitude but for much larger scale filaments (15 pc).

4.6 Conclusions

In this study we looked at 10 large scale high mass star forming regions with the IRAM 30m telescope, we investigated the relationship between flow rates and distance from the hub in these regions, and also investigated the potential presence of trends across evolutionary stages. We then compared the flow rate distributions to those we calculated across intermediate and smaller scales of the same 10 regions using data from the ALMAGAL survey. Our main findings are summarised in the points below;

- Having data on three spatial scales (a few pc, $< 1\,\mathrm{pc}$ and a few thousand au) allows us to examine flow rate relationships and properties continuously through these scales and compare the individual results per scale.
- At the large scale we see a range of filamentary structures depending on the region. The relationship between flow rate and distance from the clump either decreases with distance or has little variation.
- Looking at flow rates from all directions onto the large scale clumps we see correlation with the direction of the highest flow rates and the direction of the identified filament(s) in the region. We also see gradients towards the core of increasing flow rates.
- The distributions of the flow rates across the three scales see decreasing median values (1.06×10^{-4} $\mathrm{M_\odot\,yr^{-1}}$, 6.28×10^{-5} $\mathrm{M_\odot\,yr^{-1}}$, 4.40×10^{-5} $\mathrm{M_\odot\,yr^{-1}}$) and widening distributions. When taking into account 50 % errors these values show a decreasing trend but are not statistically significant.
- The relationship between evolutionary stage and flow rate for the different scales shows small variations but no definite trends.

Looking at the processes of high-mass star formation across many spatial scales is a unique advantage for comparison and discussion. Here we utilised this opportunity to look at how the flow of material differs at different scales but further multi-scale studies are needed in the future with larger samples and a wider range of scales looking at other processes that are significant to high-mass star formation.

5

ADVANCING OUR UNDERSTANDING OF HIGH-MASS STAR FORMATION

Understanding how gas accretes onto structures in star-forming regions, from large-scale filaments and clumps down to small-scale cores, is central to building a comprehensive picture of star formation. This thesis set out to explore the broad question:

What are the properties of accretion flows in and onto star-forming clusters?

To address this, a combination of observational and theoretical approaches was employed across a range of spatial scales and environments. The observational results come from data obtained from the ALMAGAL survey, complemented by large-scale mapping from the IRAM 30m telescope. The ALMAGAL data, with resolutions ranging from $\sim 0.6''$ to $1''$, allowed for detailed analysis of gas kinematics and structure within star-forming regions across various evolutionary stages – quiescent, protostellar, YSOs, and HII regions. Using continuum and line emission, particularly H_2CO ($3_{0,3}$ - $2_{0,2}$) and $C^{18}O$ (2-1), we investigated velocity gradients around dense cores and along filamentary structures. Cores were identified using a dendrogram-structure based method, and position-velocity cuts were employed to trace the gas flows. Flow rates onto individual cores were estimated by combining velocity gradients with column density measurements. The IRAM 30m observations, with $12''$ resolution, provided complementary large-scale context, enabling the identification of clumps and extended filaments feeding into smaller-scale structures, and large scale flow rates to be calculated. Together, these datasets enabled the calculation of flow rates across three spatial scales offering a comprehensive view of the hierarchical accretion processes driving high-mass star formation. Theoretical insights were obtained from the analysis of galactic MHD simulations, which modelled filamentary structures and clump formation under both feedback-dominated and non-feedback dominated conditions. Filamentary skeletons were extracted using the `FilFinder` algorithm, and flow rates were computed along the filaments, onto them from the surrounding environment, and radially around the clumps. The simulation analysis highlighted the role of environmental feedback and inclination effects on observed flow rate trends.

5.0.1 Summary of results

Chapter 2 focused on observational measurements of flow rate properties onto ~ 180 cores at ($< 1\,\mathrm{pc}$) scale using data from the ALMAGAL survey. This study of a large sample of cores allowed a robust investigation into the properties of flow rates. Analysing approximately 700 flow rates revealed trends of increasing flow rates with respect to evolutionary stage, with the largest values being seen in the more advanced stages, the YSOs and HII regions, where the accretion is strongest and continuous before dispersal. It is also seen that the flow rates are larger towards the centre of the cores, where all flows from the extended environment come together. There is a strong correlation between the flow rates and the mass of the core, $\sim \mathrm{M}^{2/3}$, which supports the "tidal-lobe" accretion mechanism, suggesting that massive cores dominate accretion in a way consistent with their gravitational influence on the surrounding gas.

Chapter 3 explored synthetic observations of different galactic star forming environments, allowing us to test the robustness of observational methods, and investigate the relationships between flow rates and the environment. This study shows that filaments are crucial to the transport of material to the central clump. The radial direction where the primary filaments connect to the hub are where the highest flow rates are. By investigating the flows from the environment onto the primary filaments it is shown that these flows from the environment are enough to sustain those we see along the filaments. Notably, a difference in behaviour between feedback and non-feedback dominated environments is seen, with feeder filaments playing a significant role. In the feedback-dominated region flow rates tend to decrease towards the central clump, a pattern explained by the presence of multiple feeder filaments distributing the flow from the primary filament into various paths onto the central clump. In the region where feedback is not as prevalent, there are higher flow rates near the core, suggesting a more centralised accumulation of material. The progressive merging of feeder filaments into primary filaments in these regions supports a sustained material flow towards the central clumps. Additionally, the impact of both galactic and filamentary inclination angles was qualitatively studied for two selected filaments. Varying the galactic inclination reveals more information about the structure of the filament-clump system, and the filamentary inclination allowed a better estimate of the flow rates along those filaments, showing that with unknown inclination angle we see both overestimation and underestimation of the flow rates.

Chapter 4 investigated accretion flows across three spatial scales (a few pc, $<$ 1 pc, a few thousand au) in ten different regions using a combination of data from the ALMAGAL survey and the IRAM 30m. This unique combination of datasets enabled assessment of whether flow properties change systematically with scale. Results indicate that at large scales (a few pc) flow rates are either increasing towards the central clump or show little variation with distance. At this scale, looking radially around the hubs there are clear gradients of increasing flow rates towards the centre of the clump, and correlation with filament direction and the direction of highest flow rates onto the clump. The distributions of flow rates across the three spatial scales have a trend of decreasing median values. At the large scale, flow rates are required to sustain the formation of a cluster, with multiple star-forming cores, where as moving towards intermediate and smaller scales, the flow rates are then focused on individual cores, so less material transport is required from the environment into the cores at these scales. With respect to evolutionary stage there are small variations but no definitive correlations with scale. It is seen that the YSOs and HII regions tend to have the largest values through all spatial scales.

5.0.2 Thesis conclusions

Collectively, the results from these chapters provide a more complete view of accretion flow properties in star-forming clusters. Several overarching conclusions emerge:

- **Observational support of the tidal-lobe accretion mechanism** — Accretion flow rates are most strongly influenced by core mass, with a relationship of $M^{2/3}$, suggesting that massive cores potential is dominated by the gas.
- **Galactic environment influence** — Simulated galactic environments demonstrate that feedback levels in the environment significantly affect flow structure and values, in regions with higher feedback feeder filaments channel material from the primary filaments to feed the clumps. Whereas in environments with less feedback, feeder filaments directly supply material from the surroundings to the primary filaments themselves.
- **Filaments are sustained from their environments** — Looking at the flow rates from the environment onto the filaments shows values that sustain those flow rate values along the filaments themselves, towards the central clumps.
- **Multi-scale variations of flow rates** — Multi-scale analysis reveals that the median flow rate values have a decreasing trend from larger to smaller spatial scales as flow rates go from supplying a whole stellar cluster to individual cores.
- **Flows and evolutionary stage** — The observational data shows that the more evolved sources, YSOs and HII regions, tend to have the largest flow

rates of all the evolutionary stages. This is true for all spatial scales in this work.

- **Confidence in the flow rate method** — Comparing the observational results with other studies in the literature, and the theoretical flow rates with their true flow rates from the simulations allowed testing of the flow rate calculation method. Seeing similar values in each study gives confidence in this method.

These findings contribute to ongoing efforts to bridge the gap between theoretical models and observational data in star formation studies. By quantifying flow behaviours across a range of scales and conditions, this thesis advances our understanding of how mass is assembled and redistributed within star-forming environments.

While many open questions remain, this thesis provides new insights into the nature of accretion flows in clustered star-forming regions. By integrating observations, theory, and multi-scale analysis, it offers a step forward in decoding the complex interplay between gravity, environment, and structure that drives the birth of stars.

5.1 Outlook: The importance of studying high-mass star formation

High-mass star formation remains a fundamental area of study in astrophysics, with significant implications for our understanding of galactic evolution, stellar feedback, and the cosmic distribution of heavy elements (e.g., Wolfire & Cassinelli 1987; Zinnecker & Yorke 2007; Arce et al. 2007; Smith et al. 2009; Kuiper & Hosokawa 2018). Massive stars play a critical role in shaping their surrounding environments, influencing star formation processes on both local and galactic scales. While substantial progress has been made in understanding the mechanisms driving the formation of massive stars, critical gaps persist, particularly in the quantification of mass accretion processes across multiple scales and environments. Bridging these gaps requires the combination of theoretical models and observational data to construct a comprehensive framework for high-mass star formation. Addressing these unresolved questions will enhance our ability to predict star formation outcomes across diverse galactic conditions and refine our understanding of the physical principles governing stellar evolution.

Following on from this thesis, three key questions remain central to advancing our understanding of high-mass accretion:

1. **How do accretion rates evolve quantitatively from large-scale clouds down to individual small-scale cores?**
2. **How do accretion rates evolve with time?**
3. **How much does the environment influence accretion flows?**

Each of these questions addresses a crucial aspect of the accretion process, building directly on the findings presented in this thesis. Some of these questions are natural extensions of the studies carried out here, while others represent new directions inspired by the results. Together, they highlight key areas for future exploration in the field of high-mass star formation. The following sections explore these questions in detail, outlining the current understanding and future ideas for research.

5.1.1 Towards a unified picture of accretion across multiple scales

A key challenge in the field is linking accretion processes across scales, from galactic structures down to individual protostellar cores. Observational studies have identified large-scale accretion flows that are feeding molecular clouds (e.g., 'Maggie' (Syed et al., 2022), 'Nessie' (Jackson et al., 2010), and the Radcliffe wave (Alves et al., 2020)), while smaller-scale studies have focused on filamentary structures and individual star-forming cores (e.g., Kirk et al. 2013; Henshaw et al. 2014; Beuther et al. 2020). However, a comprehensive understanding of how accretion transitions across these scales remains elusive, as discussed in Chapter 4.

Expanding on current data, future studies can systematically investigate the continuity of mass accretion across scales and compare observed flow rates with theoretical predictions for large clouds or individual cores (e.g., Padoan et al. 2020b; Gómez & Vázquez-Semadeni 2014). By combining large-scale galactic plane surveys (e.g., SEDIGISM, GRS) with high-resolution interferometric observations, it will be possible to construct a robust statistical framework for characterising accretion processes across a range of spatial scales.

5.1.2 Time evolution of accretion flows

Another major avenue for future exploration is the evolution of accretion rates over time. Given the long evolutionary timescales of star formation, direct observational tracking of individual systems is not feasible. However, progress can be made by studying synthetic star-forming regions at different evolutionary stages, from quiescent molecular clouds to active HII regions, using galactic simulations. Comparative studies across different time stamps will help constrain how accretion rates change as clouds collapse and evolve into star-forming cores.

Incorporating simulations and observational analyses of regions at different stages of evolution will enable a more complete understanding of the timescales and mechanisms governing accretion flows. A future research priority will be refining theoretical models to better replicate the observed variations in accretion rates across different evolutionary stages.

5.1.3 Environmental influences on accretion flows

The impact of environmental conditions on accretion processes remains an open question. Variations in star formation activity between the inner and outer regions of the Milky Way, as well as differences observed in spiral arms versus inter-arm regions, suggest that accretion processes are influenced by external conditions such as turbulence, radiation fields, and cloud density (e.g., Mills & Morris 2013; Krieger et al. 2017; Henshaw et al. 2019). Understanding these dependencies is essential for developing a predictive framework for high-mass star formation in diverse galactic environments.

The Central Molecular Zone (CMZ), with its extreme physical conditions, provides an excellent playground for investigating how accretion mechanisms operate in environments that resemble those found in high-redshift galaxies. Future studies, utilising data from the ALMA CMZ Exploration Survey (ACES) (PI: S. Longmore, Co-Is: C. Battersby, J. Bally, J, Henshaw et al.) will offer valuable insights into the nature of star formation in dense, turbulent environments. Similarly, upcoming surveys like the Outer Galaxy High-Resolution Survey (OGHReS) will help characterise how accretion processes differ in the low-density outer regions of the Milky Way (Urquhart et al., 2024). Expanding these investigations will be key to determining whether universal accretion mechanisms exist or if environmental factors lead to fundamentally different modes of star formation.

5.1.4 The future of high-mass star formation research

The next decade of research in high-mass star formation will be driven by further integrating multi-scale observations, numerical simulations, and comparative studies across diverse galactic environments. By addressing the aforementioned key unanswered questions, studies will provide a more complete picture of the processes governing massive star formation. As observational capabilities continue to advance, new datasets will enable increasingly precise constraints on the mechanisms that shape our galaxy and the broader universe.

A

Additional material to Chapter 2

A.1 Sample parameter histograms

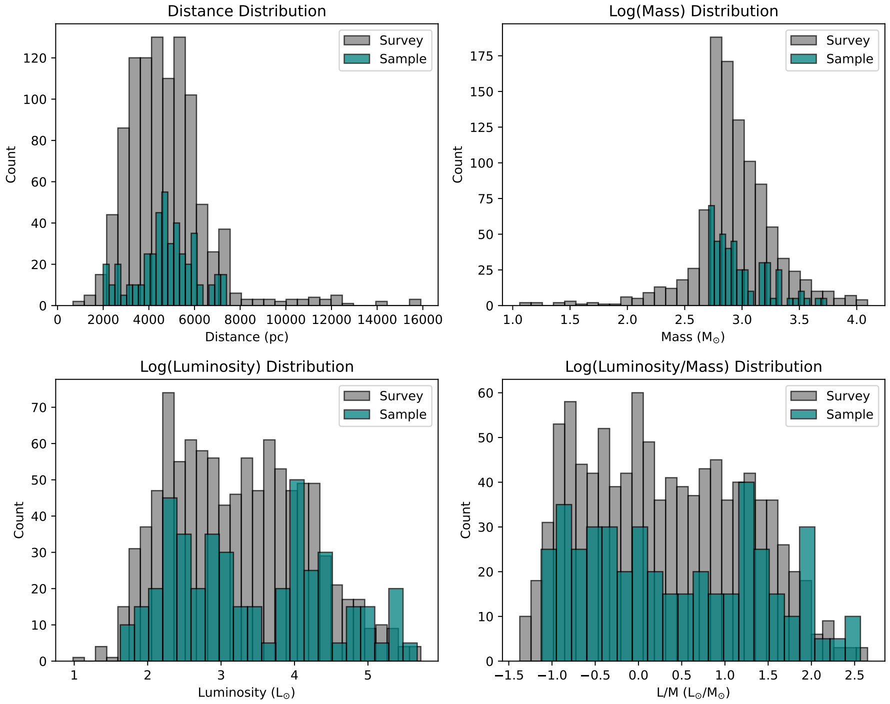

Figure A.1: Histograms comparing the all regions in the ALMAGAL survey vs the ones chosen for this sample for distance, mass, luminosity, and L/M.

A.2 Core mass figures

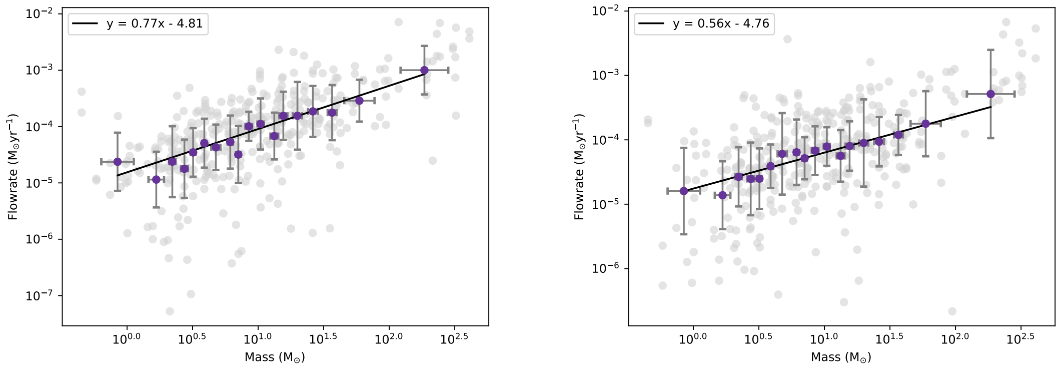

(a) Only inner flow rates.

(b) Only outer flow rates.

Figure A.2: Flow rate vs. core mass relation for only the flow rates closer to the core (panel (a)), and only the flow rates further from the core (panel (b)).

A.3 Source and core parameters

Table A.1: Table of source parameters (10 row preview).

ALMAGAL Name	ID	G_{lon} (°)	G_{lat} (°)	V_{lsr} ($\mathrm{km\,s^{-1}}$)	Dist (pc)	Mass ($\mathrm{M_{\odot}}$)	Lum ($\mathrm{L_{\odot}}$)	Temp (K)	Classification
AG022.5316-0.1923	99331	22.533	-0.191	74.8	4470	1503	217	20	Quiescent
AG024.0046+0.0397	107003	24.006	0.040	113.1	5960	2025	691	20	Quiescent
AG024.0147+0.0487	107032	24.014	0.048	111.5	5890	3263	2155	20	Quiescent
AG024.8555+0.0051	111167	24.855	0.005	108.7	5780	806	231	20	Quiescent
AG026.6280-0.0647	119601	26.628	-0.064	103.2	5570	620	279	20	Quiescent
AG027.7975+0.1501	124229	27.798	0.150	81.7	4610	927	108	20	Quiescent
AG028.3550+0.0728	126186	28.354	0.070	81.4	4590	1126	179	20	Quiescent
AG030.2747-0.2311	135558	30.274	-0.231	103.6	5800	1238	243	20	Quiescent
AG031.0225-0.1113	139543	31.022	-0.111	77.1	4400	782	114	20	Quiescent
AG308.8759+0.1730	717276	308.876	0.174	-49.8	4110	557	80	20	Quiescent

Table A.2: Table of core parameters (10 row preview).

ID	x Offset (″)	y Offset (″)	Flow rate (L_{outer}) (10^{-4} M$_\odot$ yr^{-1})	Flow rate (L_{inner}) (10^{-4} M$_\odot$ yr^{-1})	Flow rate (R_{inner}) (10^{-4} M$_\odot$ yr^{-1})	Flow rate (R_{outer}) (10^{-4} M$_\odot$ yr^{-1})	Mass (M$_\odot$)
99331	2.73	2.52	0.21	0.49	0.02	0.02	17.8
107003	2.00	3.99	0.08	0.004	0.23	0.19	6.3
107032	0.95	-6.18	1.22	10.27	0.97	0.38	37.6
111167	1.63	-2.40	2.84	0.54	0.50	0.003	14.1
119601	-0.38	2.00	4.87	0.31	0.40	0.89	6.3
124229	1.05	0.00	0.90	0.80	1.57	0.44	6.6
126186	4.83	-6.72	0.35	0.38	0.06	0.15	2.7
126186	5.04	-3.36	0.20	0.27	0.08	0.12	3.9
126186	-3.78	-0.21	0.81	2.46	0.71	1.13	17.8
126186	0.42	3.57	2.23	2.65	0.13	0.08	8.4

B

Additional material to Chapter 4

B.1 Scale figures

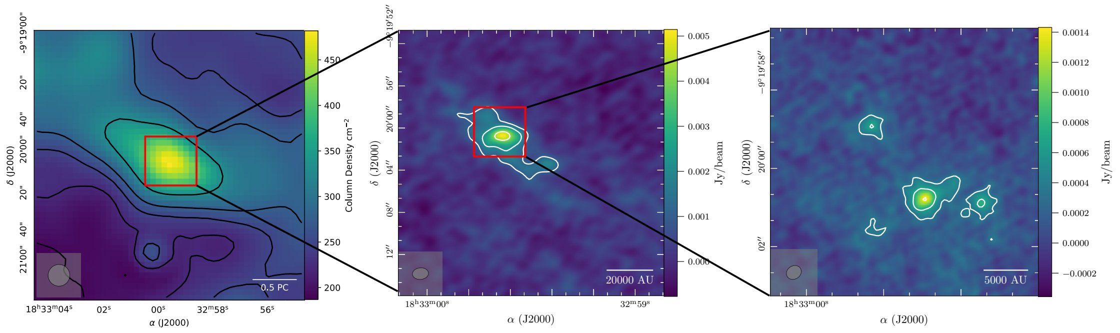

(a) AG022.5-0.19

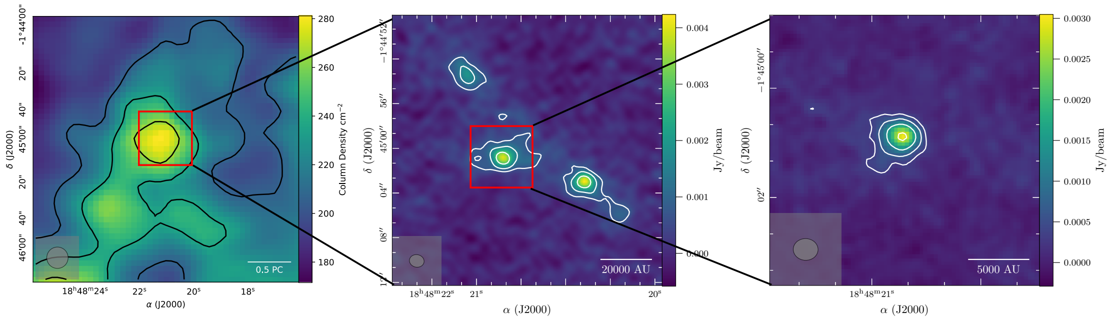

(b) AG031.0-0.11

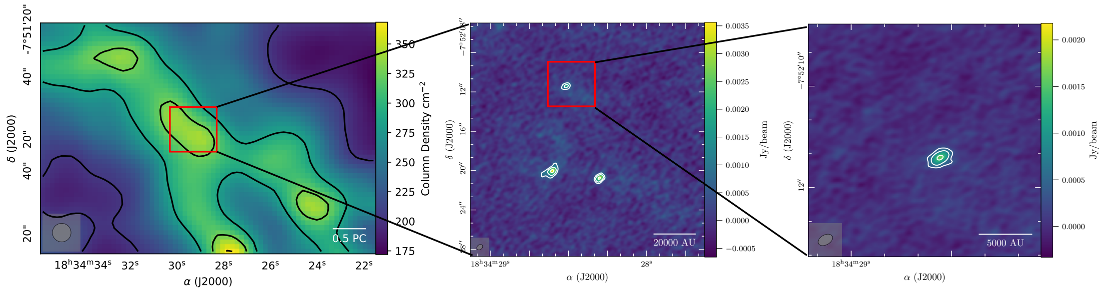

(c) AG023.9+0.15

Figure B.1: Three panel continuum figures showing the different data scales. *Left:* Reprojected Marsh et al. (2017) column density maps to match the IRAM 30m data scales at 12″ spatial resolution. Contours overlaid in black, with 0.5 pc scale bar. *Middle:* Zoom in of the large scale clump to reveal the ALMAGAL intermediate scale cores, continuum contours overlaid in white, with 20 000 au scale bar. *Right:* Zoom in of one of the intermediate scale cores to reveal ALMAGAL small scale cores, continuum contours overlaid in white with a 5000 au scale bar.

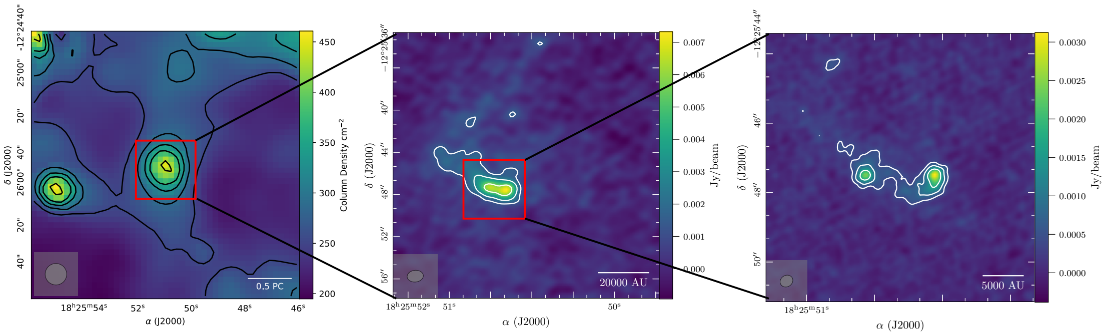

(a) AG018.9-0.07

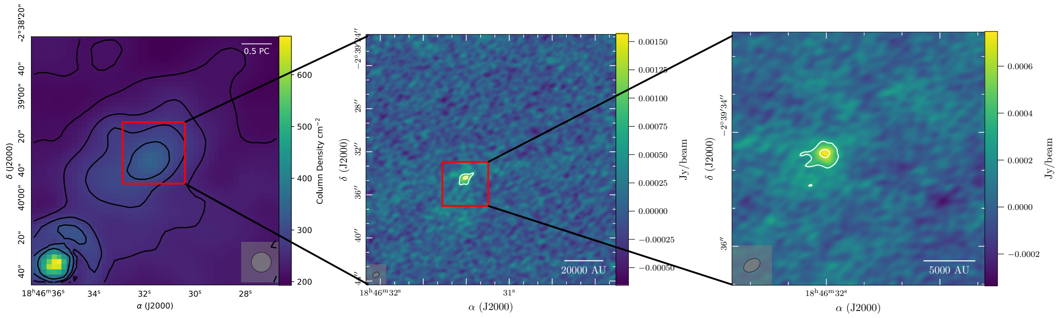

(b) AG030.0-0.12

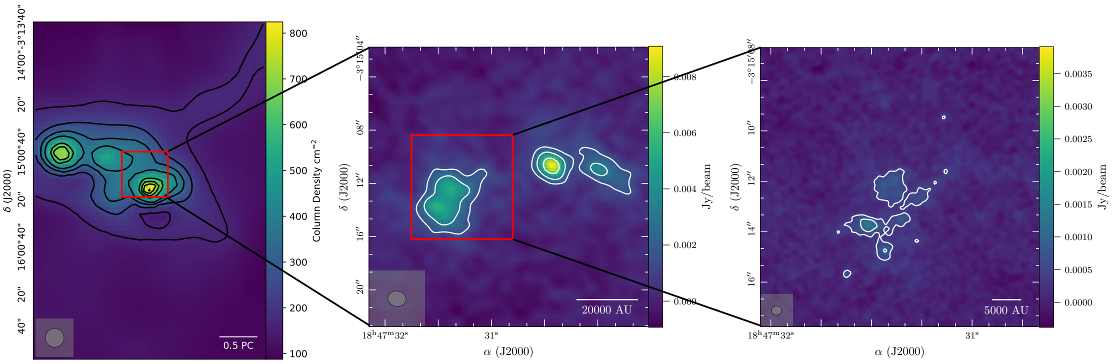

(c) AG029.5-0.61

Figure B.2: Three panel continuum figures showing the different data scales. *Left:* Reprojected Marsh et al. (2017) column density maps to match the IRAM 30m data scales at 12″ spatial resolution. Contours overlaid in black, with 0.5 pc scale bar. *Middle:* Zoom in of the large scale clump to reveal the ALMAGAL intermediate scale cores, continuum contours overlaid in white, with 20 000 au scale bar. *Right:* Zoom in of one of the intermediate scale cores to reveal ALMAGAL small scale cores, continuum contours overlaid in white with a 5000 au scale bar.

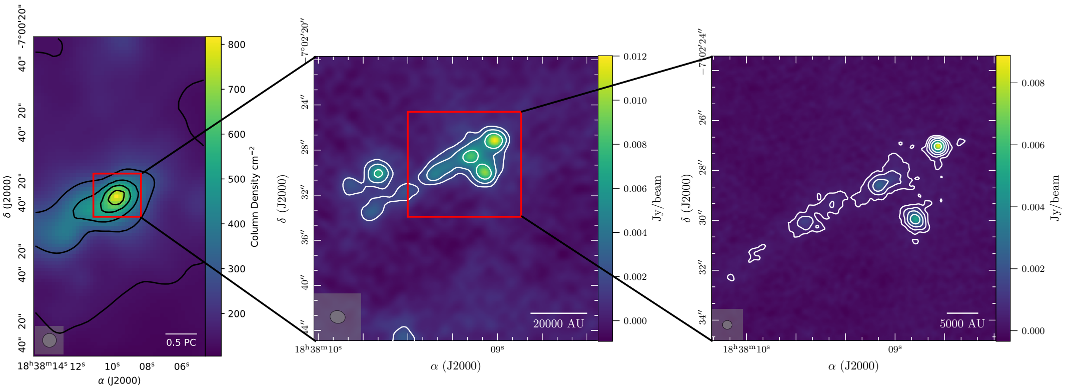

(a) AG025.1-0.27

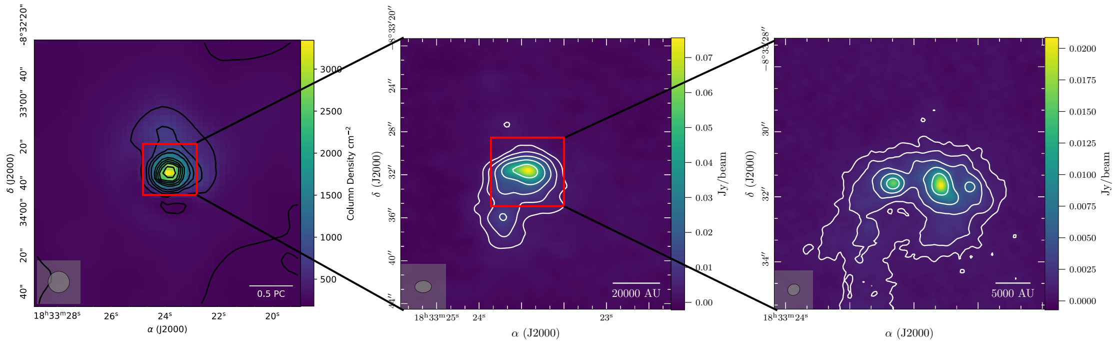

(b) AG023.2+0.07

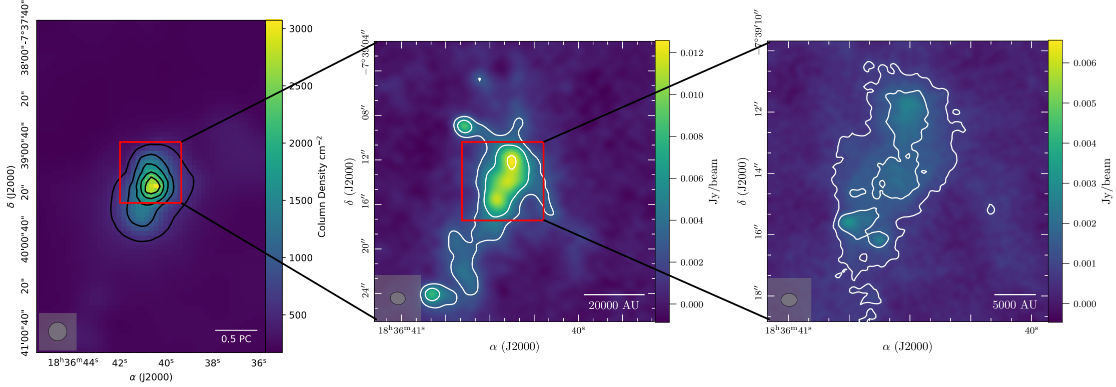

(c) AG024.4-0.22

Figure B.3: Three panel continuum figures showing the different data scales. *Left:* Reprojected Marsh et al. (2017) column density maps to match the IRAM 30m data scales at 12″ spatial resolution. Contours overlaid in black, with 0.5 pc scale bar. *Middle:* Zoom in of the large scale clump to reveal the ALMAGAL intermediate scale cores, continuum contours overlaid in white, with 20 000 au scale bar. *Right:* Zoom in of one of the intermediate scale cores to reveal ALMAGAL small scale cores, continuum contours overlaid in white with a 5000 au scale bar.

B.2 IRAM 30m 0th moment maps

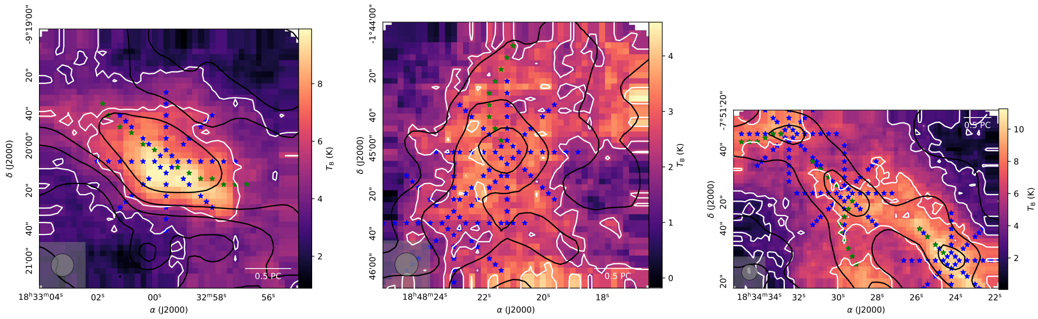

(a) AG022.5-0.19 **(b)** AG031.0-0.11 **(c)** AG023.9+0.15

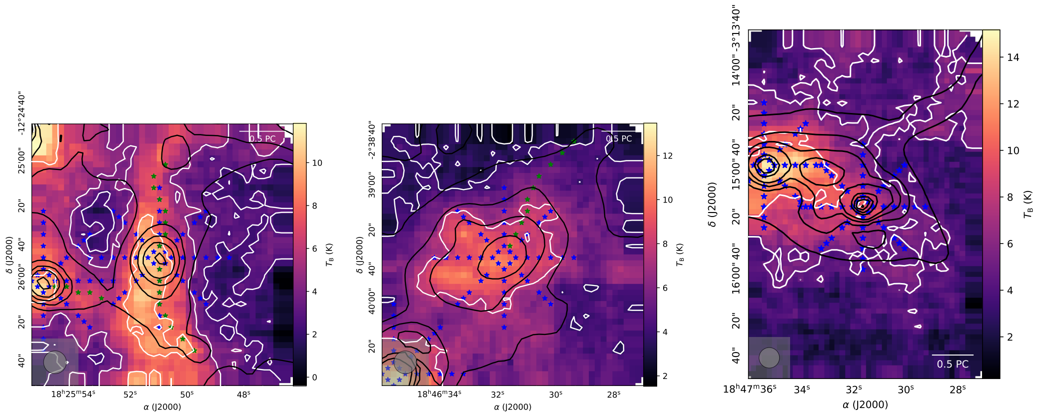

(d) AG018.9-0.07 **(e)** AG030.0-0.12 **(f)** AG029.5-0.61

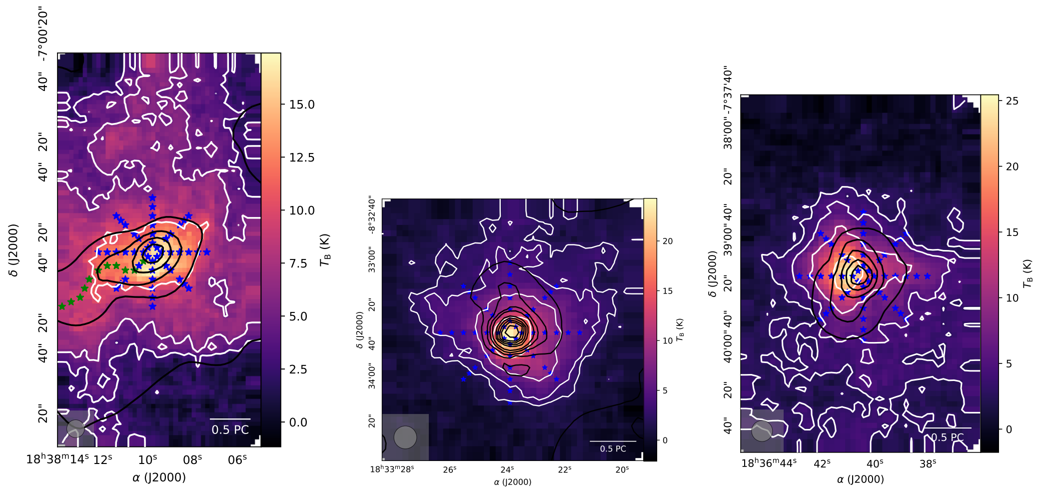

(g) AG025.1-0.27 **(h)** AG023.2+0.07 **(i)** AG024.4-0.22

Figure B.4: IRAM 30m $C^{18}O$ (2-1) 0th moment maps for each region. Blue stars show polar around the clumps flow rate positions and green stars show along the filament flow rate positions.

B.3 IRAM 30m 1st moment maps

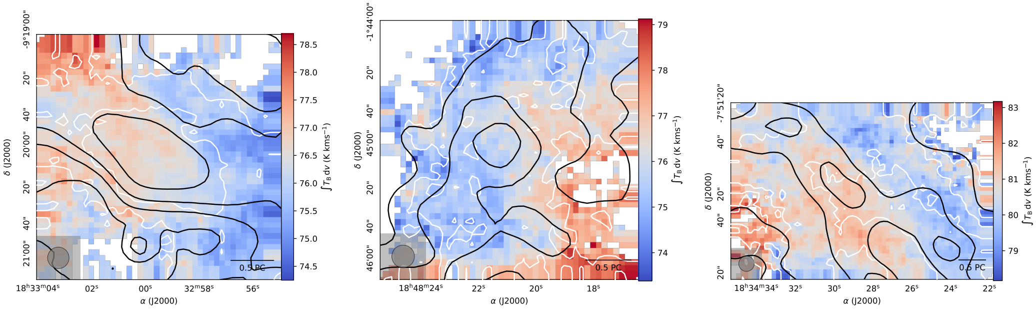

(a) AG022.5-0.19 **(b)** AG031.0-0.11 **(c)** AG023.9+0.15

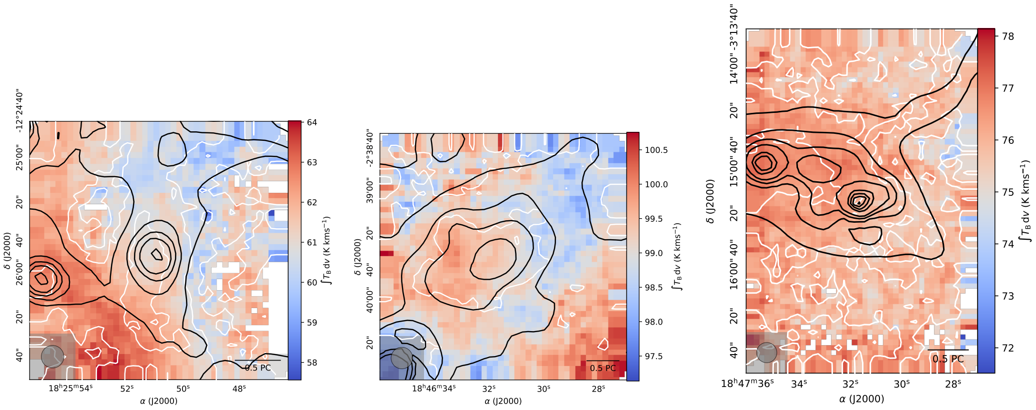

(d) AG018.9-0.07 **(e)** AG030.0-0.12 **(f)** AG029.5-0.61

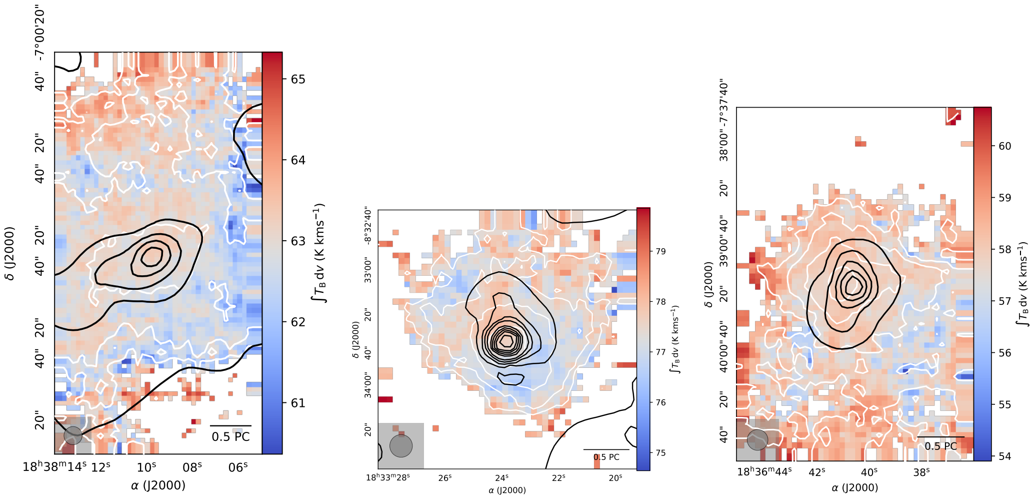

(g) AG025.1-0.27 **(h)** AG023.2+0.07 **(i)** AG024.4-0.22

Figure B.5: IRAM 30m C^{18}O (2-1) 1st moment maps for each region.

List of Figures

1.1 The full area of the Galactic plane visible from the southern hemisphere 2
1.2 A schematic of the evolution from quiescent to HII region 6
1.3 Quiescent vs. protostellar visual differences 7
1.4 Protostellar, YSO and HII region examples though 8, 24 and 70 µm wavelengths 8
1.5 A view of the IRAM 30m 10
1.6 A view of the ALMA array 12
1.7 Milky-Way type galaxy simulation 17

2.1 ALMAGAL sub-sample source distribution 25
2.2 Sub-sample evolutionary stage distributions 27
2.3 Astrodendro identification image for AG348.5792-0.9197 28
2.4 AG348.5792-0.9197 0th moment in SO 29
2.5 Position velocity cut 31
2.6 Dust and gas temperature comparison 33
2.7 Theoretical flow rate spread due to unknown inclination 36
2.8 Evolutionary stage flow rate histograms 39
2.9 Distance flow rate histograms 40
2.10 Distance variation flow rate histogram 40
2.11 Flow rate vs. core mass relationship 41

3.1 Simulated galaxy overview 47
3.2 Active and quiet region density projections 49
3.3 Active and quiet region `FilFinder` velocity-coded skeletons 50
3.4 Along, onto and polar points demonstration 51
3.5 Active cube flow rates statistics 54
3.6 Quiet cube flow rate statistics 54
3.7 Flow rate vs. distance relation for the active cube 55
3.8 Flow rate vs. distance relation for the quiet cube 56
3.9 Active cube polar flow rate plots 57
3.10 Quiet cube polar flow rate plots 57
3.11 Inclinations distance vs. flow rate relationship 58

3.12 Simulated flow rates along the filaments in the active cube 61
3.13 Distributions of all the perpendicular flow rates measured at 0, $\pi/2$, π, and $3\pi/2$ for the 3D filament spines in the active region 62
3.14 3D projection of the filament spines for filaments 1 and 3 in the active cube 63

4.1 Three panel continuum figure showing the different data scales 71
4.2 Three panel figure showing structure identification at each scale . . . 76
4.3 Two panel figure showing velocity analysis at different scales 78
4.4 Relationship between flow rate and distance for regions AG028.3+0.06 and AG025.1-0.27 80
4.5 Polar plot for AG028.3+0.06 81
4.6 Polar plot for AG025.1-0.27 81
4.7 Flow rate distributions for the three spatial scales 83
4.8 Violin plot for the three spatial scales 84
4.9 Flow rate distributions for each evolutionary stage, for each spatial scale 85

A.1 Sub-sample parameter histograms 98
A.2 Flow rate vs. core mass distance variations 98

B.1 Three panel scales figures 102
B.2 Three panel scales figures 103
B.3 Three panel scales figures 104
B.4 IRAM 30m C^{18}O (2-1) 0th moment maps 105
B.5 IRAM 30m C^{18}O (2-1) 1st moment maps 106

List of Tables

1.1 Protostar tracers - mm/submm 14

2.1 Observational parameters 25
2.2 Final sample distribution 31
2.3 p-values from the KS and Mann-Whitney U tests. 37

3.1 `FilFinderPPV` parameters 51

4.1 10 Regions parameters 73
4.2 Median flow rate values 79

A.1 Table of source parameters (10 row preview). 99
A.2 Table of core parameters (10 row preview). 100

Publication list

The following published paper is part of this thesis (Chapter 2):

- **M. R. A. Wells**, H. Beuther S. Molinari, P. Schilke, C. Battersby, et al. *Dynamical accretion flows: ALMAGAL: Flows along filamentary structures in high-mass star-forming clusters.* A&A 690:A185 October 2024 [Citations: 11].

The following paper is part of this thesis (Chapter 3) and is currently under review:

- **M. R. A. Wells**, R. Pillsworth, H. Beuther, R. E. Pudritz and E. W. Koch. *From theory to observation: understanding filamentary flows in high-mass star-forming clusters.* A&A [Submitted]

The following paper is part of this thesis (Chapter 4) and is in preparation:

- **M. R. A. Wells**, H. Beuther S. Molinari, P. Schilke, C. Battersby et al. *Hierarchical Flows from Clouds to Cores. Characterising the Flow from pc to 1000 au Scales with ALMAGAL + IRAM 30m.* [In prep.]

The following published paper is **not** part of this thesis:

- **M. R. A. Wells**, J. S. Urquhart et al., *ATLASGAL - star forming efficiencies and the Galactic star formation rate.* MNRAS, 516, 4245-4255. November 2022 [Citations: 7]

The following co-authored publications are all **not** part of this thesis:

- C. Gieser, H. Beuther, D. Seminov, A. Ahmadi, Th. Henning, **M. R. A. Wells**. *Physical and chemical complexity in high-mass star-forming regions with ALMA. I. Overview and evolutionary trends of physical properties.* A&A, 674:A160. June 2023. [Citations: 5]
- J. S. Urquhart, **M. R. A. Wells** et al., *ATLASGAL - evolutionary trends in high-mass star formation.* MNRAS, 510,3,2289-2407. March 2022. [Citations: 48]

- J. S. Urquhart, C. Figura, J. R. Cross, **M. R. A. Wells** et al., *SEDIGISM-ATLASGAL: dense gas fraction and star formation efficiency across the Galactic disc.* MNRAS, 500, 3050-3063. January 2021. [Citations: 37]
- S. Molinari et al. *ALMAGAL I. The ALMA evolutionary study of high mass protocluster formation in the Galaxy: presentation of the survey and early results.* A&A [Accepted.]
- Á. Sánchez-Monge et al. *ALMAGAL II. The ALMA evolutionary study of high-mass protocluster formation in the Galaxy.* A&A [Accepted.]
- A. Colletta et al. *ALMAGAL III. Compact source catalog: fragmentation statistics and physical evolution of the core population.* A&A [Accepted.]
- C. Mininni et al. *ALMAGAL IV. Morphological comparison of molecular and thermal dust emission using the histogram of oriented gradients (HOG) method.* A&A [Accepted.]
- J. Syed et al. *Cold atomic gas identified by HI self-absorption - Cold atomic clouds in the inner Galactic plane.* [In prep.]
- K. Schwarz et al. *Evidence of Enhanced Ionization in Protostellar Envelopes.* [In prep.]

Bibliography

Agertz, O., Teyssier, R., & Moore, B. 2011, MNRAS, 410, 1391

Alves, J., Zucker, C., & Goodman, A. 2020, Nature, 578

André, P., Di Francesco, J., Ward-Thompson, D., et al. 2014, in Protostars and Planets VI, ed. H. Beuther, R. S. Klessen, C. P. Dullemond, & T. Henning, 27–51

André, P., Men'shchikov, A., Bontemps, S., et al. 2010, A&A, 518, L102

Arce, H. G., Shepherd, D., Gueth, F., et al. 2007, in Protostars and Planets V, ed. B. Reipurth, D. Jewitt, & K. Keil, 245

Battersby, C., Keto, E., Walker, D., et al. 2020, ApJS, 249, 35

Beltrán, M. T. & de Wit, W. J. 2016, A&A Rev., 24, 6

Beuther, H., Kuiper, R., & Tafalla, M. 2025, arXiv e-prints, arXiv:2501.16866

Beuther, H., Mottram, J. C., Ahmadi, A., et al. 2018, A&A, 617, A100

Beuther, H., Thorwirth, S., Zhang, Q., et al. 2005, ApJ, 627, 834

Beuther, H., Wang, Y., Soler, J., et al. 2020, A&A, 638, A44

Beuther, H., Wyrowski, F., Menten, K. M., et al. 2022, A&A, 665, A63

Beuther, H., Zhang, Q., Bergin, E. A., et al. 2007, A&A, 468, 1045

Bonnell, I. A., Bate, M. R., & Vine, S. G. 2003, MNRAS, 343, 413

Bonnell, I. A., Bate, M. R., & Zinnecker, H. 1998, MNRAS, 298, 93

Bonnell, I. A., Clarke, C. J., Bate, M. R., & Pringle, J. E. 2001, MNRAS, 324, 573

Bonnell, I. A., Larson, R. B., & Zinnecker, H. 2007, in Protostars and Planets V, ed. B. Reipurth, D. Jewitt, & K. Keil, 149

Bosco, F., Beuther, H., Ahmadi, A., et al. 2019, A&A, 629, A10

Bressert, E., Bastian, N., Gutermuth, R., et al. 2010, MNRAS, 409, L54

Carey, S. J., Noriega-Crespo, A., Mizuno, D. R., et al. 2009, PASP, 121, 76

Carroll-Nellenback, J. J., Frank, A., & Heitsch, F. 2014, ApJ, 790, 37

CASA Team, Bean, B., Bhatnagar, S., et al. 2022, PASP, 134, 114501

Caselli, P., Walmsley, C. M., Terzieva, R., & Herbst, E. 1998, ApJ, 499, 234

Caselli, P., Walmsley, C. M., Zucconi, A., et al. 2002, ApJ, 565, 344

Cesaroni, R., Hofner, P., Walmsley, C. M., & Churchwell, E. 1998, A&A, 331, 709

Chakravarti, I. M., Laha, R. G., & Roy, J. 1967, (No Title)

Chira, R. A., Kainulainen, J., Ibáñez-Mejía, J. C., Henning, T., & Mac Low, M. M. 2018, A&A, 610, A62

Churchwell, E., Babler, B. L., Meade, M. R., et al. 2009, PASP, 121, 213

Clark, P. C. & Whitworth, A. P. 2021, MNRAS, 500, 1697

Clark, S. E., Peek, J. E. G., & Putman, M. E. 2014, ApJ, 789, 82

Clarke, S. D., Whitworth, A. P., Duarte-Cabral, A., & Hubber, D. A. 2017, MNRAS, 468, 2489

Dobbs, C. L. & Pringle, J. E. 2013, MNRAS, 432, 653

Draine, B. T. 2003, ApJ, 598, 1017

Draine, B. T. 2011, Physics of the Interstellar and Intergalactic Medium

Duan, X. & Guo, F. 2024, The Astrophysical Journal

Duarte-Cabral, A., Bontemps, S., Motte, F., et al. 2013, A&A, 558, A125

Elia, D., Merello, M., Molinari, S., et al. 2021, MNRAS, 504, 2742

Elia, D., Molinari, S., Schisano, E., et al. 2017, MNRAS, 471, 100

Federrath, C. 2016, MNRAS, 457, 375

Ferrière, K. M. 2001, Reviews of Modern Physics, 73, 1031

Fiege, J. D. & Pudritz, R. E. 2000, MNRAS, 311, 105

Frank, A., Ray, T. P., Cabrit, S., et al. 2014, in Protostars and Planets VI, ed. H. Beuther, R. S. Klessen, C. P. Dullemond, & T. Henning, 451–474

Froebrich, D. & Rowles, J. 2010, MNRAS, 406, 1350

García, P., Bronfman, L., Nyman, L.-Å., Dame, T. M., & Luna, A. 2014, ApJS, 212, 2

Gerner, T., Beuther, H., Semenov, D., et al. 2014, A&A, 563, A97

Gerner, T., Shirley, Y. L., Beuther, H., et al. 2015, A&A, 579, A80

Gieser, C., Beuther, H., Semenov, D., et al. 2021, A&A, 648, A66

Gieser, C., Beuther, H., Semenov, D., et al. 2022, A&A, 657, A3

Goldsmith, P. F., Heyer, M., Narayanan, G., et al. 2008, ApJ, 680, 428

Gómez, G. C. & Vázquez-Semadeni, E. 2014, ApJ, 791, 124

Grudić, M. Y., Kruijssen, J. M. D., Faucher-Giguère, C.-A., et al. 2021, MNRAS, 506, 3239

Gutermuth, R. A. & Heyer, M. 2015, AJ, 149, 64

Hacar, A., Clark, S. E., Heitsch, F., et al. 2023, in Astronomical Society of the Pacific Conference Series, Vol. 534, Protostars and Planets VII, ed. S. Inutsuka, Y. Aikawa, T. Muto, K. Tomida, & M. Tamura, 153

Hacar, A., Konietzka, R., Seifried, D., et al. 2025, A&A, 694, A69

Hacar, A., Socci, A., Bonanomi, F., et al. 2024, A&A, 687, A140

Hacar, A., Tafalla, M., Forbrich, J., et al. 2018, A&A, 610, A77

Haid, S., Walch, S., Seifried, D., et al. 2019, MNRAS, 482, 4062

Hartmann, L., Ballesteros-Paredes, J., & Heitsch, F. 2012, MNRAS, 420, 1457

Heitsch, F., Hartmann, L. W., & Burkert, A. 2008, ApJ, 683, 786

Hennebelle, P., Commerçon, B., Joos, M., et al. 2011, A&A, 528, A72

Henshaw, J. D., Caselli, P., Fontani, F., Jiménez-Serra, I., & Tan, J. C. 2014, MNRAS, 440, 2860

Henshaw, J. D., Ginsburg, A., Haworth, T. J., et al. 2019, MNRAS, 485, 2457

Hildebrand, R. H. 1983, QJRAS, 24, 267

Hillel, S. & Soker, N. 2020, The Astrophysical Journal, 896, 104

Ho, P. T. P. & Townes, C. H. 1983, ARA&A, 21, 239

Hoare, M. G., Lumsden, S. L., Oudmaijer, R. D., et al. 2005, in Massive Star Birth: A Crossroads of Astrophysics, ed. R. Cesaroni, M. Felli, E. Churchwell, & M. Walmsley, Vol. 227, 370–375

Högbom, J. A. 1974, A&AS, 15, 417

Izumi, N., Sanhueza, P., Koch, P. M., et al. 2024, ApJ, 963, 163

Jackson, J. M., Finn, S. C., Chambers, E. T., Rathborne, J. M., & Simon, R. 2010, ApJ, 719, L185

Jenkins, E. B. 2013, ApJ, 764, 25

Kahn, F. D. 1974, A&A, 37, 149

Kim, J.-h., Agertz, O., Teyssier, R., et al. 2016, ApJ, 833, 202

Kirk, H., Myers, P. C., Bourke, T. L., et al. 2013, ApJ, 766, 115

Klessen, R. S., Burkert, A., & Bate, M. R. 1998, ApJ, 501, L205

Klessen, R. S. & Glover, S. C. O. 2016, Saas-Fee Advanced Course, 43, 85

Klessen, R. S., Heitsch, F., & Mac Low, M.-M. 2000, ApJ, 535, 887

Koch, E. W. & Rosolowsky, E. W. 2015, MNRAS, 452, 3435

Krieger, N., Ott, J., Beuther, H., et al. 2017, ApJ, 850, 77

Krumholz, M. R. 2014, Phys. Rep., 539, 49

Krumholz, M. R. & Federrath, C. 2019, Frontiers in Astronomy and Space Sciences, 6, 7

Krumholz, M. R., Klein, R. I., & McKee, C. F. 2007, ApJ, 656, 959

Krumholz, M. R., Klein, R. I., McKee, C. F., Offner, S. S. R., & Cunningham, A. J. 2009, Science, 323, 754

Kuiper, R. & Hosokawa, T. 2018, A&A, 616, A101

Kuiper, R., Klahr, H., Beuther, H., & Henning, T. 2010, ApJ, 722, 1556

Kuiper, R., Klahr, H., Beuther, H., & Henning, T. 2011, ApJ, 732, 20

Kumar, M. S. N., Palmeirim, P., Arzoumanian, D., & Inutsuka, S. I. 2020, A&A, 642, A87

Lada, C. J. & Lada, E. A. 2003, Annual Review of Astronomy and Astrophysics, 41, 57–115

Li, P. S. & Klein, R. I. 2019, MNRAS, 485, 4509

Liu, H. B., Galván-Madrid, R., Jiménez-Serra, I., et al. 2015, ApJ, 804, 37

Liu, T., Wu, Y., & Zhang, H. 2013, ApJ, 775, L2

López-Sepulcre, A., Cesaroni, R., & Walmsley, C. M. 2010, A&A, 517, A66

Lumsden, S. L., Hoare, M. G., Urquhart, J. S., et al. 2013, ApJS, 208, 11

Mac Low, M.-M. & Klessen, R. S. 2004, Reviews of Modern Physics, 76, 125

Mangum, J. G. & Wootten, A. 1993, ApJS, 89, 123

Marsh, K. A., Whitworth, A. P., Lomax, O., et al. 2017, MNRAS, 471, 2730

McKee, C. F. & Tan, J. C. 2003, ApJ, 585, 850

McKnight, P. E. & Najab, J. 2010, The Corsini encyclopedia of psychology, 1

Mège, P., Russeil, D., Zavagno, A., et al. 2021, A&A, 646, A74

Mills, E. A. C. & Morris, M. R. 2013, ApJ, 772, 105

Molinari, S., Baldeschi, A., Robitaille, T. P., et al. 2019, MNRAS, 486, 4508

Molinari, S., Merello, M., Elia, D., et al. 2016, ApJ, 826, L8

Molinari, S., Schilke, P., Battersby, C., et al. 2025, arXiv e-prints, arXiv:2503.05555

Molinari, S., Swinyard, B., Bally, J., et al. 2010a, A&A, 518, L100

Molinari, S., Swinyard, B., Bally, J., et al. 2010b, PASP, 122, 314

Motte, F., Bontemps, S., & Louvet, F. 2018, ARA&A, 56, 41

Motte, F., Bontemps, S., & Louvet, F. 2018, Annual Review of Astronomy and Astrophysics, 56, 41–82

Motte, F., Bontemps, S., Schilke, P., et al. 2007, A&A, 476, 1243

Mullens, E., Zucker, C., Murray, C. E., & Smith, R. 2024, ApJ, 966, 127

Myers, P. C. 2009, ApJ, 700, 1609

Nava, L., Recchia, S., Gabici, S., et al. 2019, MNRAS, 484, 2684

Nunez-Iglesias, J., Blanch, A., Looker, O., Dixon, M., & Tilley, L. 2018, PeerJ, 6, 4312

Offner, S. S. R., Clark, P. C., Hennebelle, P., et al. 2014, in Protostars and Planets VI, ed. H. Beuther, R. S. Klessen, C. P. Dullemond, & T. Henning, 53–75

Olguin, F. A., Sanhueza, P., Chen, H.-R. V., et al. 2023, ApJ, 959, L31

Olivares, V., Salome, P., Combes, F., et al. 2019, A&A, 631, A22

Ossenkopf, V. & Henning, T. 1994, A&A, 291, 943

Padoan, P., Juvela, M., Goodman, A. A., & Nordlund, Å. 2001, ApJ, 553, 227

Padoan, P., Pan, L., Juvela, M., Haugbølle, T., & Nordlund, Å. 2020a, ApJ, 900, 82

Padoan, P., Pan, L., Juvela, M., Haugbølle, T., & Nordlund, Å. 2020b, ApJ, 900, 82

Padovani, M., Galli, D., & Glassgold, A. E. 2009, A&A, 501, 619

Peretto, N., Fuller, G. A., Duarte-Cabral, A., et al. 2013, A&A, 555, A112

Pillsworth, R. & Pudritz, R. E. 2024, MNRAS, 528, 209

Pillsworth, R., Roscoe, E., Pudritz, R. E., & Koch, E. W. 2025, arXiv e-prints, arXiv:2504.01099

Pineda, J. E., Arzoumanian, D., Andre, P., et al. 2023, in Astronomical Society of the Pacific Conference Series, Vol. 534, Protostars and Planets VII, ed. S. Inutsuka, Y. Aikawa, T. Muto, K. Tomida, & M. Tamura, 233

Pon, A., Johnstone, D., & Heitsch, F. 2011, ApJ, 740, 88

Ragan, S. E., Henning, T., Tackenberg, J., et al. 2014, A&A, 568, A73

Rathborne, J. M., Jackson, J. M., & Simon, R. 2006, ApJ, 641, 389

Redaelli, E., Bovino, S., Sanhueza, P., et al. 2022, ApJ, 936, 169

Russell, H. R., McDonald, M., McNamara, B. R., et al. 2017, The Astrophysical Journal, 836, 130

Salpeter, E. E. 1955, ApJ, 121, 161

Sánchez-Monge, Á., Brogan, C. L., Hunter, T. R., et al. 2025, arXiv e-prints, arXiv:2503.05559

Sanhueza, P., Girart, J. M., Padovani, M., et al. 2021, ApJ, 915, L10

Scalo, J. M. 1985, in Protostars and Planets II, ed. D. C. Black & M. S. Matthews, 201–296

Schisano, E., Molinari, S., Elia, D., et al. 2020, MNRAS, 492, 5420

Schneider, N., Csengeri, T., Bontemps, S., et al. 2010, A&A, 520, A49

Schuller, F., Menten, K. M., Contreras, Y., et al. 2009, A&A, 504, 415

Seifried, D., Banerjee, R., Klessen, R. S., Duffin, D., & Pudritz, R. E. 2011, MNRAS, 417, 1054

Seifried, D. & Walch, S. 2015, MNRAS, 452, 2410

Shirley, Y. L. 2015, PASP, 127, 299

Smith, R. J., Longmore, S., & Bonnell, I. 2009, MNRAS, 400, 1775

Stahler, S. W. & Palla, F. 2004, The Formation of Stars

Svoboda, B. E., Shirley, Y. L., Traficante, A., et al. 2019, ApJ, 886, 36

Syed, J., Soler, J. D., Beuther, H., et al. 2022, A&A, 657, A1

Tackenberg, J., Beuther, H., Henning, T., et al. 2014, A&A, 565, A101

Tan, J. C., Beltrán, M. T., Caselli, P., et al. 2014, 149

Teyssier, R. 2002, A&A, 385, 337

Thomasson, B., Joncour, I., Moraux, E., et al. 2022, A&A, 665, A119

Traficante, A., Fuller, G. A., Billot, N., et al. 2017, MNRAS, 470, 3882

Traficante, A., Jones, B. M., Avison, A., et al. 2023, MNRAS, 520, 2306

Turk, M. J., Smith, B. D., Oishi, J. S., et al. 2011, ApJS, 192, 9

Tychoniec, Ł., van Dishoeck, E. F., van't Hoff, M. L. R., et al. 2021, A&A, 655, A65

Urquhart, J. S., Busfield, A. L., Hoare, M. G., et al. 2007, A&A, 474, 891

Urquhart, J. S., König, C., Colombo, D., et al. 2024, MNRAS, 528, 4746

Urquhart, J. S., König, C., Giannetti, A., et al. 2018, MNRAS, 473, 1059

Urquhart, J. S., Moore, T. J. T., Csengeri, T., et al. 2014, MNRAS, 443, 1555

Urquhart, J. S., Wells, M. R. A., Pillai, T., et al. 2022, MNRAS, 510, 3389

van der Tak, F. F. S., Black, J. H., Schöier, F. L., Jansen, D. J., & van Dishoeck, E. F. 2007, A&A, 468, 627

van Dishoeck, E. F., Kristensen, L. E., Mottram, J. C., et al. 2021, A&A, 648, A24

van Gelder, M. L., Tabone, B., van Dishoeck, E. F., & Godard, B. 2021, A&A, 653, A159

Vasyunina, T., Linz, H., Henning, T., et al. 2011, A&A, 527, A88

Vázquez-Semadeni, E., Gómez, G. C., Jappsen, A. K., Ballesteros-Paredes, J., & Klessen, R. S. 2009, ApJ, 707, 1023

Vázquez-Semadeni, E., Palau, A., Ballesteros-Paredes, J., Gómez, G. C., & Zamora-Avilés, M. 2019, MNRAS, 490, 3061

Wells, M. R. A., Beuther, H., Molinari, S., et al. 2024, A&A, 690, A185

Wells, M. R. A., Urquhart, J. S., Moore, T. J. T., et al. 2022, MNRAS, 516, 4245

Widmann, F., Beuther, H., Schilke, P., & Stanke, T. 2016, A&A, 589, A29

Williams, J. P., Blitz, L., & McKee, C. F. 2000, in Protostars and Planets IV, ed. V. Mannings, A. P. Boss, & S. S. Russell, 97

Wolfire, M. G. & Cassinelli, J. P. 1987, ApJ, 319, 850

Wolfire, M. G., McKee, C. F., Hollenbach, D., & Tielens, A. G. G. M. 2003, ApJ, 587, 278
Xu, X., Li, D., Dai, Y. S., Goldsmith, P. F., & Fuller, G. A. 2020, ApJ, 898, 122
Xu, X., Wang, K., Gou, Q., et al. 2024, MNRAS, 535, 940
Yorke, H. W. & Kruegel, E. 1977, A&A, 54, 183
Yorke, H. W. & Sonnhalter, C. 2002, ApJ, 569, 846
Zhang, Q., Qiu, K., Girart, J. M., et al. 2014, ApJ, 792, 116
Zhang, Q., Wang, K., Lu, X., & Jiménez-Serra, I. 2015, ApJ, 804, 141
Zhang, S., Cyganowski, C. J., Henshaw, J. D., et al. 2024, MNRAS, 533, 1075
Zhao, B., Pudritz, R. E., Pillsworth, R., Robinson, H., & Wadsley, J. 2024, ApJ, 974, 240
Zhou, J. W., Dib, S., & Davis, T. A. 2024, MNRAS, 534, 683
Zinnecker, H. 1984, MNRAS, 210, 43
Zinnecker, H. & Yorke, H. W. 2007, ARA&A, 45, 481
Zucker, C., Battersby, C., & Goodman, A. 2015, ApJ, 815, 23
Zucker, C. & Chen, H. H.-H. 2018, ApJ, 864, 152
Zucker, C., Goodman, A., Alves, J., et al. 2021, ApJ, 919, 35

Acknowledgments

I have learnt so much in these past four years, from the people I call my best friends, to people who are no longer in my life, there are too many people who contributed to who I am today, how I got here, and therefore the production of this work. Younger me would think I am super cool and that means I've done things right. (yes Keila, current me thinks I'm cool too). This work is a true labour of love, hate, pain, frustration, dedication, discipline and so much more, but I would not have gotten through it without my supervisor. Henrik, I think the research we have done (and will continue to do) together is the most fascinating thing in the world and I can't thank you enough for having excellent choice in PhD students, and people in general because our group is the best. I hope you understand how amazing these four years have been because of you, and especially the care you have had for me as a person, and also everyone in our group. I will never have a better boss and I'm a little mad at you for that.

Now, we'll be discussing this in future sessions but I owe a lot to my therapist, we have worked together since 2020 and I know I was always capable of everything I've done so far, and I am capable of everything I want to do, but she is the one who helped me believe that so yes I could have done it without her help, but I would not have wanted to.

To the wonderful person I met on day one, Marten – the person I laughed with (and at) from the very start – I hope you know how important you are to me and how incredibly proud I am of you. Growing up with you over these years has been a pleasure (on average), and I am so happy to have you in my life. Thank you for all of the support, I love you.

My dearest Olga, you are the most supportive and caring friend anyone could have and we have the most fulfilling friendship I could ask for. Thank you for always having my back, I hope you know I'm there for you always.

This thesis and the knowledge I have gained from doing it can also be attributed to my two PhD older siblings. Caro and Jonas, thank you for teaching me all of the basics, being patient with me, and most of all becoming some of my favourite people. You are wonderful and I hope you know that you inspire me to no end. Selina and Tim, you are so used to me asking stupid questions, bugging you, or telling you the same stupid stories about the same stupid situations but I love you both so much. You called me out, comforted me, got real with me, laughed with me

and continue to support me, I cannot thank you enough.

To my parents — thank you for never telling me I couldn't do something. You instilled in me the utmost confidence, and I truly wouldn't be here without you (literally). For anyone who didn't understand the meaning of the opening paragraph of this thesis, it's a dedication to my parents. My mom has always said that I'm "Ellie" from the book/movie, Contact, and that one day I'll find the little green men, so this always reminds me of her. My dad and I absolutely love the small world ride at Disney world and it's something that always reminds me of him.

I have to try not to write pages and pages about how proud I am of my siblings and how they are the nicest, stupidest, silliest, most annoying but infinitely cool people I know. So I'll leave it like that. Maddie, Missy, Kenz and Rocco, just know I think you are amazing and I cannot believe I get to say I'm related to you (just note I will not reply to you ever again unless you address me with my new title).

This has easily been the easiest section of my whole thesis to write, I'm having the opposite problem to the rest of the sections, I can't stop writing. Kaya, thank you for being a great flatmate, we have had many experiences together and I'm so happy to have met you. Sebastian, I wouldn't have gotten through without our shared love for Taylor, you are such a hard worker, and lovely person, I'm excited to see the great things you do. Evert, the support and care you have shown me has been heart-warming, you are one of my favourite people and I feel so lucky to call you my friend. Thank you for always being on my team. Verena, thank you for giving me a chance even after seeing how grumpy my resting face can be. You always listened, always stood by my side, and I can't thank you enough for that. Paul and Laura, you are two of the kindest people, and I'm so grateful for the friendship we've built. Eric — sunshine — thank you for bringing so much happiness to everyone around you, and for always managing to put a smile on my face, even on my grumpiest days. Wishing you all the best for everything ahead. Fabi, what started as Trash TV Tuesdays and Christmas cookies turned into brunches, coffees, and countless catch-ups. You've always been such a supportive friend, and I'm so proud of you and excited to see what's next. Callie, from the start you showed such kindness and support. Some of my favourite memories are with you, I can't thank you enough — I'm so proud of you and everything you've done. Postdoc Steve, we really need to do more baking because we absolutely kill it in the kitchen — especially if cinnamon is involved (which, with us, it usually is). Thanks for always checking in on me — it means more than you know. Dan and Evie, you two are not just adorable but also two of the kindest souls. You've shown me how much you care time and time again. I'm looking forward to many more walks, dinners, and cake/coffee dates together. A huge thank you to my PhD younger brother Simon, for putting up with me. Somewhere along the way we became besties, and I can't wait to read your thesis when you graduate. There are so many more people I want to thank — Rhys, Svenja, Malin and Passy — you are all wonderful, and I'm so grateful to have crossed paths with you. A really special part of my time at MPIA has been the Womens+ community. I've loved our meetings and the sense of support they brought. I feel so lucky to have found a space where I can be open and share my life. Finally, a huge thank you to my examiners, Henrik and Laura, the rest of my committee, and to everyone who gave feedback, shared advice, or simply listened to me vent — I'm deeply grateful.

I hope that anyone reading this can tell how much I love these people and how incredible they are. I am the luckiest person.